JOURNAL OF THE AERONAUTICAL SCIENCES

VOLUME 13 DECEMBER, 1946 NUMBER 12

The Interaction Between Boundary Layer and Shock Waves in Transonic Flow*

HANS WOLFGANG LIEPMANN†

California Institute of Technology

SUMMARY

Experiments of transonic flow past a circular arc profile show that the shock-wave pattern and the pressure distribution are strongly dependent upon the state of the boundary layer. A change from laminar to turbulent boundary layer at a given Mach Number changes the flow pattern considerably.

Shock waves can interact with the boundary layer in a manner similar to a reflection from a free jet boundary. These shock waves are not distinctly discernible from pressure distribution measurements.

INTRODUCTION

MOST EXPERIMENTAL INVESTIGATIONS of transonic flow phenomena have been based on the assumption that the Mach Number is the only important parameter. Reynolds Number effects were assumed, in general, to be negligible. There are, however, certain reasons to suspect that Reynolds Number effects can be appreciable and that the boundary layer does influence the transonic flow pattern. One of these reasons is that potential theory has shown that smooth transonic (that is, subsonic-supersonic-subsonic) flow is possible with local Mach Numbers well in excess of unity (for example, reference 1). Experiments[2] to date have failed to show the existence of large local supersonic regions without the occurrence of shock waves. This discrepancy between theory and experiment can be due to the fact that the potential solution for shock-free transonic flow is a possible but unstable solution, while the flow with shock wave is more stable and occurs in experiment; or the discrepancy may be due to the fact that certain basic assumptions of the theory (i.e., steady, nonviscous flow of a perfect gas) are not met in the experiments. Of these assumptions, the one that is most likely to fail is that of zero viscosity. In nearly all cases, transonic flow occurs near a solid boundary. Thus, the supersonic zone will be in contact with a laminar or turbulent boundary layer, the existence of which is neglected in potential theory.

These two possibilities may be illustrated with well-known examples from real fluids. In pipe flow laminar motion is a possible solution for all Reynolds Numbers. Actually, beyond a certain Reynolds Number turbulent flow is always found experimentally. This is due to the fact that laminar flow is not a stable solution.

A different example is flow in a divergent channel or diffuser. It is well known that the flow pattern for a nonviscous fluid and for a viscous fluid are radically different, even for vanishingly small viscosity. The actual flow pattern of the real fluid cannot be approximated by perfect fluid flow.

In fact, it is fortunate that in most subsonic aerodynamic problems full use can be made of the classical boundary layer theory, and that pressure forces can be computed on the basis of the perfect fluid flow, i.e., potential theory. The influence of viscosity and turbulent shear is generally restricted to a narrow zone, the boundary layer, and is important for friction effects only. It will be seen that in some problems of transonic flow, and probably for some supersonic flow problems, the classical boundary layer assumptions fail so that results derived from boundary layer theory become questionable.

The investigations reported here have as their ultimate goal the understanding of the formation of shock waves in transonic flow. The reasoning outlined above led to the belief that boundary layer effects are of paramount importance in transonic flow phenomena. Hence, the interaction between boundary layer and shock wave was the object of the first investigations.

Received June 29, 1946.

* The author wishes to acknowledge the cooperation of Mrs. K. Liepmann and of Messrs. H. Ashkenas and J. D. Cole.

† Associate Professor of Aeronautics.

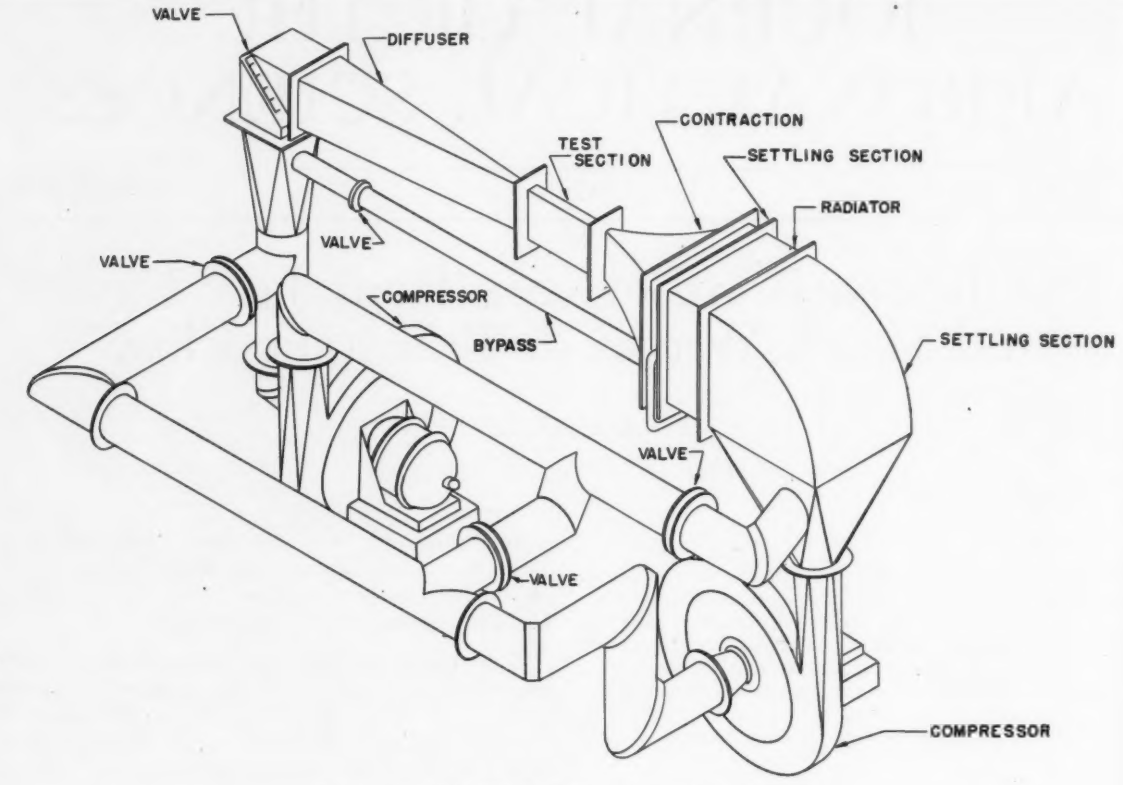

FIG. 1. The GALCIT 2- by 20-in. transonic wind tunnel.

The work presented here was carried out during 1945* at the California Institute of Technology under the sponsorship of the Air Technical Service Command, Wright Field.

APPARATUS AND METHODS

Wind Tunnel

The 2- by 20-in. transonic wind tunnel, built specifically for investigations of this type, was used in these experiments. A general layout of the tunnel is shown in Fig. 1. The tunnel is driven by two turboblowers that can be operated either in series or in parallel. The power is sufficient to choke the tunnel with any model.

The emphasis in the design of the tunnel was on flexibility and quality of the airflow, i.e., low turbulence and steady and easily adjustable flow. Considerations of energy ratio were of secondary importance. Hence, screens are used freely in the circuit to reduce the turbulence level. The speed is regulated by throttling and by-passing, the blowers being driven by constant speed induction motors. An extremely fine speed control between $M_T \doteq 1$ and $M_T \doteq 0.1$ is obtained in this manner. Details of the tunnel construction can be found in reference 3.

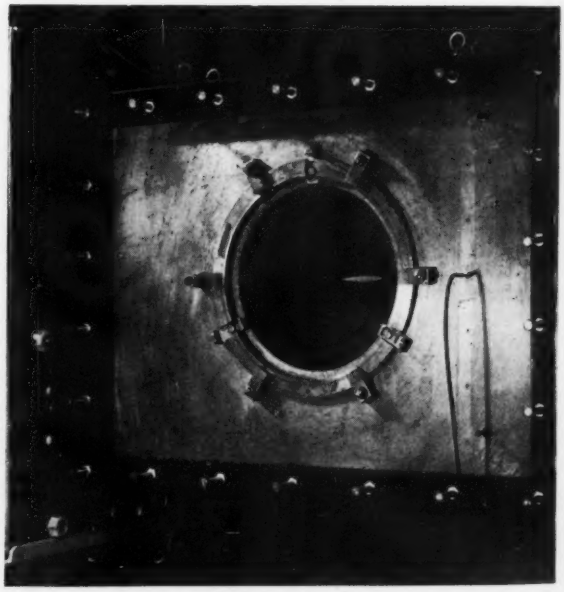

FIG. 2. The test section of the GALCIT 2-by 20-in. transonic wind tunnel with the 3-in. by 12 per cent biconvex airfoil in place.

* The research was actually initiated in 1944. The first year was spent in the design and construction of the wind tunnel and equipment.

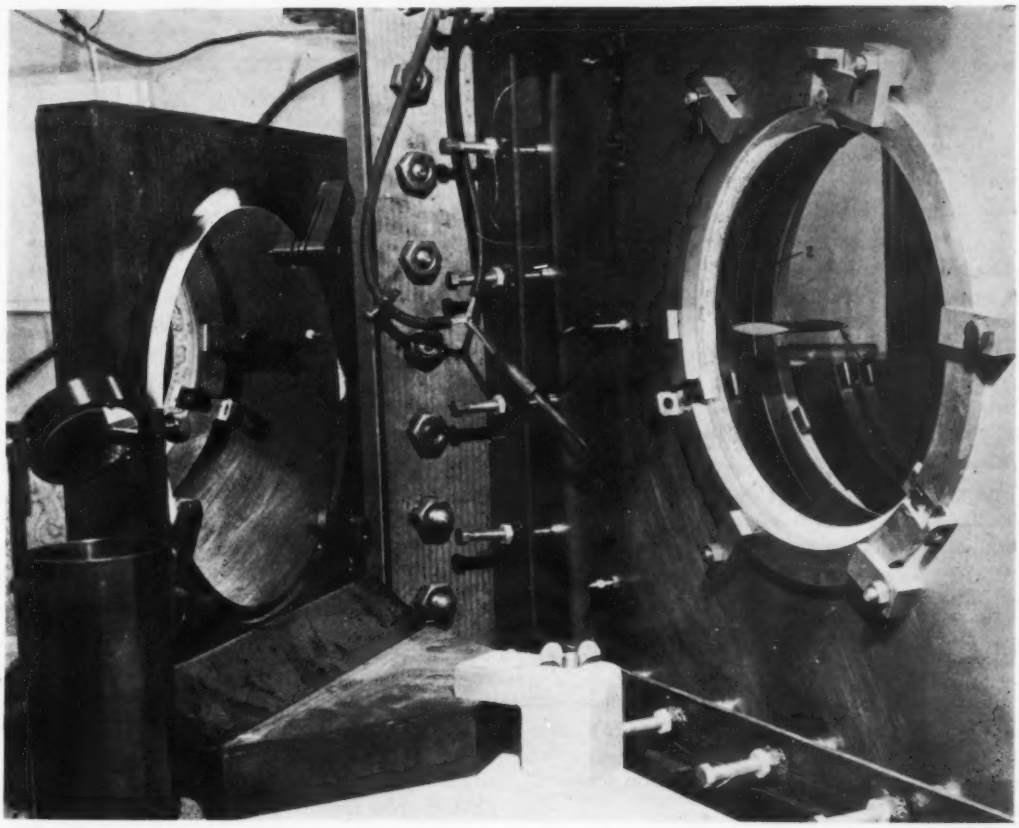

FIG. 3. Test section wall showing pin vises (1) and phosphor bronze wires (2) used in mounting the model (3).

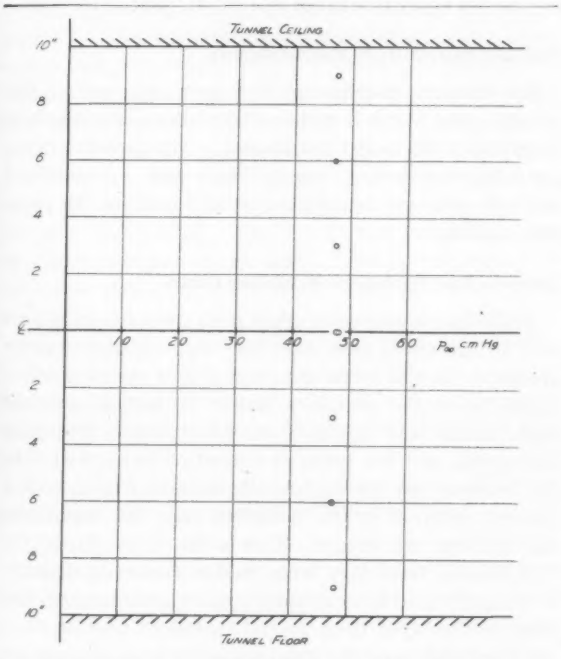

FIG. 4. Vertical pressure distribution on tunnel wall empty tunnel.

Test Section and Model

The test section is seen in Fig. 2. The dimensions are 2 by 20 by 36 in. The section widens from 2.00 in. at the entrance to 2.21 in. at the exit to keep the Mach Number distribution uniform. The maximum variation in Mach Number along the section at $M = 0.85$ was found to be 2.5 per cent.

The model support is seen in Fig. 3. The airfoil is held between the glass walls by friction. Two fine wires stretch upstream along the walls of the test section. These wires are for safety only and do not carry much load. The wires are in the wall boundary layer and do not, therefore, disturb the flow past the model. This type of model support was found to be suitable for the present experiments. The drilling of holes in the glass walls is avoided, and the position of the model in the test section can be changed easily.

Humidity Control

For the investigations presented here it was found that raising the stagnation temperature in the tunnel gave adequate humidity control. The cooling water for the radiator can be regulated easily and the temperature in the tunnel adjusted to within 0.2°. The

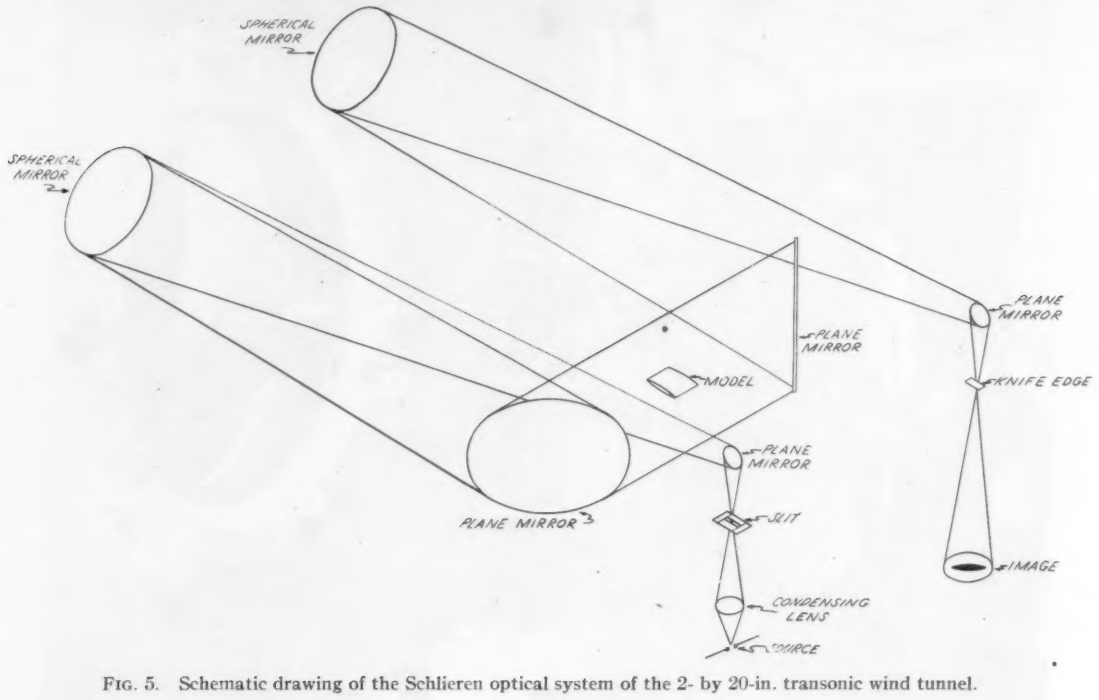

FIG. 5. Schematic drawing of the Schlieren optical system of the 2- by 20-in. transonic wind tunnel.

measurements were all made at a stagnation temperature.

$$\vartheta_0 = 55.5°\text{C.} \pm 0.2°$$

The dew-point temperature was always found to be

$$\vartheta_s = 14°\text{C.} \pm 2°$$

The stagnation temperature was measured by means of a resistance thermometer in the settling chamber. The saturation temperature was measured by means of a dew-point meter of the type described in reference 4.

Determination of Mach Number

The Mach Number M_T in the test section was obtained from readings of the difference between the pressure in the settling chamber p_0 and the average pressure p_T in the test section upstream of the model ($p_0 - p_T$) and of the absolute value of p_T. M_T is then given by the well-known relation

$$p_0/p_T = \{1 + [\gamma - 1)/2]M_T^2\}^{\gamma/(\gamma-1)}$$

$\gamma = C_P/C_V$ was always taken as 1.400.

The pressure distribution normal to the direction of flow in the reference plane is shown in Fig. 4.

Schlieren System

The Schlieren system employed in these investigations is of the two-mirror type. The actual light path is complicated because of lack of space. The light path is shown in Fig. 5. The quality of the pictures is not adversely affected by the rather complicated setup. The photographs are sharp enough to allow enlargement to more than six times the original size of 4 by 5 in.

For continuous observation, a mercury vapor lamp (G-E H4) was used. The photographs were made by means of a spark discharge of 4×10^{-6} sec. duration.

Pressure Distribution Measurements

For pressure distribution measurements, one of the circular glass plates is replaced by a stainless-steel plate upon which the model is mounted. The pressure tubes are taken out through the steel side wall. A standard multiple mercury manometer is employed for the pressure readings.

Laminar and Turbulent Boundary Layer

Schlieren photographs taken with the knife edge parallel to the mean flow direction—i.e., so that density gradients normal to the direction of flow are recorded—clearly show the boundary layer. In fact, it is found that laminar and turbulent boundary layers are easily discernible and the point of transition is marked. In the laminar case the edge of the boundary layer is well defined, whereas in the turbulent case the edge fades out into the free stream. This is due to two facts: (1) The laminar boundary layer profiles (velocity, density, or temperature) have a much larger curvature near the edge of the layer than do the turbulent profiles; (2) the boundary layer fluctuations in the laminar case are of a much larger scale than those in turbulent layers.

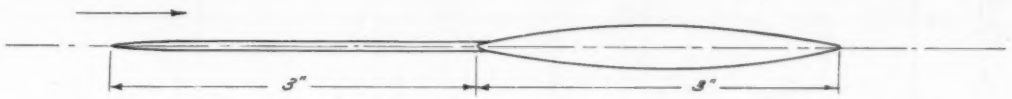

FIG. 6. Three-in. by 12 per cent circular arc airfoil + 3- by $^1/_{16}$-in. flat plate.

Hence, the optical "surface" formed by the boundary layer is "wavy" in the laminar and "rough" in the turbulent case.

The transition point of the airfoil used in the present investigation was, except for the very highest Mach Numbers, downstream of the shock wave. Transition was found to occur at about 80 per cent chord at a Mach Number $M_T = 0.795$ and at a Reynolds Number, based on the airfoil chord, of $R = 850{,}000$.

To investigate cases in which the boundary layer is turbulent at the position of the shock wave, the following simple procedure was used: A thin ($^1/_{16}$ in.), pointed flat plate was fastened to the leading edge of the airfoil as shown in Fig. 6. This plate, at zero angle of attack, does not appreciably affect the pressure distribution. It does, however, produce an effectively larger Reynolds Number and a turbulent boundary layer. Using this scheme, measurements at the same Mach Number with both laminar and turbulent boundary layer could be made and compared. Other obvious means to render the boundary turbulent, such as surface roughness elements and increased tunnel turbulence, were also used occasionally.

PURPOSE OF THE EXPERIMENTS

The experiments were undertaken to study the mechanism of the boundary-layer-shock-wave interaction rather than to test specific airfoil shapes. The choice of model, therefore, was dictated only by considerations of simplicity. A 12 per cent thick, double circular arc section of 3-in. chord was chosen, and all experiments reported here were carried out with this model at zero angle of attack. The critical Mach Number for this airfoil is $M_c = 0.79$. The tunnel was found to choke at Mach Number $M_T = 0.91$. The investigations of transonic flow thus covered the range between these limits.

Wind-tunnel wall corrections are of minor importance in the present investigation, since no attempt to simulate free flight conditions is made. The Mach Numbers given in the figures are thus the uncorrected Mach Numbers.

Two types of measurements were made, Schlieren photographs and pressure distribution surveys. It will be seen that, in spite of many prejudices, Schlieren photographs can give a clear picture of the flow pattern and, furthermore, when properly evaluated, can furnish a great deal of quantitative information. Schlieren photographs have the great advantage of being the result of a nearly instantaneous observation. This is important for boundary layer effects, which by nature are quasi-stationary and fluctuating.

Pressure distribution measurements, especially with models of small scale, have a large time lag and furnish a picture of mean effects only. The difference in time lag must be taken into account in comparing Schlieren photographs with pressure distribution measurements.

Errors in the pressure distribution measurements can arise from faulty orifices, lack of two-dimensional flow, etc. The results presented were checked for freedom from systematic errors by a simple procedure. The orifices were purposely distributed asymmetrically with respect to both centerlines of the airfoil. Rotating the airfoil through an angle of 180° moves each orifice into a new position. If the pressure distribution in both positions checks within the experimental scatter, the systematic errors are negligible. This was found to be the case for the measurements presented here.

RESULTS

"Laminar" and "Turbulent" Shock Waves

Figs. 7 to 12 show a series of pressure distribution and Schlieren photographs for the airfoil with both laminar and turbulent boundary layer. It is evident *that marked difference in the shock-wave pattern and pressure distribution exists between the laminar and the turbulent cases.**

The main observations are these: The "laminar" shock waves are inclined upstream. No sudden increase in the surface pressures is observed. The "turbulent" shock waves, on the other hand, are nearly normal or inclined downstream. The pressure distributions show the familiar sudden pressure increase. In the laminar case two or more shock waves appear; in the turbulent case only one shock wave is present, in general.

Shock "Reflections" from the Boundary Layer

Close examination of a Schlieren photograph of the shock wave for the case of laminar boundary layer shows the following (Fig. 13): The shock wave is followed by a fan-shaped expansion zone. The boundary layer thickens ahead of the shock wave. At the point of contact with the shock wave and expansion zone, the edge

* Similar results have been found independently by Dr. J. Ackeret, at Zurich, Switzerland. Ackeret's results apparently have not yet been published. Dr. H. S. Tsien who visited the Eidgenossische Technische Hochschule in 1945 informed the author of Dr. Ackeret's investigations.

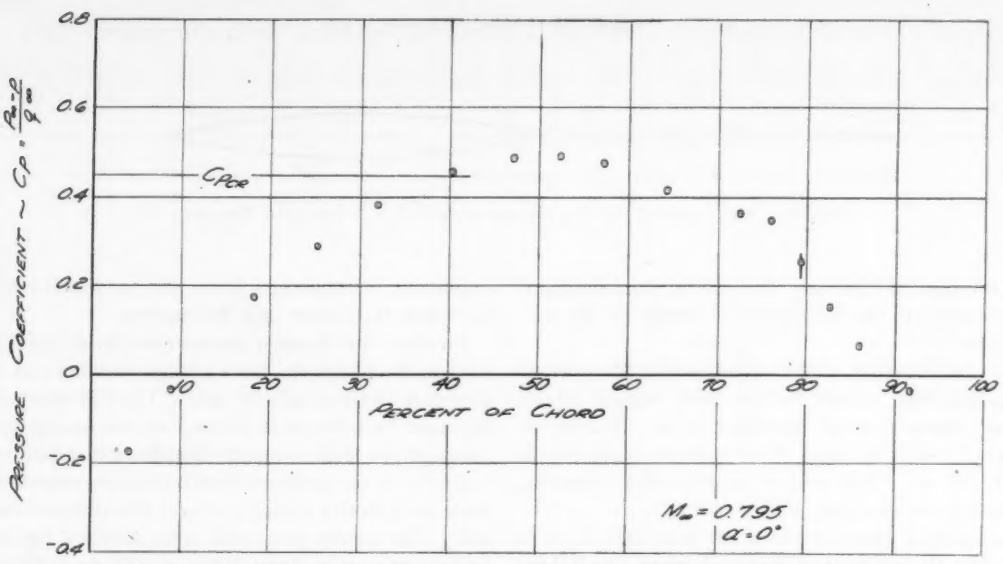

FIG. 7a. Pressure distribution 3-in. by 12 per cent circular arc airfoil, $R = 8.33 \times 10^5$ (laminar).

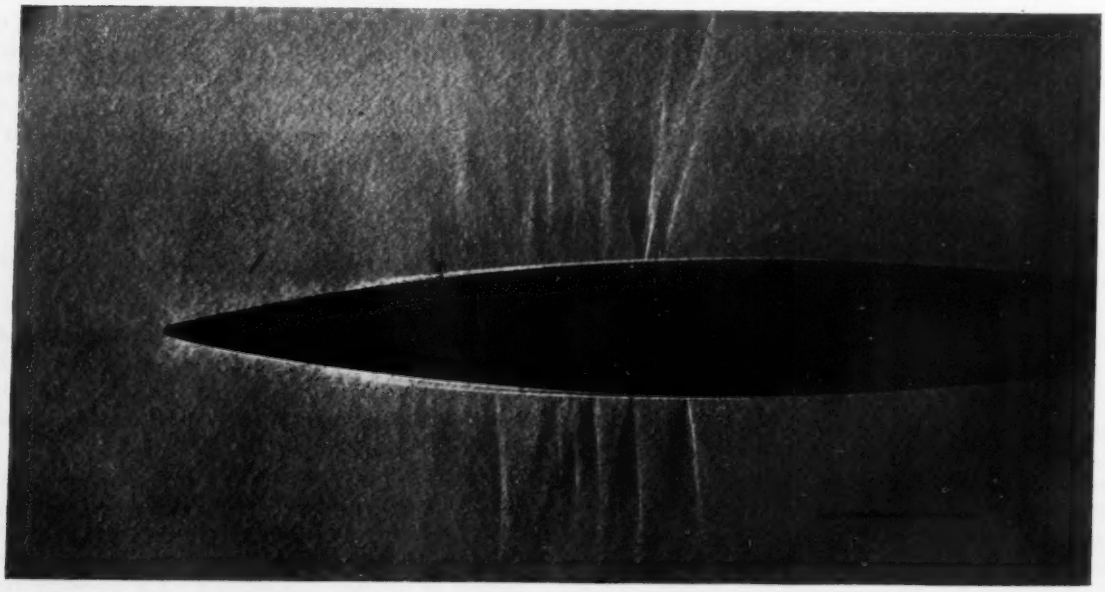

FIG. 7b. Flow at $M_\infty = 0.795$, $R = 8.33 \times 10^5$ (laminar); knife edge normal to mean flow directon.

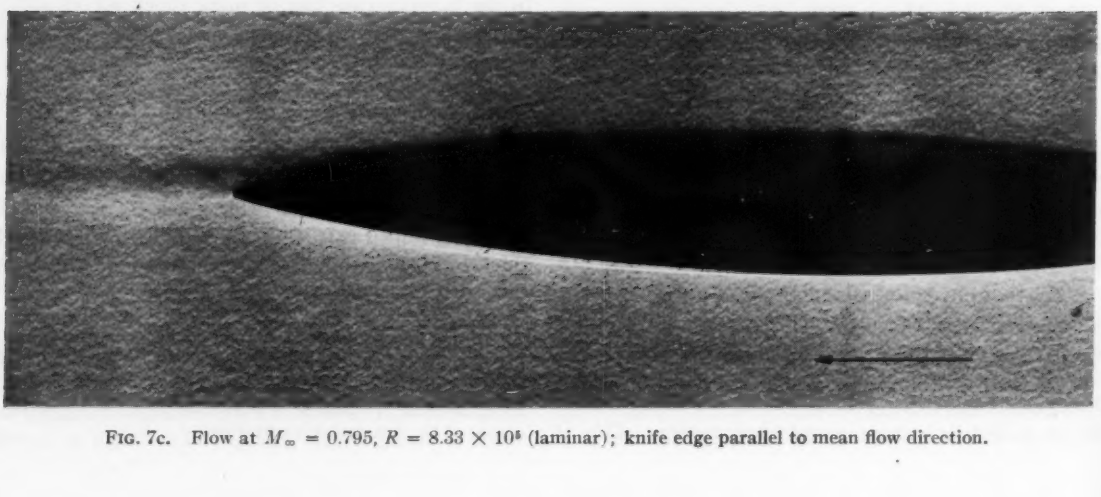

FIG. 7c. Flow at $M_\infty = 0.795$, $R = 8.33 \times 10^5$ (laminar); knife edge parallel to mean flow direction.

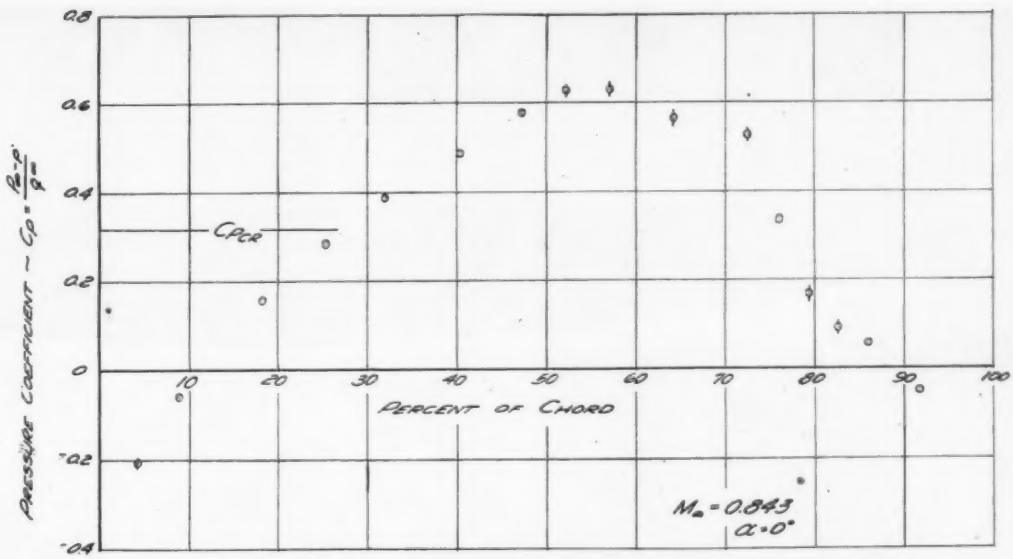

FIG. 8a. Pressure distribution 3-in. by 12 per cent circular arc airfoil, $R = 8.45 \times 10^6$ (laminar).

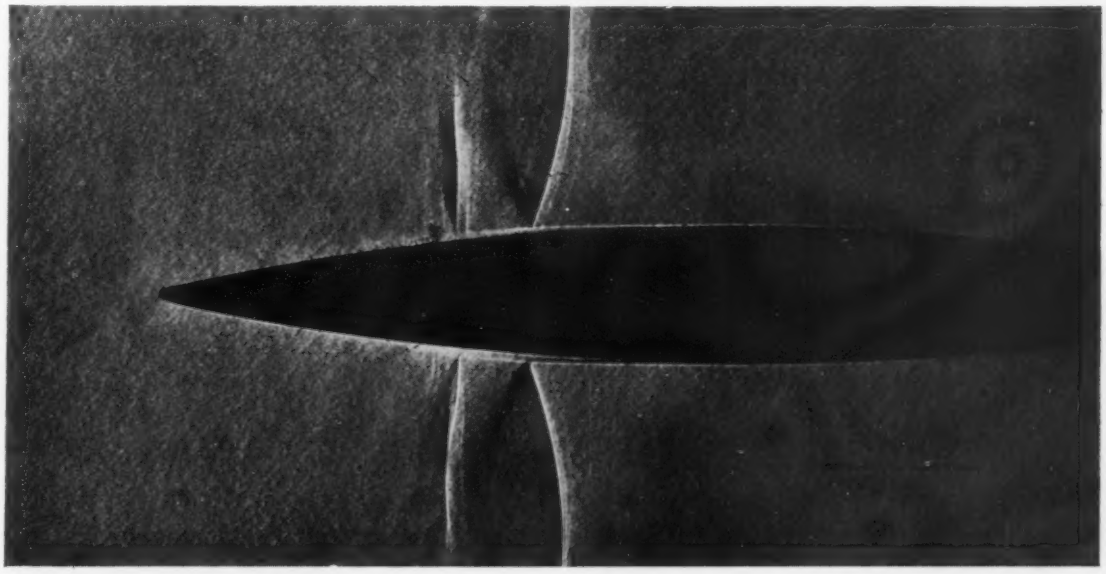

FIG. 8b. Flow at $M_\infty = 0.843$, $R = 8.45 \times 10^6$ (laminar); knife edge normal to mean flow direction.

of the boundary layer is seen to make a definite bend *toward* the wall.

The flow field existing near the base of the shock wave is shown schematically in Figs. 14 and 15. The flow passes the shock wave first and the pressure increases from P_1 to P_2. The Mach Number decreases from M_1 to M_2. Since the shock wave is oblique, the direction of flow changes by an amount $\Delta_1\vartheta = \vartheta_1 - \vartheta_2$. These changes are discontinuous—i.e., extremely rapid.

In the subsequent expansion zone the flow is again accelerated, but in a continuous fashion, corresponding to the well-known Prandtl-Meyer flow. The pressure decreases from P_2 to P_3; the Mach Number increases from M_2 to M_3. The flow is turned farther in the same direction by an amount $\Delta_2\vartheta = \vartheta_2 - \vartheta_3$.

Quantitative results can easily be obtained from the Schlieren photographs using the results of the well-known theory of oblique shock waves and of Prandtl-Meyer flow (i.e., isentropic flow around a corner). The procedure is as follows:

(1) M_3 is obtained from the angle θ_3 between the direction of flow (indicated by the visible edge of the boundary layer) and the downstream edge of the expansion zone. θ_3 is the Mach angle and, hence,

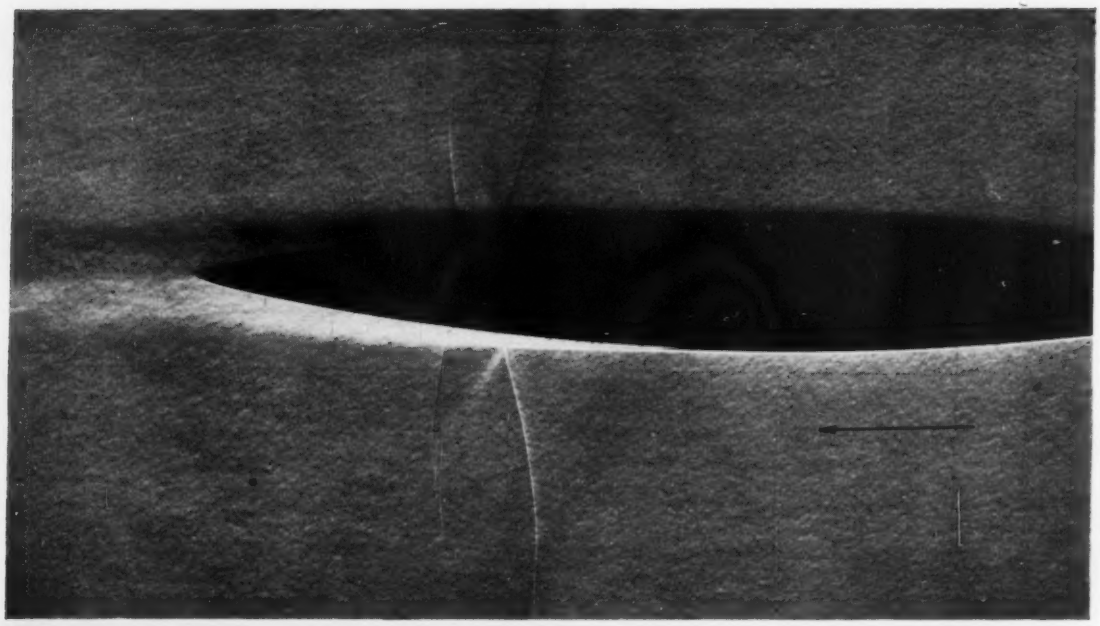

FIG. 8c. Flow at $M_\infty = 0.843$, $R = 8.45 \times 10^6$ (laminar); knife edge parallel to mean flow direction.

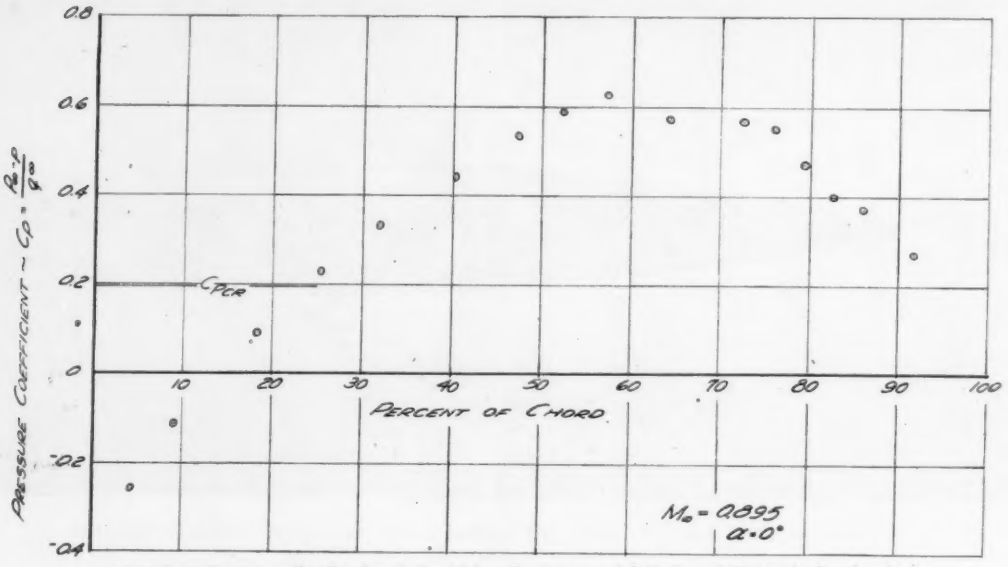

FIG. 9a. Pressure distribution 3- by 10-in. circular arc airfoil, $R = 8.77 \times 10^5$ (laminar).

TABLE 1
$M_\infty = 0.843$

M_1	M_2	M_3	p_1/p_0	p_2/p_0	p_3/p_0	p_0'/p_0	$\vartheta_{1_\infty} - \vartheta_2$	$\vartheta_2 - \vartheta_3$
1.18	1.01	1.09	0.427	0.516	0.468	0.984	2.7°	1.0°

$$M_3 = \csc \theta_3$$

(2) M_2 is obtained from the angle of spread, ω, of the expansion zone and M_3, by using the Prandtl-Meyer theory. (See, for example, reference 5.)

(3) The wave angle, θ_1, of the shock wave and the Mach Number, M_2, behind the wave determine M_1, the Mach Number on the upstream side of the shock wave.

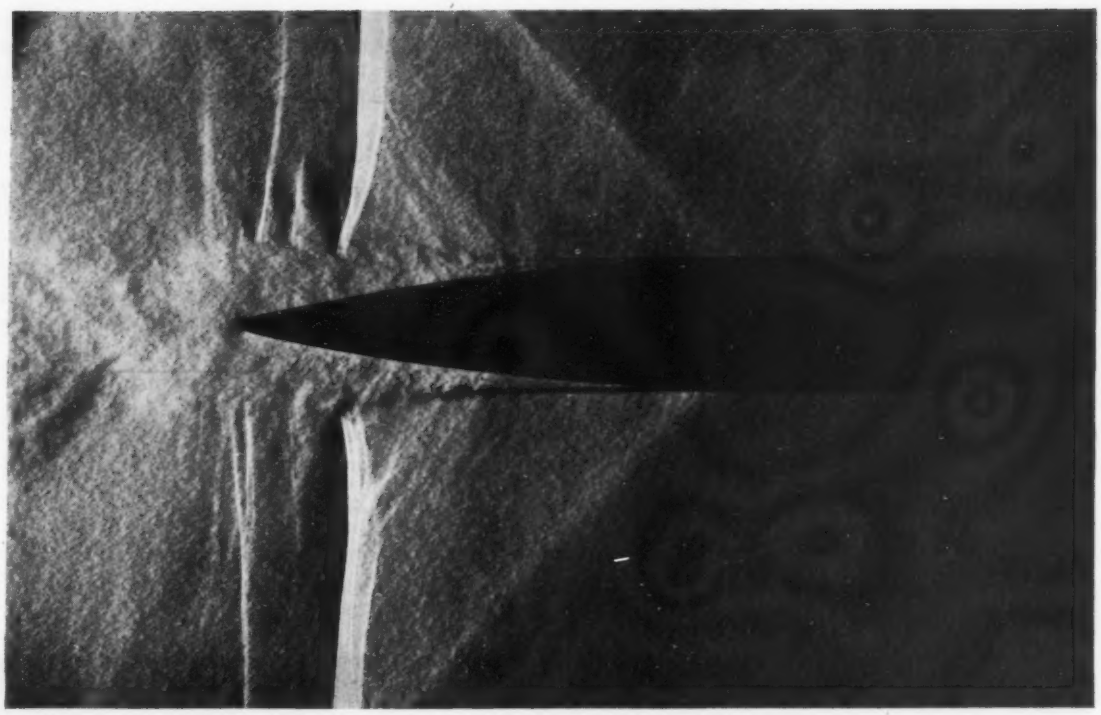

FIG. 9b. Flow at $M_\infty = 0.895$, $R = 8.77 \times 10^5$ (laminar); knife edge normal to mean flow direction.

FIG. 9c. Flow at $M_\infty = 0.895$, $R = 8.77 \times 10^5$ (laminar); knife edge parallel to mean flow direction.

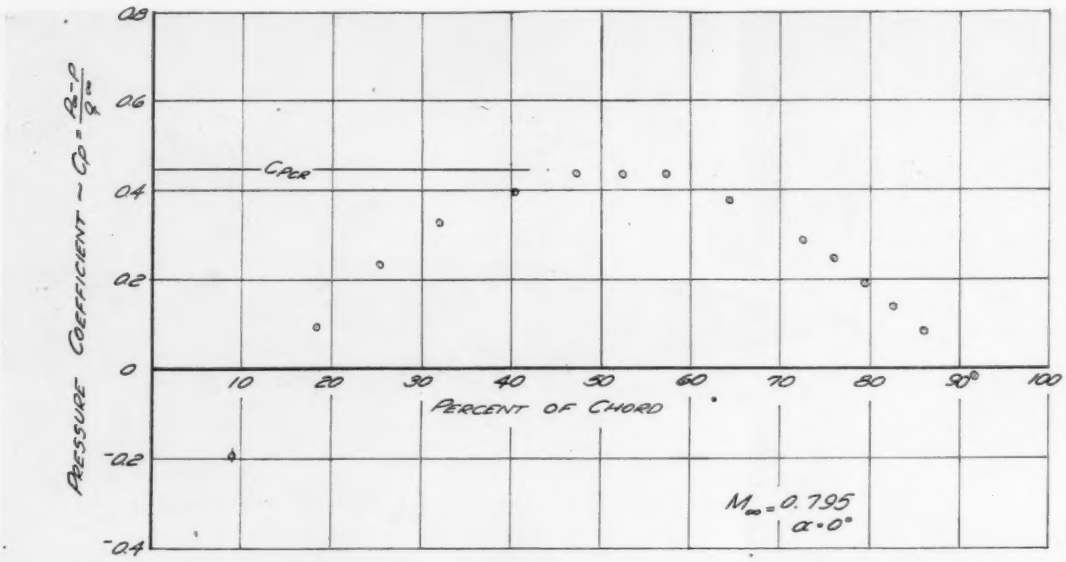

FIG. 10a. Pressure distribution 3-in. by 12 per cent circular arc airfoil + 1/16- by 3-in. flat plate, $R = 1.67 \times 10^6$ (turbulent).

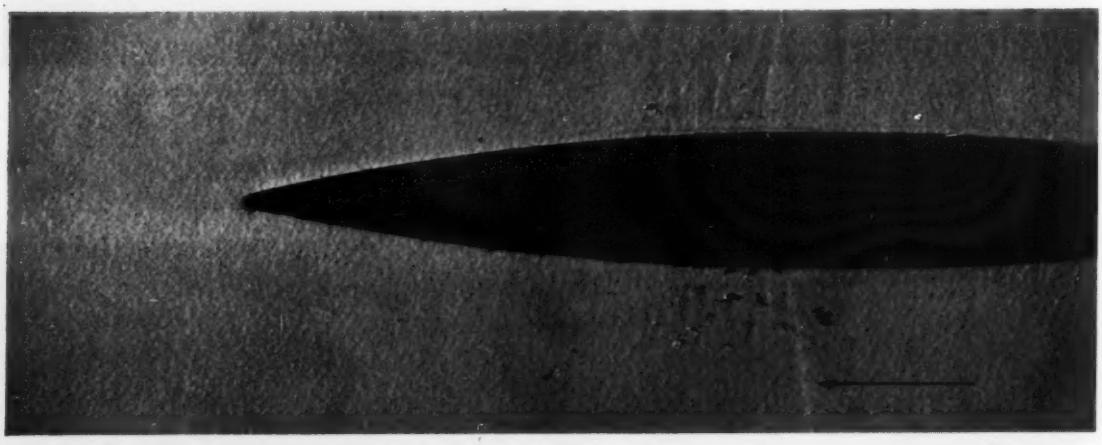

FIG. 10b. Flow at $M_\infty = 0.795$, $R = 1.67 \times 10^6$ (turbulent); knife edge normal to mean flow direction.

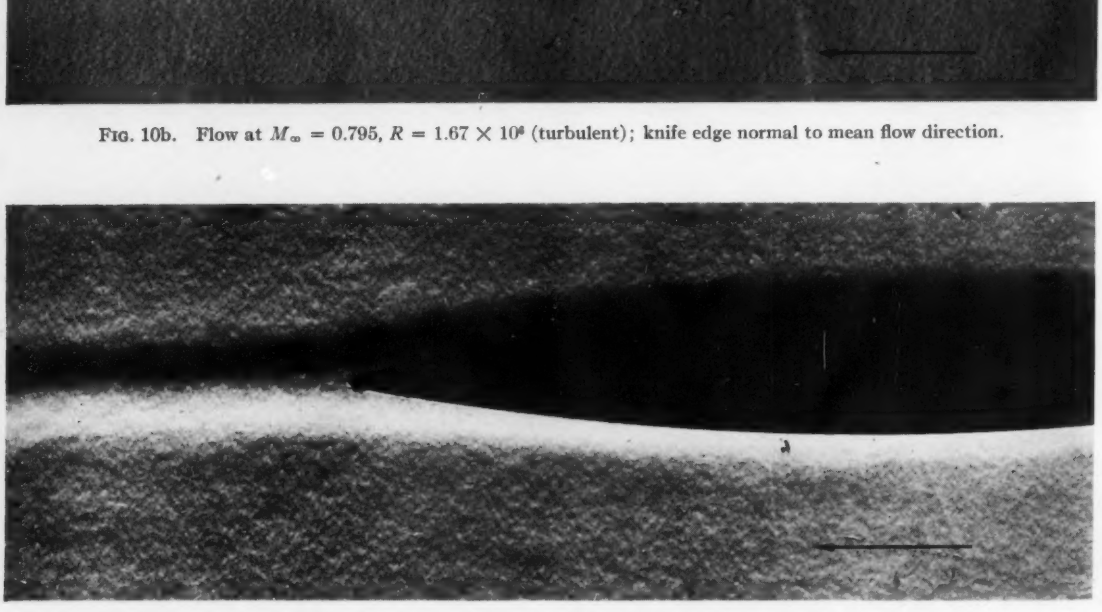

FIG. 10c. Flow at $M_\infty = 0.795$, $R = 1.69 \times 10^6$ (turbulent); knife edge parallel to mean flow direction.

(4) From the stagnation pressure p_0 ahead of the shock and the Mach Number, the stagnation pressure behind the shock p_0' may be computed.

Table 1 presents the results of a typical evaluation of this kind.

It should be remembered that ordinary Prandtl-Meyer flow past a convex surface is an exact solution only for a supersonic zone of infinite extent. However, it can be expected to give a good approximation to a turning supersonic flow only when the radius of curvature is small compared with the extent of the supersonic zone. In this case, then, it can be applied.

It is evident that:

(1) The flow behind the shock wave—expansion zone combination is supersonic. Hence another similar process can occur. The process will be repeated until subsonic speeds are finally obtained. Recompression occurs in two ways. The pressure upstream of the shock wave is seen to increase slightly. The Schlieren photograph shows a faint triangular compression zone. The entropy increases in the passage through the shock wave, and thus the Mach Number corresponding to the same local pressure is less behind the shock. The entropy increases in the passage through the shock wave, and thus the Mach Number corresponding to the same local pressure is less behind the shock.

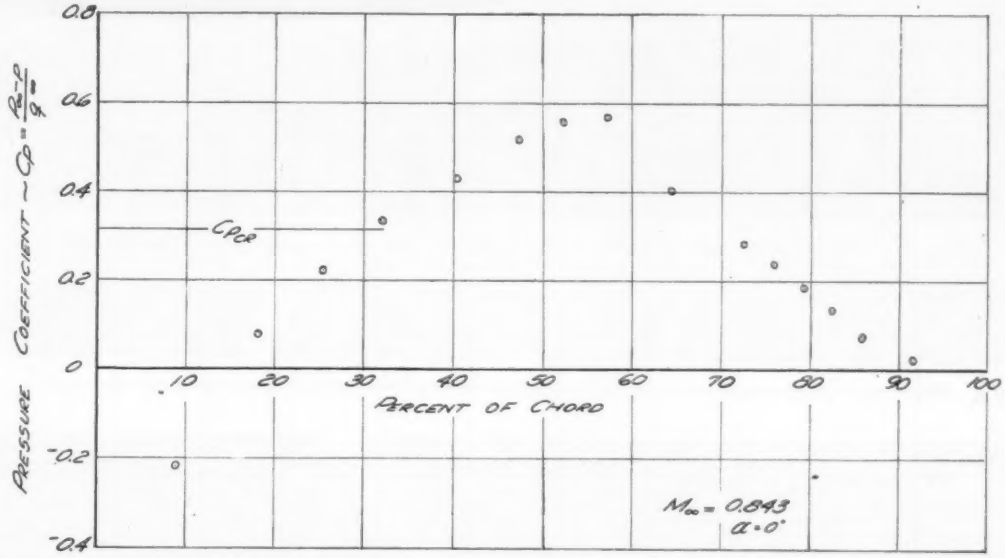

FIG. 11a. Pressure distribution 3-in. by 12 per cent circular arc airfoil + 1/16- by 3-in. flat plate, $R = 1.69 \times 10^6$ (turbulent).

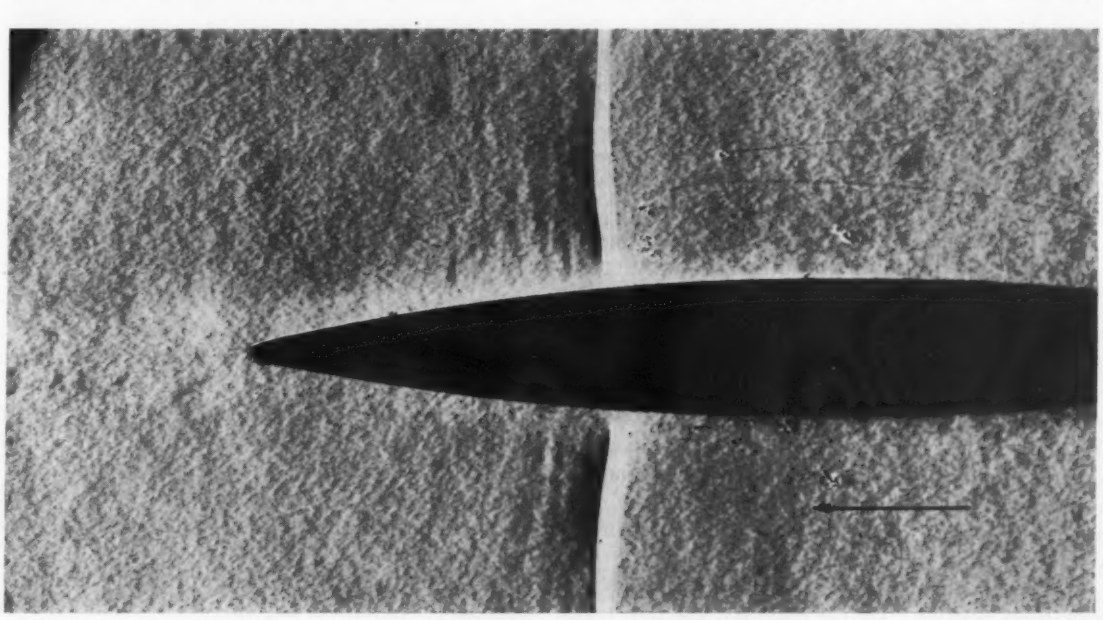

FIG. 11b. Flow at $M_\infty = 0.843$, $R = 1.69 \times 10^6$ (turbulent); knife edge normal to mean flow direction.

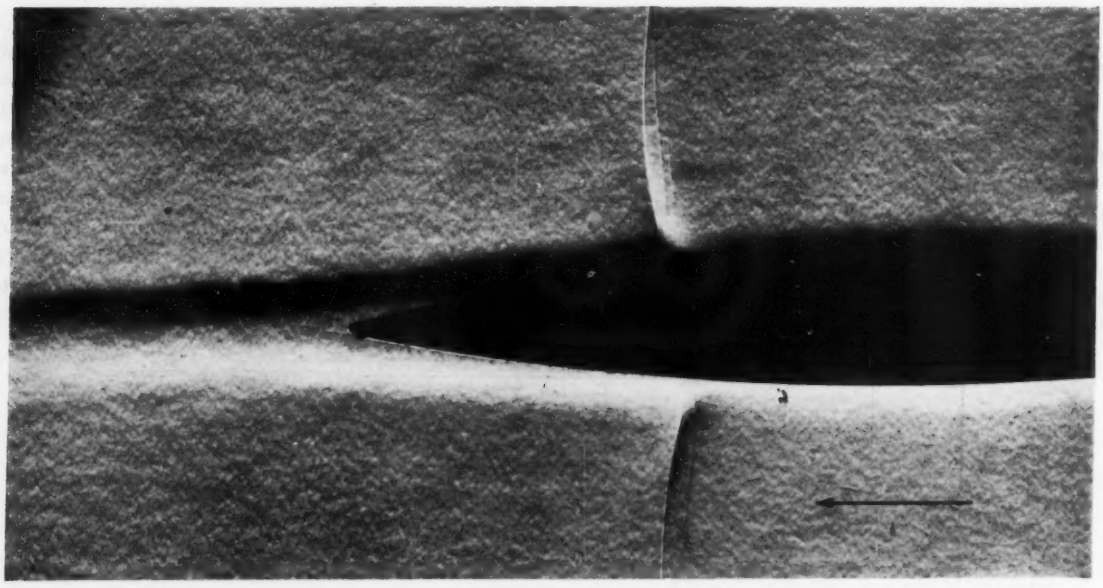

FIG. 11c. Flow at $M_\infty = 0.843$, $R = 1.69 \times 10^6$ (turbulent); knife edge parallel to mean flow direction.

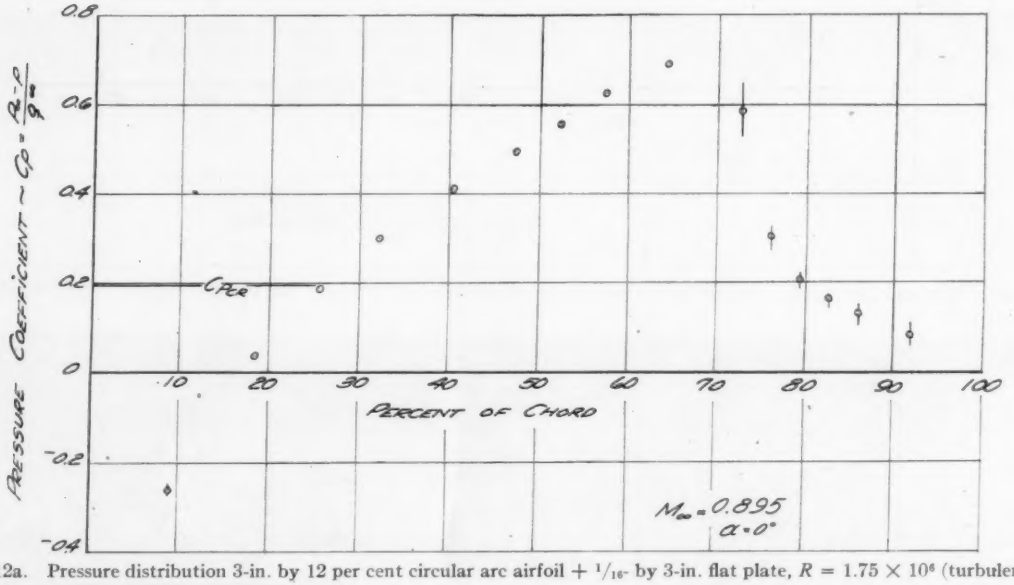

FIG. 12a. Pressure distribution 3-in. by 12 per cent circular arc airfoil + $^1/_{16}$- by 3-in. flat plate, $R = 1.75 \times 10^6$ (turbulent).

(2) The pressures just upstream and just downstream of the shock-expansion combination do not differ greatly. *Hence, this type of shock wave is not easily discernible from surface pressure distribution measurements.* This fact, which was first found by an analysis of Schlieren photographs, was completely borne out by the pressure distribution measurements made at a later date (see Fig. 8). The behavior of the pressure is sketched in Fig. 15.

(3) The boundary layer does not separate at the shock-wave position. On the contrary, the flow turns toward the surface.

The behavior of the shock wave near the surface can be summarized in the statement that the shock wave interacts with the boundary layer in a manner similar to shock interaction with a free jet surface. In other words the boundary condition satisfied here is more nearly the condition of *constant pressure* than that of *constant direction*. This fact is believed to be of fundamental importance for the understanding of many transonic phenomena.

This result is by no means surprising. The rigorous boundary condition in any case is the condition of zero slip at the solid wall. This condition can be satisfied

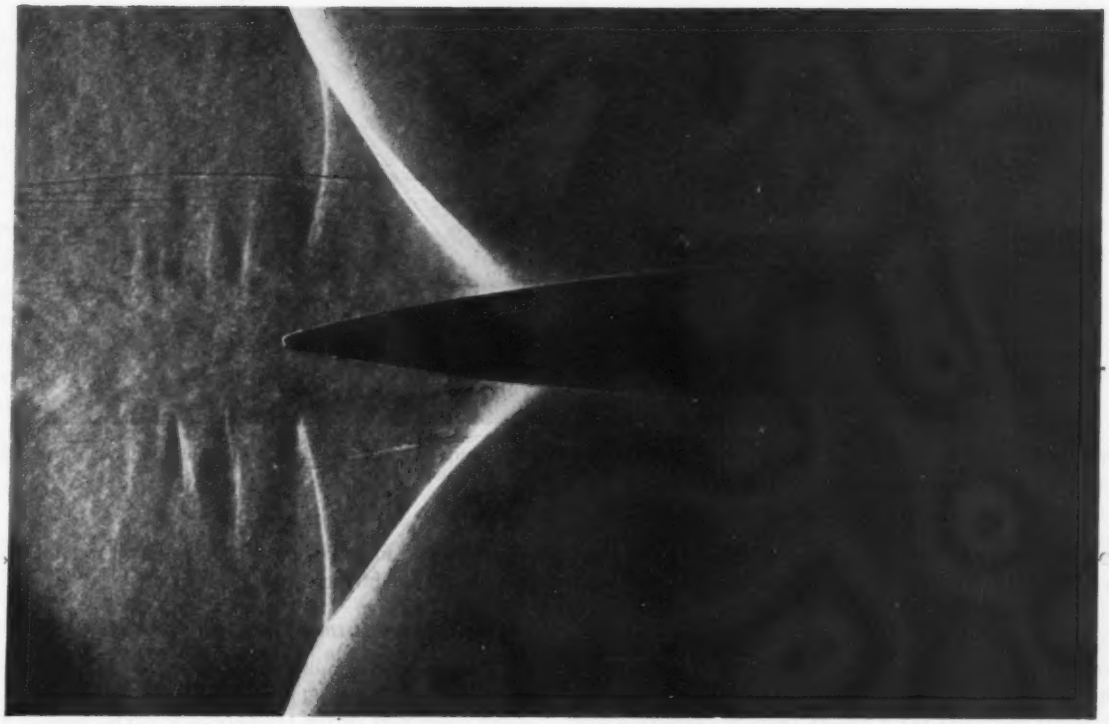

FIG. 12b. Flow at $M_\infty = 0.895$, $R = 1.75 \times 10^6$ (turbulent); knife edge normal to mean flow direction.

FIG. 12c. Flow at $M_\infty = 0.895$, $R = 1.75 \times 10^6$ (turbulent); knife edge parallel to mean flow direction.

only by a viscous fluid. The classical boundary layer theory leads to the result that the flow about a body can be separated into a boundary layer where viscous effects are appreciable and potential flow outside of this layer. The boundary condition of the viscous flow in the boundary layer is the condition of zero slip. The condition to be satisfied by the potential flow outside of the boundary layer is that of zero normal velocity near the wall—i.e., at a distance equal to the displacement thickness of the layer. Hence, according to the classical boundary layer theory, potential flow is similar *to flow past a solid body* of a shape nearly identical with the real body.

This result is based on the assumption that all changes of fluid properties in the direction of flow are small compared with the changes normal to the flow direction (i.e., the boundary layer thickness δ is assumed to be the smallest characteristic length). This condition

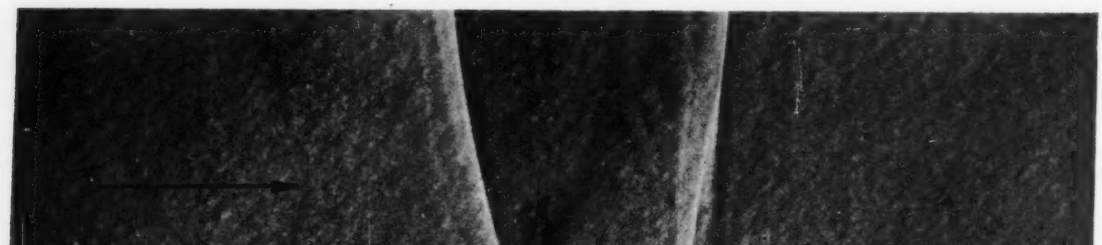

FIG. 13. Flow at $M_\infty = 0.843$, $R = 8.45 \times 10^5$, showing the flow expansion and the "corner" of the boundary layer; knife edge normal to mean flow direction.

can fail near the base of a shock wave. The changes of velocity in the x direction—i.e., in this case parallel to the mean flow—are often of the same order or larger than the changes in the y direction—i.e., across the boundary layer. A new length, τ, the thickness of the shock wave, is important. Since $\tau \ll \delta$, all results of the classical boundary layer theory become questionable in the neighborhood of a shock wave. This includes, of course, the boundary condition to be satisfied by the flow outside the viscous zone. If the changes in the direction of flow become large compared to the changes across the layer, the appropriate boundary condition for the outer flow *appears to approach the condition prevailing near a free surface rather than near a solid wall.*

Although the inclination of the "laminar" shock wave upstream may appear surprising at first, it can easily be explained. Essentially, it is due to the finite extent of the supersonic zone. In terms of Mach lines—i.e., expansion and compression wavelets—the existence of a finite supersonic region means that the effects of both families of Mach lines must be considered. In general, for flow past a convex surface, the expansion wavelets will be inclined downstream and the compression wavelets inclined upstream. Thus, if a shock wave is formed as an envelope of compression wavelets, it must be inclined upstream.

The Shock Wave in the "Turbulent" Case

Close examination of the shock-wave pattern for the turbulent case (Fig. 11) reveals a completely different result from that of the laminar case. The base of the shock wave is wide; thus, compression near the edge

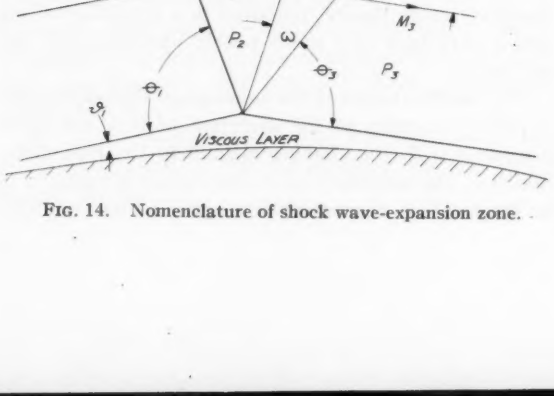

FIG. 14. Nomenclature of shock wave-expansion zone.

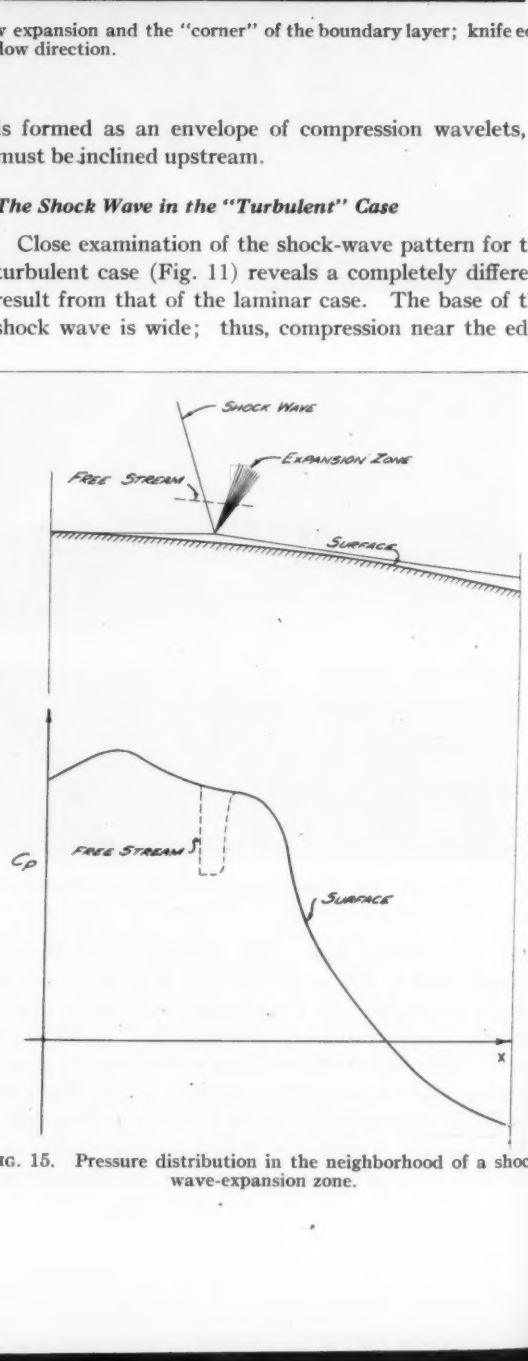

FIG. 15. Pressure distribution in the neighborhood of a shock wave-expansion zone.

of the boundary layer is more nearly continuous. According to the previous discussion, in these cases the flow should behave more in the conventional manner—i.e., corresponding to the classical boundary layer relation. This is borne out by the pressure distributions (Figs. 10 to 12). For this case, a marked increase in pressure is evident at the shock-wave position.

Separation and Shock Wave

The argument presented in the preceding paragraphs concerning the application of results of the classical boundary layer theory also applies to considerations of boundary layer separation. The oft-repeated argument, that the strong pressure gradients associated with a shock wave must cause separation, should be applied with care. The investigations presented here show that separation does not always occur near the shock-wave position. This is, of course, evident in the case of the shock-wave-expansion zone combination. But even in the case of a strong single wave, such as the turbulent shock of Figs. 10 to 12, separation does not occur at the shock position. In fact, comparison of Figs. 11 and 12 shows the separation at approximately the same chordwise position, in spite of an appreciable shift in the location of the shock wave. A pronounced separation is clearly observed in the case of laminar flow at $M = 0.895$. Here, the boundary layer separates *ahead* of the shock wave. A schematic drawing of this condition is presented in Fig. 16.

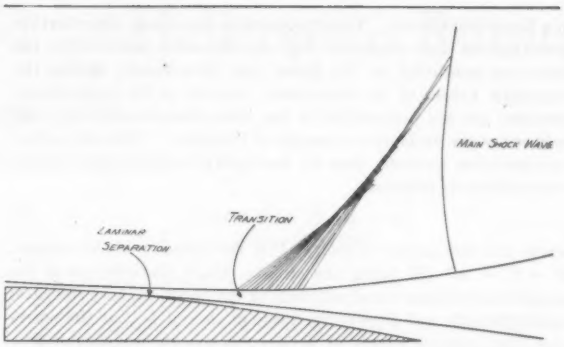

FIG. 16. Boundary layer separation ahead of a shock wave.

CONCLUSIONS

(1) The boundary layer has a pronounced influence upon the shock-wave pattern and pressure distribution in transonic flow. A change of the boundary layer from the laminar to the turbulent régime results in a marked change in shock-wave pattern and surface pressures at the same free stream Mach Number.

The importance of this finding for the interpretation of wind-tunnel results is evident. Effects of this type should also have a considerable influence on the pressure distribution on turbine and compressor blades.

(2) Shock waves can interact with the boundary layer in a manner similar to the reflection of a shock wave from a free surface. The shock wave in this case is followed by an expansion zone; the surface pressure does not show a marked change near the shock-wave base. The pressure gradient normal to the boundary layer is of the same order as the pressure gradient parallel to the boundary layer.

This effect is in striking contrast to the behavior of boundary layers in subsonic flow and is believed to be important for an understanding of supersonic flow near solid surfaces.

(3) It is found that separation does not necessarily occur near the base of a shock wave.

Arguments that postulate the separation due to a shock wave are based upon the classical boundary layer theory, which does not apply in the immediate neighborhood of the shock-wave base.

REFERENCES

[1] von Kármán, Th., *Compressibility Effects in Aerodynamics*, Journal of the Aeronautical Sciences, Vol. 8, pp. 337–356, 1941.

[2] Stack, John, *Compressible Flows in Aeronautics*, Journal of the Aeronautical Sciences, Vol. 12, pp. 127–148, 1945.

[3] Liepmann, H. W., *The 2" × 20" Transonic Wind Tunnel*, Final Rep. for supplemental Agreement Number 1 (S-4843) to Contract No. W 33-038 ac-1717 (11592) with ATSC, Wright Field, 1945.

[4] Liepmann, K., and Liepmann, H. W., *A Dew-point Meter Using Cooling by Expansion of CO_2*, The Review of Scientific Instruments, Vol. 16, No. 2, 1945.

[5] Liepmann, H. W., and Puckett, A. E., *An Introduction to the Aerodynamics of Compressible Fluids;* John Wiley and Sons, Inc., New York, 1946.

Letters to the Editor

Dear Sir:

E. V. Laitone's Letter, to the Editor, published in the August, 1946, issue of the JOURNAL (p. 404), is concerned with a subject upon which the present writer has already commented elsewhere.[1] It was pointed out that there are several variants of the linear-perturbation theory, and by different writers, all of which provide the same results in two-dimensional cases (such as the correction of airfoil characteristics for compressibility effects), but that these variants lead to inconsistent and incompatible results when applied to bodies of revolution in axially symmetric flow.

Unfortunately, this somewhat confused subject was rendered a bit more obscure by the writer's note in the Quarterly, which included the statement that all of these results in the axially symmetric case are equally valid and cannot be distinguished between

in a linearized theory. This statement is erroneous, since further investigation has disclosed that the liberties taken with the boundary condition in the plane case (specifically, fitting the boundary values of the transverse velocity at an approximate location) are *not* permissible in the three-dimensional case, and *only one* of the variants is innocent of this error. Thus the velocity-correction formula loses its ambiguity, and its only correct expression is as follows:

$$(u - U)/U = (1/\beta^2)F(\beta n) \qquad (1)$$

where u is the surface velocity, U is the velocity of the stream, $\beta^2 = 1 - M^2$ (M being the stream Mach Number), n is the parameter defining the slenderness of the body, such as the ratio caliber/length, and $F(n)$ is the value of $(u - U)/U$ at the corresponding point of a body of slenderness n in incompressible flow ($\beta = 1$). This is the result given by B. Göthert.[3] The writer has prepared a second note for publication in the Quarterly which will present these matters in more detail.

Thus, Laitone is correct in his objections to the use of the velocity-correction formula $F(n)/\beta$. Moreover, he is correct in his suggestion that the surface velocity is approximately independent of Mach Number for very slender bodies, because for typical bodies

$$F(n) \leqq n^2 \log n$$

and

$$(1/\beta^2)F(\beta n) \leqq n^2 \log (\beta n) \leqq n^2 \log n$$

provided $n \ll \beta$. But this approximation is not very good for bodies of practical interest, for which $1/10 < n < 1/3$ and $0 < M \leqq 0.8$, say. It is recommended that Göthert's formula, Eq. (1) be used; it results in velocity corrections as great as 40 per cent when applied to ellipsoids of revolution in this régime.

It is of interest also that Sauer's proof that the velocity is independent of β in the limiting case, which Laitone quotes, is really invalid, since it involves an improper integral that does not actually exist. This has been pointed out by Dr. C. C. Lin, of Brown University. Lin has provided a valid proof of the theorem and has arrived at a formula which shows $(u - U)/U$ to be proportional to $n^2 \log (\beta n)$, for small n, *in general*. Previously this form was obtained by Göthert[2] and by the writer[1] only for the special case of ellipsoids of revolution.

REFERENCES

[1] *On Compressible Flow About Bodies of Revolution*, Quart. Appl. Math., Vol. 4, pp. 191–193, 1946.

[2] *Ebene und räumliche Strömung bei hohen Unterschallgeschwindigkeiten*, Lilienthal Gesellschaft f. Luftfahrtforschung, Bericht 127, pp. 97–101, 1940.

W. R. SEARS
Cornell University

Dear Sir:

In a Letter to the Editor which appeared in the August, 1946, issue of the JOURNAL, Edmund V. Laitone pointed out that the "correction factor" $1/\sqrt{1 - M^2}$ is applicable only to two-dimensional subsonic compressible flows and not to three-dimensional flows, as discovered by Ferrari[1] and also by Göthert.[2] However, it is not correct to state that the pressures acting on a slender body of revolution are independent of Mach Number in first approximation. A more careful analysis[3] shows that while the equivalent source-sink distribution for a slender body of revolution is independent of Mach Number in first approximation, the increase with Mach Number of the maximum (positive) axial disturbance velocity, or the maximum negative pressure coefficient on such a body, is approximately given by the following expression:

$$\frac{c_{pM}}{c_{po}} = 1 + \frac{\log \sqrt{1 - M^2}}{0.31 + \log t/c} \qquad (1)$$

where t/c = thickness ratio of the body. (This relation, which was derived by considering a slender ellipsoid of revolution, agrees with the result obtained by Schmieden and Kawalki[4] by a strict application of Göthert's method.) Thus, Mr. Laitone's statement is correct only for the limiting case of a "body" of zero thickness.

Apparently, Sauer[5] and others are led to the conclusion that the pressures are independent of Mach Number because in their analysis the contribution of a source or sink element to the axial disturbance velocity, which is proportional to

$$\frac{(x - \xi)\, f(\xi) d\xi}{(x - \xi)^2 + (1 - M^2)r^2}$$

is replaced by $f(\xi)/(x - \xi)d\xi$. Since the term $(1 - M^2)r^2$ is discarded, the effect of Mach Number on the pressures is also disregarded. It is difficult to justify such a procedure, which amounts to neglecting the logarithmic term in Eq. (1) in comparison with unity. In references 3 and 4 the solution of the linearized partial differential equation for the velocity potential is accepted without further modification, except that in the final result terms of the order of $(t/c)^2 \log (t/c)$ are neglected in comparison with terms of the order of t/c.

REFERENCES

[1] Ferrari, C., *Campi di Corrente Inpersonora Attorno a Solidi di Rivolusione*, L'Aerotecnica, Vol. 17, pp. 507–518, 1937.

[2] Göthert, B., *Ebene und räumliche Strömung bei hohen Unterschallgeschwindigkeiten*, Bericht 127 der Lilienthal-Gesellschaft für Luftfahrtforschung, pp. 97–101, 1940.

[3] Lees, L., *A Discussion of the Application of the Prandtl-Glauert Method to Subsonic Compressible Flow Over a Slender Body of Revolution*, N.A.C.A. T.N. No. 1127, 1946.

[4] Schmieden, C., and Kawalki, K. H., *Beiträge zum Umströmungsproblem bei hohen Geschwindigkeit*, Bericht S 13, (Teil 1) der Lilienthal-Gesellschaft für Luftfahrtforschung, pp. 40–68, 1942.

[5] Sauer, Robert, *Theoretische Einführung in die Gasdynamik;* Springer-Verlag, Berlin, 1943.

LESTER LEES
Assistant Professor of Aeronautical Engineering
Princeton University

Jet Propulsion Applied to Helicopter Rotors

R. H. MILLER*

McDonnell Aircraft Corporation

SUMMARY

Some of the factors affecting jet-driven rotor performance are discussed and it is shown that the relatively high tip speeds required in order to realize a reasonable jet efficiency result in a considerable reduction in the aerodynamic efficiency of the rotor. Although this aerodynamic efficiency may be improved by decreasing the rotor solidity, a practical limit is reached, in the case of jet drives involving airflow through the blades, beyond which the specific fuel consumption increases almost asymptotically with decrease in solidity. However, the weight-saving possible with such drives, and their simplicity, may in certain cases offset their low aerodynamic and propulsive efficiencies. A rough comparative performance and weight estimate are made between conventional and jet-driven helicopters in an attempt to evaluate their relative merits.

INTRODUCTION

THE POSSIBLE ADVANTAGES of a jet-propelled rotor are (1) elimination of antitorque devices, and (2) weight-saving and mechanical simplicity. However, in order to obtain a reasonable jet propulsive efficiency, the rotor should be operated at relatively high tip speeds, which will result in a reduction in the aerodynamic efficiency of the rotor unless the solidity is materially decreased. The minimum rotor solidity, in the case of jet drives involving air or gas flow through the blades, is in turn governed by the necessity for keeping the gas velocities in the blade, and hence the associated pressure drops, to a reasonable value.

Several different jet drives for a helicopter rotor may be envisaged but it is believed that the problems common to most of them may be investigated by considering only the following two basic types:

Type A.—Propulsion by means of a jet with compression provided entirely by virtue of the forward motion of the jet unit located at or near the blade tip, i.e., a ram-jet.

Type B.—Propulsion by means of a jet at the blade tip with centrifugal compression in the hollow blade and additional compression provided by an engine or rotor-driven compressor.

Obviously in the case of Type A, the jet efficiency is independent of the rotor solidity except as structural considerations limit the rotor blade chord for a given jet unit weight. In the case of Type B, the jet efficiency is extremely sensitive to rotor solidity.

Received March 14, 1946.

* Consulting Engineer. Also Assistant Professor of Aeronautical Engineering, Massachusetts Institute of Technology.

NOMENCLATURE

A	=	disc area, sq.ft.
C	=	blade chord
c	=	specific fuel consumption (S.F.C.), lbs. per b.hp.-hr.
c_p	=	specific heat at constant pressure = 0.24
C_T	=	thrust coefficient = thrust/$\rho A\Omega^2R^2$
J	=	mechanical equivalent of heat = 778 ft.lbs. per B.t.u.
M_A	=	weight flow of air, lbs. per sec.
M_F	=	weight flow of fuel, lbs. per sec.
P	=	power, ft.lbs. per sec.
R	=	blade radius, ft.
T	=	temperature, °F. absolute
V	=	tip speed, ft. per sec.
W	=	gross weight, lbs. or work, ft.lbs. per sec.
f	=	equivalent flat plate area—parasite drag or Fanning friction factor
g	=	acceleration of gravity, ft. per sec.^{2}
k	=	ratio of specific heats = 1.4
r	=	pressure ratio
u	=	jet velocity, ft. per sec.
w	=	disc loading, lbs. per sq.ft.
δ	=	profile drag coefficient of rotor blade
σ	=	rotor solidity—ratio of blade area to disc area
Ω	=	rotor speed, rad. per sec.
ρ	=	density of air = 0.002378 lbs. sec.^{2} per ft.^{4}
η	=	efficiency of jet drive
η_m	=	mechanical efficiency of rotor drive: ratio of shaft to brake horsepower
η_t	=	thermal efficiency of engine
μ	=	ratio of forward speed to tip speed

SECTION I. AERODYNAMIC EFFICIENCY OF THE ROTOR

In order to permit an evaluation of the effects of changes in tip speed and solidity on the aerodynamic efficiency of a rotor, the weight that may be lifted for a given shaft horsepower and the maximum range for a given ratio of fuel load to gross weight will be established as a function of solidity and tip speed.

The well-known formula for the hovering helicopter, assuming constant profile drag, δ, gives for the torque coefficient

$$C_Q = \sigma\delta/8 + C_T\sqrt{C_T/2}$$

which may be expressed in terms of power and weight as

$$\frac{P}{W} = \frac{\sigma\delta}{8}\left(\frac{\rho}{w}\right)\Omega^3R^3 + \sqrt{\frac{w}{2\rho}}$$

This has been plotted in Fig. 1, in terms of lbs. per shaft hp., against σ for various tip speeds and disc loadings.

Additional information as to the vertical rate of climb for a given excess power, ΔP (in ft.lbs. per sec.) over

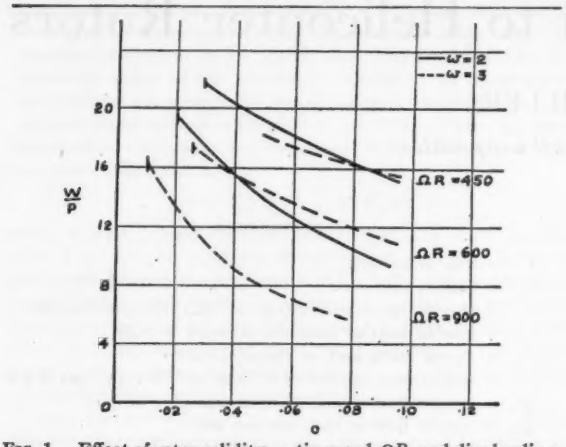

FIG. 1. Effect of rotor solidity, σ, tip speed, ΩR, and disc loading, w, on power required to hover.

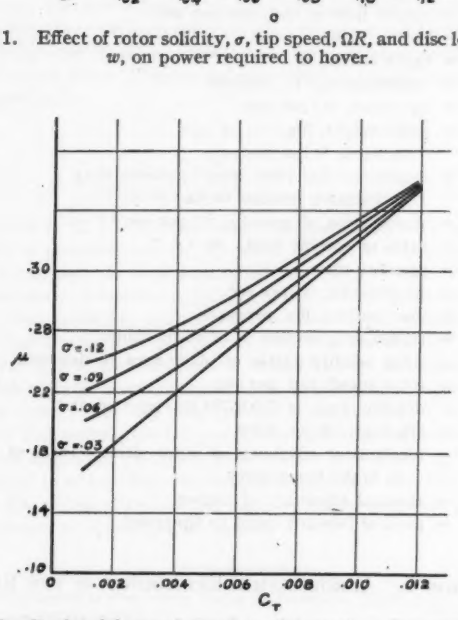

FIG. 2. Ratio of forward speed to tip speed, μ, for maximum range for various thrust coefficients and solidities.

that required for hovering as obtained from Fig. 1, may be readily determined, for a constant-speed rotor, from the relationship

$$\text{Vertical rate of climb} = \frac{\Delta P}{W}\left(\frac{\Delta P/W + 2\sqrt{w/2\rho}}{\Delta P/W + \sqrt{w/2\rho}}\right)$$

in ft. per sec. which may be derived from the standard formulas for vertical climb.

The range at any forward velocity, $\mu\Omega R$, may be closely approximated from the formula

$$\text{Range} = \frac{375\mu\,\Delta C_T\,(\eta_s/c)}{(\sigma\delta/8)(1+n\mu^2) + (C_T^2/2\mu) + (f/A)(\mu^3/2)} \text{ in miles}$$

n may be taken as 4.6 and f/A, the "drag coefficient" based on disc area for the helicopter less rotor, as 0.010.

ΔC_T is the increment of thrust coefficient represented by the fuel. C_T should be based on the average gross weight.

The value of μ for maximum range may be established by solving for μ in the formula

$$\frac{\sigma\delta}{8} = \frac{(C_T^2/\mu) - (\mu^2 f/A)}{n\mu^2 - 1}$$

the solution of which has been plotted in Fig. 2 for a drag coefficient f/A of 0.010 and a value of δ of 0.012.

The maximum range has been determined for various values of tip speed, disc loading, and solidity, and plotted against solidity in Fig. 3. These curves, and those of Fig. 1, have been stopped at a minimum rotor solidity corresponding to a blade angle of attack of 10°. Beyond this angle of attack, which is believed to be the maximum desirable operating angle of attack, the drag coefficient increases rapidly and the assumption of a constant drag coefficient, $\delta = 0.012$, no longer holds. Fig. 3 is based on a fuel load of 7.5 per cent of the gross weight, but for any other fuel load it may be assumed, as a close approximation, that the range increases proportionately to the increase in fuel. It is evident from Figs. 1 and 3 that operation at higher tip speeds entails a considerable loss in both cruising and hovering performance unless the solidity is decreased accordingly.

However, the reduced power-plant and transmission weights and the elimination of the antitorque rotor result in a considerably lighter helicopter when a jet rotor drive is used. It would therefore appear possible, by increasing the fuel load and shaft horsepower, to equal or exceed the performance of a conventional helicopter without sacrificing the load-carrying capacity. This will be investigated in the next sections.

Losses due to compressibility effects, which may be appreciable at the higher tip speeds and lower solidities, have been neglected in the preparation of the curves of Figs. 1 and 3.

SECTION II. JET EFFICIENCIES

Ideal Cycle Efficiencies

For any jet operating at a pressure ratio r (defined as the ratio of combustion chamber pressure to atmos-

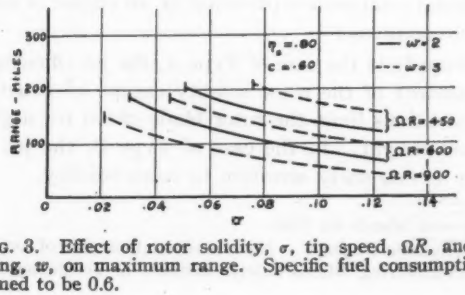

FIG. 3. Effect of rotor solidity, σ, tip speed, ΩR, and disc loading, w, on maximum range. Specific fuel consumption, c, assumed to be 0.6.

pheric pressure) the work of compression per pound of air is

$$W_c = Jc_pT_0(r^{(k-1)/k} - 1)$$

where

J = mechanical equivalent of heat—778 ft.lbs. per B.t.u.
c_p = specific heat at constant pressure = 0.24
$k = c_p/c_v = 1.4$ for air at standard temperature

whence $(k-1)/k = 0.286$, which will be used hereafter.

T_0 = ambient air temperature = 520°F. absolute

This work of compression may be supplied by any means and may be assumed independent of the rotor speed. The work done in accelerating one pound of air to the rotor tip speed, V, is

$$W_a = V^2/2g$$

The total work available from the jet per pound of charge air is

$$W_j = uV/g$$

where u is the jet velocity. If the velocity in the combustion chamber is assumed to be negligible in comparison with V, then

$$u = \sqrt{-2gJc_pT_2\ [(1/r^{0.286}) - 1]}$$

where T_2 is the combustion chamber temperature.

For combustion at constant pressure, the temperature of the gases in the combustion chamber, T_2, is given closely by

$$M_F/M_A = c_p(T_2 - T_1)/18{,}000$$

where

M_F = weight flow rate of the fuel
M_A = weight flow rate of the air
18,000 = heat content of the fuel, including an overall combustion chamber efficiency of 90 per cent
T_1 = temperature of air entering the combustion chamber = $T_0r^{0.286}$

The total work available in the fuel is, assuming 20,000 B.t.u. per lb.,

$$W_f = JM_F(20{,}000)$$
$$= Jc_pM_A(T_2 - T_1)(20{,}000/18{,}000)$$

and the total work available per pound of charge air is then

$$W_f = Jc_p(1/0.90)(T_2 - T_1)$$
$$= 208(T_2 - T_1)$$

When compression is provided entirely by the rotor, by a combination of centrifugal compression in the blades and a rotor-driven compressor, then the overall efficiency of the drive is given by

$$\eta = (W_f - W_a - W_c)/W_F$$

$$\eta = \frac{\frac{V}{g}\sqrt{-2gJc_pT_2\left(\frac{1}{r^{0.286}} - 1\right)} - \frac{V^2}{2g} - Jc_pT_0(r^{0.286} - 1)}{208(T_2 - T_1)}$$

This relationship has been plotted against r for various values of T_2 in Figs. 4a, 4b, and 4c for rotor tip speeds of 600, 900, and 1,120 ft. per sec. If the work of compression is supplied only by ram or centrifugal compression in the rotor blade, the work of compression, W_c and W_a are

$$W_c + W_a = V^2/g$$

The pressure ratios corresponding to pure ram compression are indicated in Fig. 4 and these points represent the efficiencies of jets of Type A.

The favorable pressure distribution on the forward end of a ram-jet resulting from the external airflow induced by the jet may increase these efficiencies by a considerable amount but no attempt is made here to evaluate these effects.

If additional compression is provided by means of an engine-driven compressor, rather than by a rotor-driven compressor, the overall efficiency is given by the expression

$$\eta = \frac{\frac{V}{g}\sqrt{-2gJc_pT_2\left(\frac{1}{r^{0.286}} - 1\right)} - \frac{V^2}{g}}{208(T_2 - T_1) + \frac{Jc_pT_0}{\eta_e}(r_1^{0.286} - 1)}$$

where V^2/g is the work of acceleration and compression in the blade and r_1 is the pressure ratio across the engine-driven compressor. If r_2 is the compression due to centrifugal forces in the blade, then $r = r_2r_1$. η_e is the overall thermodynamic efficiency of the engine used to drive the compressor.

Figs. 5a, 5b, and 5c show the efficiency plotted against pressure ratio for this combination, assuming a thermodynamic efficiency for the engine of 25 per cent

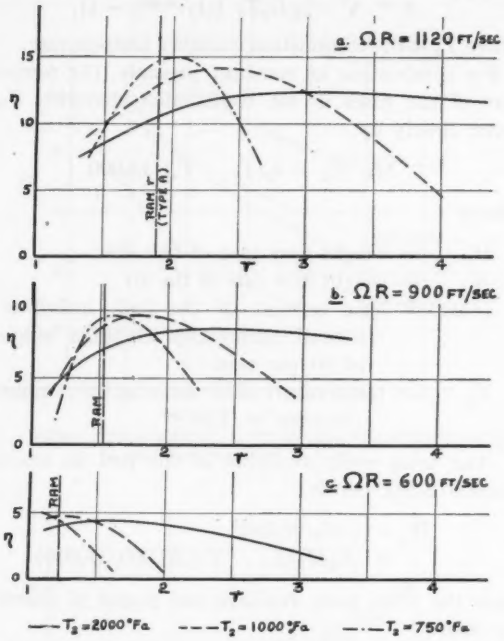

FIG. 4. Theoretical efficiency of Type B jets, with additional compression provided by a rotor-driven compressor, for various combustion chamber temperatures, T_2, and pressure ratios, r.

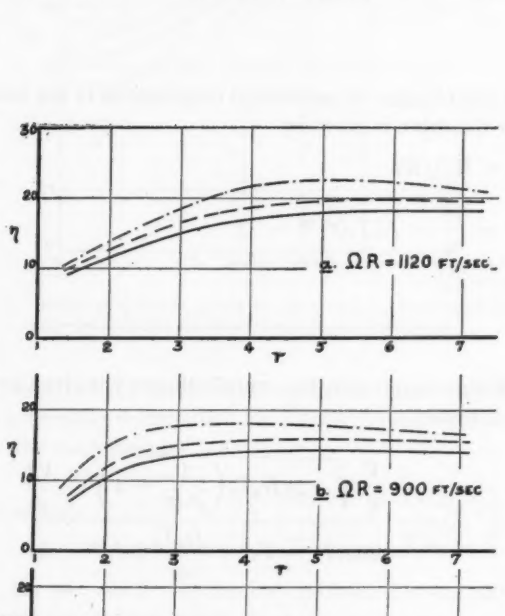

FIG. 5. Theoretical efficiency of Type B jets, with additional compression provided by an engine-driven compressor, for various combustion chamber temperatures, T_2, and pressure ratios. r.

corresponding to a specific fuel consumption of 0.6 lb. per b.hp.-hr.

Figs. 4 and 5 cover all possible combinations of the two types of jet drives, A and B, listed above.

All of the above efficiencies are theoretical ideal efficiencies, i.e., no compressor, turbine, or nozzle losses have been considered, although a combustion efficiency of 90 per cent has been included in order to keep combustion and cycle losses separate.

In addition, the following assumptions, which it is believed have little effect on the final results, have been made:

(1) The velocity of the air leaving the compressor and in the rotor blades is small compared to the velocity of the jet and the velocity of the blade tip.

(2) The value of c_p is constant and equal to 0.24. This neglects the variation of c_p with temperature and gas content. The same assumption has been made with regard to k.

(3) Combustion occurs at constant pressure and with a negligible change in combustion chamber velocity.

These assumptions, and further assumption of zero nozzle losses, have little effect on the final results.

However, neglecting the pressure losses through the blades and combustion chamber has a considerable effect on the absolute value of the overall efficiencies shown in Figs. 4 and 5, although the relative values will not be appreciably affected. Provided the velocity of flow through the blade is kept below 200 ft. per sec., the blade and combustion chamber losses are negligible, but in order to maintain this velocity it may be necessary to provide a rotor with an excessively high solidity. The effect of these major losses on the specific fuel consumption will be investigated next.

Effect of Losses on Specific Fuel Consumpton

The main losses in efficiency associated with a jet rotor drive for a helicopter arise as the result of:

(a) The necessity for pumping a considerable amount of air through the blades if a reasonable shaft horsepower is to be realized.

(b) The necessity for keeping the dimensions of the combustion chamber located at the blade tip as small as possible in order to minimize the external drag. This increases the velocity of the gases in the combustion chamber and, consequently, the pressure drop across it.

Loss (a) does not occur in the case of a ram-jet, but loss (b) may be more severe because of the low pressure ratio available.

Since an increase in solidity for the purpose of reducing these losses to a negligible value results, beyond a certain point, in a considerable decrease in the aerodynamic efficiency of the rotor, the limits between excessive losses in drive efficiency and excessive losses in aerodynamic efficiency must be established.

In order to estimate the lowest practical solidity for a given horsepower and rotor diameter, the losses in the blade have been estimated assuming a Fanning friction factor of 0.01, and the pressure drop through the combustion chamber has been assumed to be four times the dynamic pressure at the chamber inlet, with an inlet velocity equal to the velocity in the blade.

In the case of jet B, an overall compressor efficiency of 75 per cent has been assumed, which is intended to include a compressor efficiency of 85 per cent, the maximum that may be realized with an axial flow compressor, and pumping losses of 10 per cent. These pumping losses arise as a result of the pressure drops associated with the airflow to the blades through the fuselage ducts and past the flap and lag hinges.

In estimating the pressure drop through the blades, the density corresponding to the average temperature and pressure in the blade for the conditions being investigated has been used.

In the case of the ram-jet (Type A), a combustion chamber velocity of one-quarter of the forward velocity and an entrance and diffuser loss of 5 per cent of the available ram have been assumed. Entrance losses have been neglected with jets of Type B because of the ram available due to the motion of the helicopter.

Taking these losses into account, the specific fuel consumption for jets of Type B with a rotor-driven compressor and with an engine-driven compressor and jets of Type A has been plotted against the rotor solidity, σ, in Fig. 6 for a tip speed of 600 ft. per sec. In addition, the fuel consumption for jets of Type B with engine drive and a ram-jet has been plotted for a tip speed of 900 ft. per sec.

A 40-ft. diameter, two-bladed rotor has been assumed with an available net shaft horsepower of 150 hp. It is at once clear from an examination of Fig. 6 that a definite minimum rotor solidity exists for any type of jet drive using the blades as air passages. Since an increase in pressure drop results in a decrease in shaft horsepower, which in turn requires an increase in airflow resulting in a greater pressure drop, it is evident that, for a given shaft horsepower, when the critical solidity is reached the S.F.C. increases almost asymptotically. Operation at any point other than the flat portion of the curve would be, in practice, impossible. In the case of the jets of Type B with a rotor-driven compressor, the minimum solidity is far too high for aerodynamic efficiency because of the necessity for supplying by means of the relatively inefficient rotor not only the 150 shaft hp. but also the power to drive the compressor. Such a type of rotor would therefore appear to be of little practical use for helicopters.

While the curves of Fig. 6 have, of necessity, been prepared for a specific rotor diameter and horsepower, the effect of various changes may be roughly estimated from the following considerations.

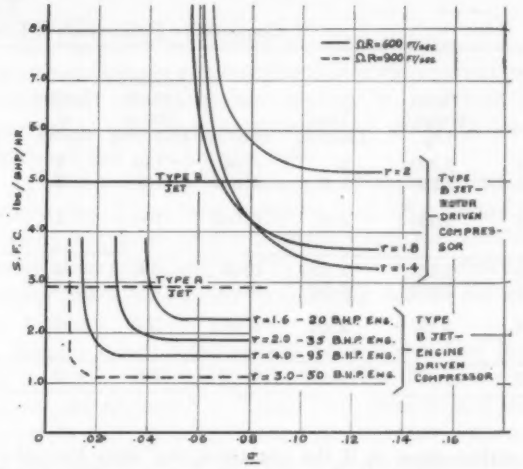

FIG. 6. Effect of rotor solidity, σ, on specific fuel consumption for various types of jet drives. Combustion chamber temperature in all cases is 2,000°F. abs.

The available shaft horsepower is a direct function of the mass flow, M, of air through the blade. The pressure drop, Δp, through the blade is approximately a function of the square of the velocity, V, which, for given operating conditions, is a function of the mass flow divided by the cross-sectional area of the blade. The cross-sectional area of the blade is a function of the square of the blade chord, c.

Therefore,

$$\Delta p = f(V^2) = F(M/c^2)^2$$

whence for a given Δp, which is the major factor in determining the minimum rotor solidity, the maximum horsepower that may be supplied to the rotor varies as the square of the blade chord, or solidity.

Thus, with a jet of Type B, $\gamma = 2$, and an engine-driven compressor, if the solidity were increased from the minimum of approximately 0.04 to 0.06, the maximum permissible rotor horsepower could be increased from 150 hp. to 150 $(0.06/0.04)^2$ or 338 hp. without any appreciable increase in S.F.C.

Also, if a single-rotor blade were used instead of two blades and the solidity were kept at 0.04, the cross-sectional area would double and the maximum permissible horsepower would also double to 300 hp. Actually, the increase would be slightly greater because of the reduction in wetted area, as discussed below. Conversely, if the horsepower were held at 150 hp., the solidity could be reduced to $0.04(1/\sqrt{2})$ or 0.028.

The pressure drop has been given above as a function of the chord to the fourth power. Actually, for the blade

$$\Delta p = {}^1/_2 \rho V^2 f \times \frac{\text{perimeter}}{\text{cross-sectional area}} \times \text{blade length}$$

where f is the Fanning friction factor. The pressure drop along the blade, therefore, varies inversely as

TABLE 1
Comparative Performance of Jet-Driven and Conventional Helicopters

	Gross Weight, Lbs.	Disc Loading	Solidity	Available Shaft Hp. at Hovering	Number of Blades	Tip Speed	Fuel—Gal.	Maximum Range—Miles	Vertical Rate of Climb—Ft. per Min. at Sea Level	Notes
1	2,500	2	0.06	140	3	450	30	192	0	Conventional helicopter
2	2,250	1.8	0.045	150	2	600	68	127	0	Jet Type B engine-driven compressor
3	2,330	1.9	0.032	150	1	600	80	192	370	Jet Type B engine-driven compressor
4	5,000	2.55	0.06	350	3	450	75	275	800	Conventional helicopter
5	5,450	2.80	0.06	505	2	600	285	275	1,710	Jet Type B engine-driven compressor
6	5,150	2.62	0.043	505	1	600	240	275	2,480	Jet Type B engine-driven compressor
7	1,060	3.00	0.020	100	2	900	30	80	1,000	Ram-jet-driven rotor

c^5 rather than c^4, if the variation of f with Reynold's Number is neglected. However, the combustion chamber pressure drop, which varies more closely as c^4, represents approximately half the total pressure drop between the blade root and the jet. Assuming Δp to be a function of c^4 is therefore slightly conservative for increasing solidities and slightly nonconservative for decreasing solidities.

If the rotor diameter were increased and the solidity remained constant, the only pressure drop effected would be that due to friction in the blade which varies with c^5. However, there is an increased pressure drop due to the increased blade length resulting in a net variation proportional to c^4, as before. Thus, if the rotor diameter were increased to 50 ft. and the solidity remained the same, the permissible shaft horsepower at the minimum solidity of 0.04 for the example taken above would become $150(50/40)^2$ or 224 hp. If the solidity were increased to 0.06, the permissible horsepower would become $224(0.06/0.04)^2$ or 505 hp. The power required from the engine driving the compressor would increase directly as the increase in rotor power to 35(505/150) or 120 b.hp.

SECTION III. COMPARATIVE PERFORMANCE OF JET AND CONVENTIONAL HELICOPTERS

In order to obtain approximate comparative performance estimates for a helicopter with a jet-propelled rotor and one with a conventional rotor drive, the following weight estimates will be used.

(a) *Conventional helicopter, 40-ft., three-bladed rotor, 180-b.hp. engine:*

(1) Gross weight = 2,500 lbs.
(2) Fuel weight, including tanks = 200 lbs. (30 gal.).
(3) Weight of complete power plant, less anti-torque device = 600 lbs.
(4) Weight of tail rotor, including supporting structure and transmission = 250 lbs.
(5) Rotor group = 350 lbs.
(6) Weight less items 2, 3, 4, and 5 = 1,100 lbs.

(b) *Equivalent jet-propelled helicopter, with Type B jet, 35-b.hp. engine driving the compressor (see Fig. 6)—using item (a6) above as a base:*

(1) Weight of power plant, compressor, gearing and ducts = 250 lbs.
(2) Rotor group = 450 lbs.
(3) Gross weight, less fuel: items (a6) plus (b1) and (b2) = 1,800 lbs.

(c) *Conventional helicopter, 50-ft. rotor, 450-b.hp. engine:*

(1) Gross weight = 5,000 lbs.
(2) Fuel weight, including tanks = 500 lbs. (75 gal.).
(3) Power plant, as in (a3) above = 1,250 lbs.
(4) Tail rotor, as in (a4) above = 500 lbs.
(5) Rotor group = 550 lbs.
(6) Weight less items 2, 3, 4, and 5 = 2,200 lbs.

(d) *Equivalent jet-propelled helicopter, with Type B jet, 125-b.hp. engine driving the compressor—using item (c6) above as a base:*

(1) Weight of power plant, as in (b1) = 700 lbs.
(2) Rotor group = 650 lbs.
(3) Gross weight, less fuel: items (c6) plus (d1) and (d2) = 3,550 lbs.

(e) *Ram-jet-propelled helicopter*—this will be estimated in a different manner because of the extreme simplicity of construction possible with this type of jet. The following weights are assumed:

Rotor	150 lbs.
Fuselage	200 lbs.
Landing gear	50 lbs.
Electrical equipment	40 lbs.
Controls	20 lbs.
Crew (2)	400 lbs.
Fuel and tank	200 lbs.
Total gross weight	1,060 lbs.

The only limits on the minimum solidity of such a rotor are structural, since no air is pumped through the blades. A minimum practical solidity of 0.02 will be assumed.

Table 1 has been prepared on the basis of the foregoing weight estimates, the aerodynamic performance data of Figs. 1 and 3, and the specific fuel consumption of Fig. 6. The effect of changes in disc loading and fuel load has been estimated by interpolation and extrapolation of Figs. 1 and 3. The effect of changes in solidity, number of blades, and diameter from that assumed in Fig. 6 has been estimated as described in Section II.

It is evident from Table 1 that except for the ramjet (7) it will probably be possible in every case to exceed the performance of a conventional helicopter, provided that a single-blade rotor could be built and made to operate satisfactorily. If a two-bladed rotor is used, the performance will be still better, except for the case of the light helicopter with a jet rotor of Type B, which has less range than the conventional helicopter.

Although the fuel load of the jet helicopter is in all cases considerably greater than that of the conventional helicopter, this does not necessarily represent an increase in operating costs because of the much lower grades of fuel that may be used.

In estimating the performance of the conventional helicopters, it has been assumed that, after deducting cooling fan, drive, and antitorque losses, the net shaft horsepower remaining is 77½ per cent of the available engine brake horsepower in hovering and 85 per cent in cruising.

Several other combinations of solidity, fuel load, shaft power, and tip speed other than those investigated and presented in Table 1 are possible and may result in even better jet rotor performance, although at the expense of an increase in gross weight. However, it is believed that the general trend is clearly indicated by the estimates of Table 1.

Letter to the Editor

Dear Sir:

From the Schlieren photographs and discussion given by Stack in the Eighth Wright Brothers Lecture,[1] the writer developed the boundary layer-shock interaction theory explained in reference 2.

The flow patterns shown in Fig. 1 may be constructed as shown in reference 2 from the following considerations:

(a) The Mach waves or infinitesimal oblique shocks are inclined to the local velocity vector at the angle

$$\theta_w = \sin^{-1}(1/M_L) \qquad (1)$$

(b) The local supersonic isentropic flow compression ($H_L = H_\infty$) produced in the contraction of the stream tube above the thickening boundary layer is given by

$$\frac{p_L/H_\infty}{p_1/H_\infty} \approx 1 + \frac{\gamma M_1^2}{\sqrt{M_1^2 - 1}}\,\theta_S + \frac{\frac{\gamma^2+\gamma}{4} M_1^6 - \gamma M_1^4 + \gamma M_1^2}{(M_1^2 - 1)^2}\,\theta_S^2 \qquad (2)$$

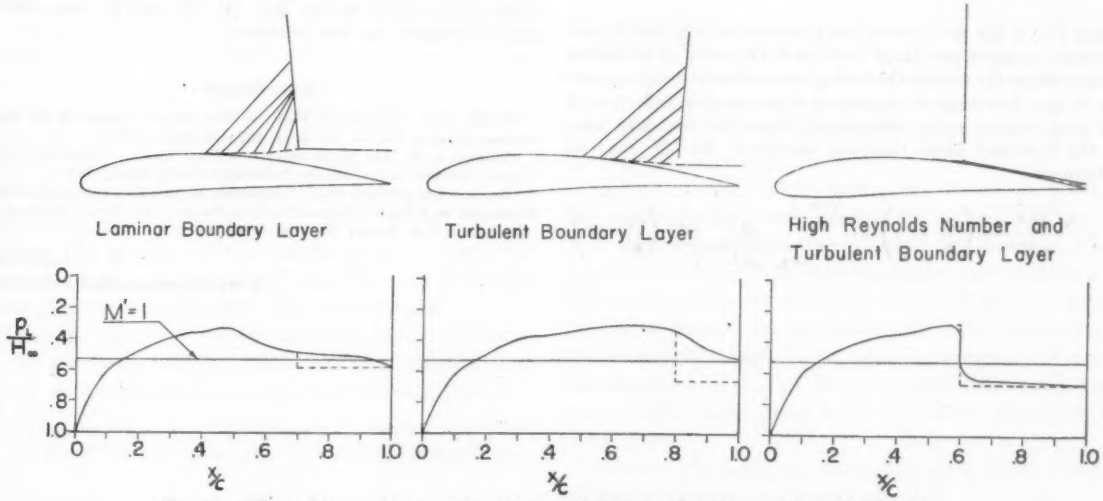

FIG. 1. Effect of increasing boundary layer turbulence or free-stream Reynolds Number.

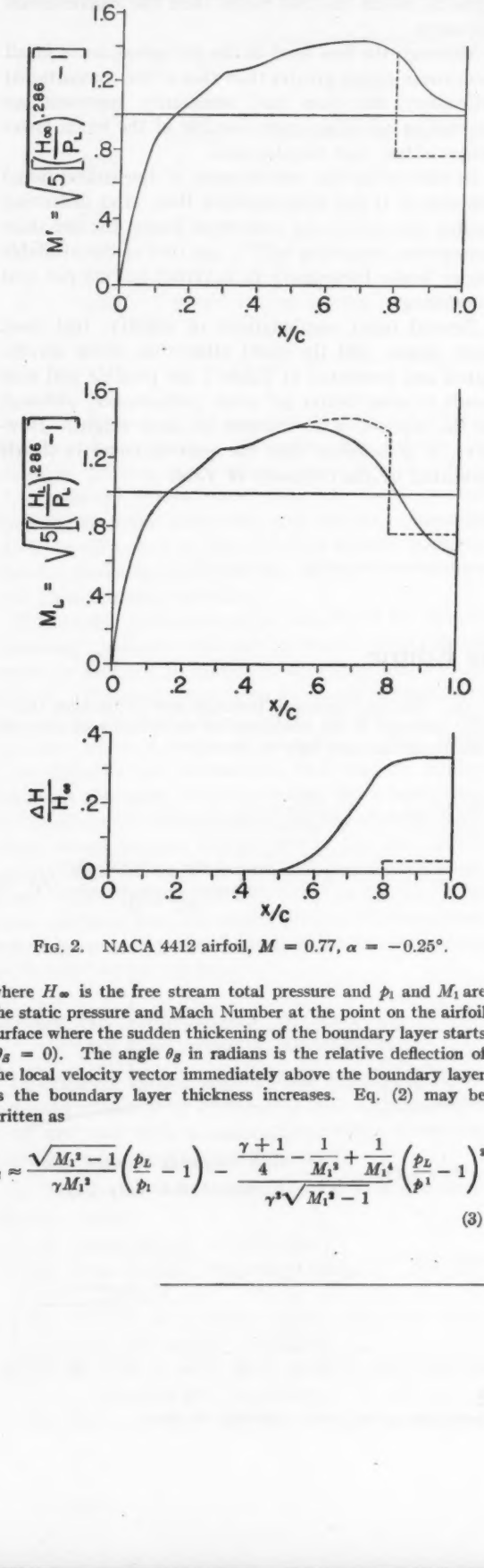

FIG. 2. NACA 4412 airfoil, $M = 0.77$, $\alpha = -0.25°$.

where H_∞ is the free stream total pressure and p_1 and M_1 are the static pressure and Mach Number at the point on the airfoil surface where the sudden thickening of the boundary layer starts ($\theta_S = 0$). The angle θ_S in radians is the relative deflection of the local velocity vector immediately above the boundary layer as the boundary layer thickness increases. Eq. (2) may be written as

$$\theta_S \approx \frac{\sqrt{M_1^2 - 1}}{\gamma M_1^2}\left(\frac{p_L}{p_1} - 1\right) - \frac{\frac{\gamma+1}{4} - \frac{1}{M_1^2} + \frac{1}{M_1^4}}{\gamma^2\sqrt{M_1^2 - 1}}\left(\frac{p_L}{p_1} - 1\right)^2 \qquad (3)$$

Fig. 1 indicates that the sudden boundary layer thickening produces isentropic flow compression and decreases the supersonic flow velocity until the local Mach Number (M_L) approaches unity or the boundary layer cannot separate any further. The final flow compression to a subsonic flow is then accomplished by means of a small normal shock. As the amount of boundary layer separation which the given flow can produce is reduced, the final normal shock increases in magnitude as indicated in Fig. 1.

Although the flow above the boundary layer (dotted line) has become subsonic behind the normal shock, Fig. 1 indicates that the flow inside the thickened boundary layer (solid line indicating pressures on airfoil surface) may still be supersonic. This is not so, however, as may be seen by an analysis in Fig. 2 of the total pressure measurements inside the boundary layer. The total pressure loss given at $x/c = 1$ was taken from reference 3 as the measurement near the airfoil trailing edge. The total pressure loss inside the boundary layer was then faired in accordance with the derivation in reference 2. The experimental total pressure loss through the normal shock was in exact agreement with that predicted by theory so the variation of total pressure was taken as the sudden discontinuity predicted by theory.

Fig. 2 shows that the actual local Mach Number inside the boundary layer has become subsonic due to the total pressure loss from viscosity effects. It is seen that throughout the isentropic supersonic flow compression the static pressure p_1 is continuous as in ordinary boundary layer theory but only up to the normal shock. Downstream of the normal shock there is a pressure discontinuity between the flow inside and outside of the boundary layer in agreement with the Schlieren photographs of reference 1. However, the static pressure inside the boundary layer is less, not greater, than that of the flow outside the boundary layer.

Consequently, it is not necessary to assume that only the sudden pressure gradient of a shock wave produces the abrupt boundary layer thickening. Actually, if the boundary layer Reynolds Number is such that an infinitesimal pressure increase produces a thickening of the boundary layer, then a Mach wave or infinitesimal oblique shock arising from any temporary disturbance can start the thickening of the boundary layer and the resulting isentropic flow compression that will then continue until it finally concludes in a small normal shock. If the boundary layer is sensitive to an increase in the pressure gradient, then the initial thickening will be abrupt and the initial Mach waves or infinitesimal oblique shocks will tend to converge and form a finite oblique shock. However, this will still be a relatively weak oblique shock so that Eqs. (1), (2), and (3) may still be used to compute the flow relations.

REFERENCES

[1] Stack, John, *Compressible Flows in Aeronautics*, Journal of the Aeronautical Sciences, Vol. 12, No. 2, pp. 127–143, April, 1945.

[2] Laitone, E. V., *The Initial Shock in a Local Region of Supersonic Flow*, Cornell Aeronautical Laboratory Publication No. 4, April, 1946.

[3] Stack, John, Lindsay, W. F., and Littell, Robert E., *The Compressibility Burble and the Effect of Compressibility on Pressures and Forces Acting on an Airfoil*, N.A.C.A. Report No. 646, 1938.

E. V. LAITONE
Cornell Aeronautical Laboratory

Newton and Fluid Mechanics

J. C. HUNSAKER*

National Advisory Committee for Aeronautics

NEWTON'S CONCEPTION OF DYNAMICS armed his successors of the next three centuries with basic tools with which they erected the great structure of modern engineering science.

While Newton is claimed by mathematicians and astronomers as their own, engineers owe to him the very foundation of their art. Modern aerodynamics is completely Newtonian in its development. Not only is it a consequence of Newton's laws of motion, but to this day it continues to utilize some of his original tactics to obtain solutions.

For example, Newton, being unable to determine from first principles the resistance of a body moving through a real fluid, simplified his problem by separating it into three parts. He postulated, first, a special frictionless incompressible fluid, then a viscous fluid, and finally, a compressible fluid.

For the frictionless fluid, he deduced that there would be a resistance due to the impact of fluid particles, varying as the fluid density, as the square of a linear dimension of the body, and as the square of the velocity of motion.

For the second fluid, having "a want of lubricity" or viscosity, he concluded that the frictional force must vary as the rate of shear of adjacent layers of fluid. This is a clear definition of the coefficient of viscosity and the basic characteristic of laminar flow. To this day we speak of tars and greases as non-Newtonian fluids, because they do not exhibit this linear relation between force and rate of shear.

Finally, he speculated on the propagation of pressure pulses, like sound waves, in a compressible fluid and found the velocity of propagation to be a function of the density and elasticity of the fluid. His computation for the velocity of sound in air was a fair approximation which stood until La Place corrected it for adiabatic rather than isothermal conditions.

From the concept of the ideal frictionless fluid comes the classical hydromechanics of Bernoulli, Euler, d'Alembert, and Lagrange.

From the concept of the viscous fluid we have the great development by Stokes and Osborne Reynolds leading to Prandtl's boundary layer mechanics.

From the concept of compressibility, we are just now evolving a comprehensive mechanics of supersonic flow to cope with the engineering needs of modern flight.

Newton's ideas are as old as reason and as new as research. Their timelessness is shown by three simple instances.

Newton clearly stated that his laws of motion imply that it does not matter whether a body be fixed and the fluid flow over it or whether the body move through a fluid at rest. This kind of relativity is the justification for the wind-tunnel testing by the Wright Brothers and their followers in aerodynamic research.

A second example of old and new is the modern wing theory which accounts for lift as the reaction to the force that communicates downward momentum continuously to the air. Froude applied the same reasoning to marine propulsion.

The third instance is the newest style of all—jet propulsion. Jet propulsion as a device of mechanics is certainly Newtonian in principle. The propulsion is the third law reaction to the second law force, as measured by the rate at which momentum is created in the jet. While Newton is said to have speculated about a jet-propelled steam carriage, certain marine creatures were making use of a propulsive jet very much earlier and might claim priority in geological time.

TWO BRANCHES OF FLUID MECHANICS

Leaving aside compressible and supersonic flows, I would like next to outline how the two great branches of fluid mechanics, frictionless flow and viscous flow, each starting with Newton, have independently developed over three centuries and now, in our time, have at last been brought together as a powerful instrument of aeronautical science. And finally, I shall have the honor to describe the successful engineering application of this new instrument of ancient lineage in the laboratory of the National Advisory Committee for Aeronautics; a laboratory named for Samuel P. Langley, an astronomer turned aeronautical scientist.

I refer to the so-called laminar flow or low-drag wing, derived from theory and applied during the late war to both fighter and bomber airplanes. Its practical form is no longer a secret as, unfortunately, our enemies obtained samples from Mustangs that fell to their guns. This wing permits an airplane to fly faster and farther by virtue of its lower drag. By a coincidence, the pressure distribution that promotes smooth airflow also permits a higher flight speed before the onset of compressibility shock.

To trace the pedigree of the low-drag wing, I must start with Newton, as I have intimated.

Presented at the Newton Tercentenary Celebration, sponsored by the Royal Society, Cambridge University, England, July, 1946.

* Chairman.

Frictionless Flow

Newton's dynamical concepts and his tactic of postulating an ideal fluid were taken up promptly by Daniel Bernoulli, who deduced the relation between pressure and velocity in his famous law of conservation of *vis viva*. d'Alembert further developed the concept of the frictionless fluid, showed how fluid should close in smoothly behind a body moving through it and so arrived at his Paradox of Zero Resistance. Euler formulated the mathematical statement of the problem and introduced a velocity potential such that its derivative in any direction was the velocity component.

These three were the founders of classical hydrodynamics. They were followed by the 19th century giants, Helmholtz, Kirchoff, Kelvin, and Rayleigh who contributed an understanding of the vortex, surfaces of discontinuity, and jets. Rankine showed how combinations of sources and sinks could be used to give ideal forms for ships.

At the beginning of this century, an elaborate structure of applied mathematics had been built up from the hydromechanics of the ideal fluid but its conclusions were almost as remote from the behavior of real fluids as in Newton's time. The subject was practically sterile.

Such a static situation, however, was destined to be saved by the pioneers of early flight. It was discovered by practical men with no knowledge of hydromechanics that an arched wing profile was advantageous. Lanchester in England, Kutta in Germany, and Joukowski in Russia independently accounted for this fact by the concept of circulation around the wing, increasing velocity over the upper surface. Even in the ideal fluid, which gave no resistance, a strong normal force or lift was predicted. Lanchester furthermore showed how a wing would cause the air to rise to meet it and then descend and that a vortex would trail behind each wing tip. He gave a physical picture of the flow which accounted for both lift and drag in a frictionless fluid and thus finally disposed of d'Alembert's paradox of no drag. Joukowski, by a conformal transformation of a wing into a cylinder, computed the pressures on the wing from the velocity field.

The picture was completed by Prandtl during the first World War. He paralleled and extended Lanchester's qualitative work and produced a complete airfoil theory of immense value to engineers. The theory was still in the domain of the ideal frictionless fluid and did not account for profile drag. This was left for wind-tunnel tests to determine.

Viscous Flow

Now to return to the other Newtonian concept, the viscous fluid.

No such elaborate structure as hydromechanics was developed for the mechanics of viscous fluids. Experimenters, or shall I say physicists, rather than mathematicians, dealt with such real fluids. However, early in the 19th century Stokes solved the equations of motion of a Newtonian viscous fluid and enunciated ideas that led to great advances.

Osborne Reynolds, from careful observation of the flow of viscous liquid in tubes, distinguished two forms of motion, laminar and turbulent, with an abrupt transition from the first to the second. By analysis, he found the determining factor to be a relation between velocity, tube diameter, density, and viscosity. This relation is a nondimensional coefficient, now known as the Reynolds Number, and is a criterion of dynamical similitude. It expresses the ratio between inertial and viscous forces in the fluid.

That turbulent flow in pipes involved much more friction than laminar flow was recognized almost as soon as the controlling variables were distinguished. However, the flow was much too complex to be amenable to simple analysis as for laminar flow, and experiments were confused by the indefinite nature of surface roughness.

Prandtl in 1904 had shown that, at sufficient speed, the effects of viscosity must be largely confined to regions of fluid close to the boundary surfaces. This boundary layer contains the mechanism for transmission of shear stress and profile drag to the wing.

Blasius (1908) calculated, and verified experimentally, the force-momentum relations for the laminar boundary layer in terms of the velocity gradient or rate of shear in the Newtonian manner. Later, Tollmein (1935) discussed the stability of such laminar flow.

Consideration of this theoretical work, supported by experimental evidence from B. M. Jones (1938) and others, led to the conclusion that a smooth surface and a falling pressure gradient are necessary to maintain an extensive laminar flow at high Reynolds Number. Otherwise, there is a prompt transition to turbulence.

The force-momentum relations for a turbulent boundary layer on a flat plate, again following Newtonian dynamics, were derived independently by von Kármán (1921) and Prandtl (1927). Subsequently, studies by G. I. Taylor, Dryden, and their collaborators accounted for skin friction and boundary-layer separation with reasonable success.

The outstanding practical characteristic of laminar flow was immediately evident—this is, that the drag is only a fraction of that for turbulent flow (Fig. 1). There was great engineering interest in means to prevent the ever present tendency toward instability and abrupt transition to turbulent flow.

Theory showed that a falling pressure gradient was required to preserve laminar flow, and airfoils of arbitrary shape were designed to effect such a pressure distribution. The results were disappointing. Wind-tunnel tests showed transition to turbulent flow at a Reynolds Number far too low for extensive laminar flow on full-scale airplane wings. Furthermore, transition was sensitive to surface roughness, to any initial

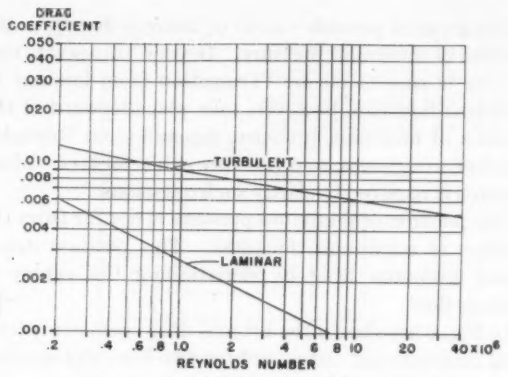

FIG. 1. Skin-friction drag of flat plates.

turbulence of the air stream, and even to acoustic vibration. Although hope of success was slight, substantial drag reduction could be obtained in no other way, since the profile drag of good wings at low incidence was attributable almost entirely to skin friction.

Not only were wind-tunnel tests disappointing in 1929–1930 but could be misleading as well. It was realized that all wind tunnels provided air streams of varying degrees of turbulence. An international exchange of models took place, and much progress was made in explaining the discrepancy between tests of the same model in different wind tunnels on the basis of their inherent turbulence.

This work probably stimulated the outstanding investigations of G. I. Taylor and B. M. Jones in England and Hugh Dryden and E. N. Jacobs in America on wind-tunnel turbulence and its control. To Dryden, in particular, we are indebted for hot-wire anemometer equipment of beautiful precision and for research that explained fully the effect of screens in reducing wind-tunnel turbulence.

Low-Turbulence Pressure Wind Tunnel

In 1938 a low-turbulence pressure wind tunnel was built at the Langley Laboratory to test two-dimensional airfoils at a Reynolds Number corresponding to full scale. This tunnel had an area contraction of 20 to 1 and a system of screens with the mesh and wire so selected that the wake from the screen did not contain vortices. Consequently, the screen itself did not introduce fine turbulence. In June, 1938, the first test of an airfoil designed to promote laminar flow indicated a drag coefficient of 0.0033 or about half of the lowest ever before recorded for an airfoil of comparable thickness. The turbulence measured was only a few hundredths of 1 per cent of the wind speed.

Jacobs, with Dryden's collaboration, was responsible for this wind tunnel and for what I believe to be a milestone in the progress of aerodynamics. The Langley research team now had a tool with which to untangle the confused state of our knowledge of viscous flow. They were greatly encouraged by B. M. Jones' Wright Brothers Lecture, also in 1938, in which he clearly showed from his experiments in flight that, by taking pains, laminar flow could be obtained for a considerable distance behind the leading edge of a smooth wing.

By May, 1941, the technique of airfoil design and testing at Langley had advanced to the point where low drags could be obtained for Reynolds Numbers corresponding to the flight of a medium bomber. However, the road was not easy and full success in the engineering sense could not have been attained by empirical methods alone. Guidance of a general theory was required.

DEVELOPMENT OF CLASSICAL HYDRODYNAMICS

I now leave the story of viscous flow and return to the parallel development of classical hydrodynamics, which also stems from Newton. Recall that modern airfoil theory was well established by 1930 on the basis of an ideal fluid with circulation. Mathematical methods were available to compute the pressure distribution on certain types of airfoils which, however, had unsatisfactory characteristics and were not used. For all practical purposes, airfoil theory in 1930 and practical airfoil design were unmarried.

Analysis of pressure-distribution measurements led Jacobs to separate the effects of camber and angle of attack on lift and to assume them to be independent. Theodoresen showed (N.A.C.A. Report No. 383, "On the Theory of Wing Sections with Particular Reference to the Lift Distribution") that such superposition was justified by the theory of thin airfoils as stated by Munk and Glauert. As a result of this theoretical support, a new family of N.A.C.A. airfoils was derived by Jacobs and Pinkerton in 1930. An arbitrary thickness distribution was used to form a series of symmetrical sections. These were given various types of camber to form families of cambered airfoils. The series proved highly successful and was widely used throughout the world. A number of variations of thickness distribution gave further airfoil forms. This work, based on airfoil theory but essentially empirical, provided the basis for most of the airfoil work, especially in Germany, Italy, and Japan up to and during the War.

The futility of efforts to obtain significant improvements by empirical variation of thickness distribution became apparent by 1935. What was wanted was stable laminar flow to a greater extent. To obtain this, complete control of pressure gradients was needed.

In 1931 Theodorsen (N.A.C.A. Report No. 411, "Theory of Wing Sections of Arbitrary shape") had published a theory of thick airfoils by means of which the pressure distribution for an arbitrary shape could be computed. The method used an inverse Joukowski transformation to transform an arbitrary airfoil to a nearly circular closed curve and, thence, to the corre-

ponding circle where the flow and pressures could be computed. Points on this curve are related to corresponding points on the circle by small angular and radial displacements. The pressure distribution as ordinarily computed from this theory was found to be not sufficiently precise near the leading edge for the prediction of local pressure gradients. Nevertheless, the theory was useful in showing how to obtain the favorable pressure drop over the forward portion of an airfoil and the sharp pressure recovery over the rear portion needed to prevent separation. Using approximate methods, airfoils of the N.A.C.A. families 2 to 5 were derived and tested. These families showed real advantages but are now considered obsolete.

Further experience with the Theodorsen transformation led Jacobs to the discovery that the airfoil, designed to give a desired pressure distribution, could be obtained with precision by an angular distortion of the curve into which the airfoil was transformed and then by correctiong both the airfoil and the corresponding pressure distribution by successive approximations. The method was systematized by Theodorsen and von Doenhoff in 1944 (N.A.C.A. No. L4G05, "Airfoil-Contour Modifications Based on ϵ Curve Method of Calculating Pressure Distribution") and reduced to engineering practice by Abbot, von Doenhoff and Stivers in 1945 in their comprehensive "*Summary of Airfoil Data*" (N.A.C.A. No. L5C05).

Engineering Applications

Now a word as to what has been done with this theory and the low-turbulence wind tunnel in the way of application. This brings us into the realm of engineering and the art of design for a useful purpose.

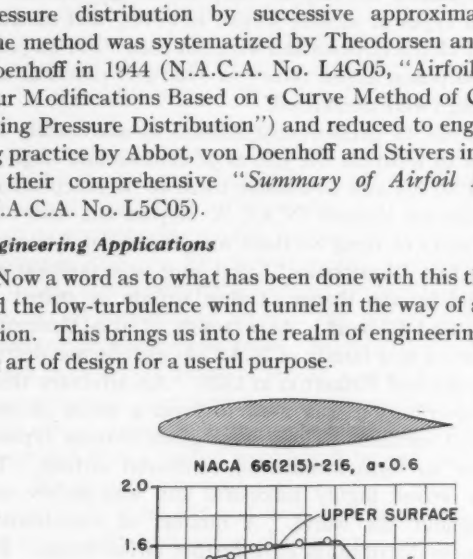

FIG. 2. Pressure distribution.

Fig. 2 shows the pressure distribution for a typical low-drag airfoil of the NACA 6 series as computed and as measured in the low-turbulence wind tunnel. Note the steadily falling pressure for the forward 60 per cent of the chord and the sharp pressure recovery after the position of minimum pressure.

The greatest possible extent of laminar flow is to the position of minimum pressure. Beyond this point, turbulence is sure to occur. Transition from laminar to turbulent flow can, however, take place forward of the position of minimum pressure, depending on Reynolds Number, roughness, and possibly other factors. More research is required to clarify such questions.

The position of minimum pressure is not far from the position of maximum thickness. This position determines minimum drag by determining the extent of laminar flow.

In Fig. 3 are shown the lift and drag coefficients for a good conventional airfoil and for two low-drag sections of the NACA 6 series, all of the same thickness. The curves are faired through points representing experimental determinations in the low-turbulence wind tunnel. The reduction in drag effected is of the order of 40 per cent. A method of computing such curves of lift and drag is presented in N.A.C.A. Report No. 4B05 ("A Concise Theoretical Method for Profile-Drag Calculation") and No. 4I12 ("The Theoretical Calculation of Airfoil Section Coefficients at Large Reynolds Numbers") together with a comparison with wind-tunnel tests. Excellent agreement is shown.

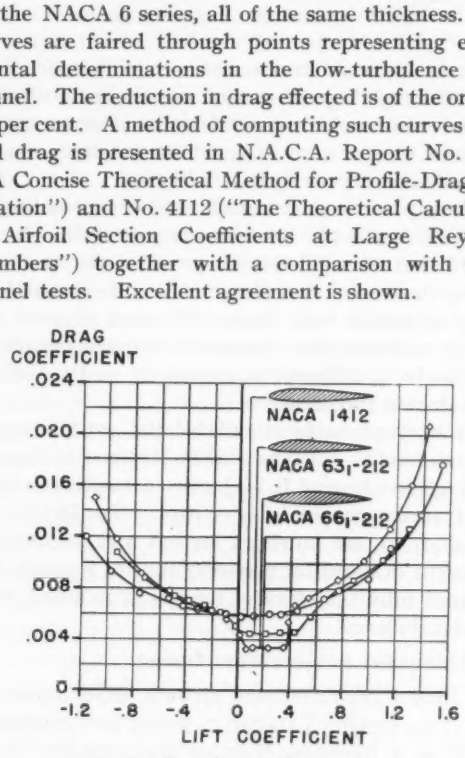

FIG. 3. Experimental drag polars.

The conventional airfoil shows a smooth variation of drag with increasing lift or angle of incidence. This is because the minimum pressure point moves slowly as the lift or angle changes. The sharp rise in drag for the NACA 6 series airfoils at two critical values of the lift is is caused by a sudden shift forward of the minimum pressure point and a consequent more forward transition.

This shift in the point of transition causes the characteristic "bucket" in the drag curve. It is, of course, the designer's wish to widen this bucket to ensure low drag for a useful range of flight conditions.

Fig. 4 illustrates the engineer's close control of the characteristics of design. Here are the pressure distributions for a series of airfoils designed to hold laminar flow for 30, 40, 50, or 60 per cent of the chord. The en-

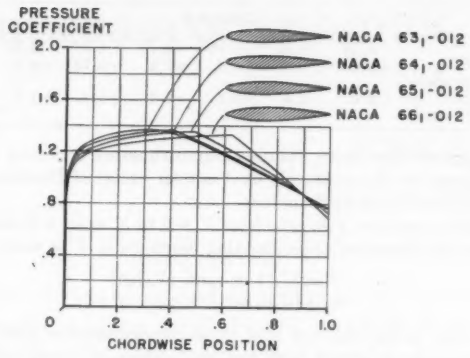

FIG. 4. Theoretical pressure distributions.

gineer may choose the one that best suits his operating conditions. He will recall that laminar flow is more difficult to maintain in proportion as the point of minimum pressure is farther back. He should be conservative if he has reason to fear his airplane wing may not remain smooth or may be required to operate under icing conditions in service.

The present position is that, for subsonic flight, the airplane designer now has a remarkably powerful theory to guide his judgment. However, the theory has been developed without regard to compressibility and therefore, does not apply at extremely high speeds. By a fortunate circumstance, the minimum pressure peak for these low-drag airfoils is lower than that for conventional airfoils, and, consequently, the critical flight speed at which sonic velocity is reached locally is somewhat higher. The great advantage of a combination of low drag with high critical speed was realized by the early NACA 16 series sections which are still used for propellers where good characteristics at high speed are imperative.

CONCLUSIONS

Let us pause to consider where we stand. Classical hydromechanics, still holding to its hypothesis of a frictionless fluid, predicts the normal pressures on the airfoil. The mechanics of a viscous fluid predicts the tangential forces on the airfoil. We assume, and the assumption is justified by experiment, that pressures due to the external flow are transmitted unchanged through the boundary layer. Thus, at last, we have the marriage of the two main branches of fluid mechanics which started with Newton's speculations on the nature of fluid resistance in his two imaginary fluids.

I should report for the record that the N.A.C.A. research that culminated after some 15 years of effort in this important advance was planned, guided, and inspired by Dr. George W. Lewis, Director of Aeronautical Research. His research teams included Jacobs, Theodorsen, Dryden, Abbott, Stack, and many others whose names will be found on N.A.C.A. reports since 1930.

While emphasizing this recent advance in fluid mechanics, I should be less than frank if I neglect to mention that there is a great deal more to learn. Specifically, the prediction of transition and separation of the boundary layer is not yet possible, and the entire transonic régime is a mystery. When the speed of flight equals the speed of sound, the flow is part subsonic and part supersonic. There is no adequate theory for such mixed flows. Furthermore, the wind tunnel, on which engineers have always depended for design data when theory would not serve, completely fails them at the speed of sound. Shock waves from the model are reflected back by the tunnel walls.

This surely is a challenging opportunity for research. Let us hope it will not take 300 years.

Letters to the Editor

Dear Sir:

The method of Ramberg and Osgood[1] of describing stress-strain curves by three parameters provides a convenient method of specifying the proportional limit of a material.

The importance of the proportional limit in compressive instability calculations has always been realized, but, because of the difficulty of precisely determining this property experimentally, it is usually neglected in specifying material properties.

The three-parameter method obviates experimental determination of the proportional limit, since the stress-strain curve is completely defined by an analytical expression, the constants of which are experimentally ascertained. If we accept the definition of proportional limit as the stress at which the strain has departed 0.01 per cent from that obtained from elasticity, it is a simple matter to derive an analytical expression for the proportional limit.

In the body of the paper,[1] the following expression for a stress-strain curve is given when $m_1 = 0.7$.

$$Ee/S_1 = \sigma + {}^3/_7\sigma^n \qquad (1)$$

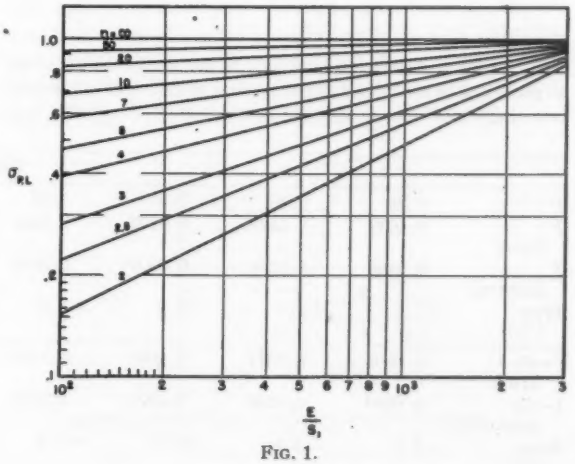

FIG. 1.

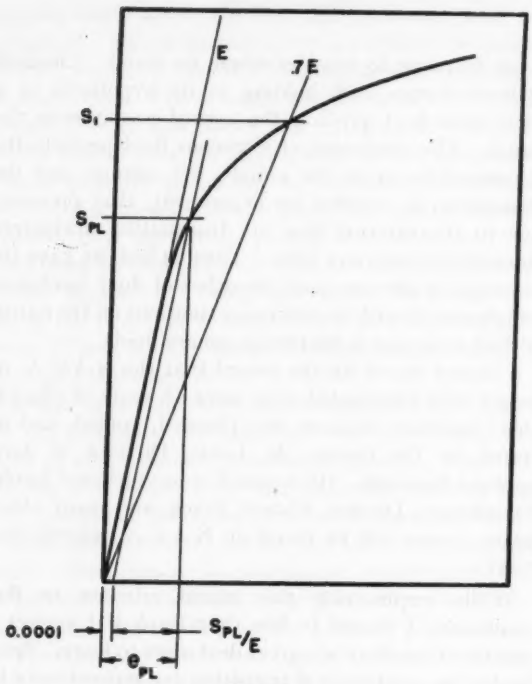

FIG. 2.

From Fig. 2, it can be seen that

$$e_{pl} = 0.0001 + (S_{pl}/E) \tag{2}$$

Combining Eqs. (1) and (2) and solving for the proportional limit stress ratio,

$$\sigma_{pl} = S_{pl}/S_1 = [2.33 \times 10^{-4}\,(E/S_1)]^{1/n} \tag{3}$$

This expression is depicted on Fig. 1, on which curves are drawn in terms of the three basic parameters.

REFERENCE

[1] Ramberg, W., and Osgood, W. R., *Description of Stress-Strain Curves by Three Parameters*, N.A.C.A. T.N. No. 902, July, 1943. Osgood, W. R., *Stress-Strain Formulas, Journal of the Aeronautical Sciences*, Vol. 13, No. 1, p. 45, January, 1946.

GEORGE GERARD
Principal Research Engineer
Republic Aviation Corporation

Dear Sir:

To facilitate flutter computations in the design stages of an airplane and to enable the flutter analyst to gain a better insight into the critical and noncritical parameters of the design it is suggested that finite, yet close, approximating functions be substituted for the commonly used tabular values of Theodorsen's F and G aerodynamic functions.

For a range of $V \equiv v/b\omega$ from $V = 0$ to $V = \infty$, it is suggested that the following approximating functions of V be used:

$$F \backsimeq {}^1/_2[1 + \tanh\,(V/10)]$$
$$G \backsimeq -V/8e^{-V/4}$$

It is to be observed that these approximations yield values rigorously in accord with the true values of F and G for the limiting conditions $V = 0$ and $V = \infty$.

For intermediate values of V, the closeness of approximation may be ascertained by a study of Table 1.

Despite the closeness of fit of the approximating functions, as seen in Table 1, they are, nevertheless, still too complicated to allow the flutter determinant to be solved explicitly for V. Therefore, the following further approximations are suggested:

$$F \backsimeq {}^1/_2(1 + V/10)$$
$$G \backsimeq -V/8(1 - V/4 + V^2/32)$$

For the range of significant V's encountered in the analysis of control surfaces of transport airplanes ($V = 0.25$ to $V = 2.50$), these latter approximations hold as closely as the former did over a wider range ($V = 0.25$ to $V = 5.00$). Closeness of fit may be judged from Table 2.

Even these errors are not so serious as one would at first suppose because of the manner in which F and G enter the total aerodynamic vector. For example, consider Theodorsen's $A_{b\beta} \equiv R_{b\beta} + iI_{b\beta}$. For it, the real and imaginary parts may be written as

$$R_{b\beta} = -B_{\beta 1} - Q(c)(2G)V + [B_{\beta 3} + Q'(c)(2F)]V^3$$
$$I_{b\beta} = [B_{\beta 2} + Q(c)(2F)]V + Q'(c)(2G)V^3$$

where all the symbols are Theodorsen's save for V and the functions of c, $Q(c)$ and $Q'(c)$. The Q functions are derived in the process of simplification of $R_{b\beta}$ and $I_{b\beta}$. All of the aerodynamic vectors may be written in exactly similar form.

For even rougher approximation and correspondingly greater simplification of the aerodynamic terms, $(2G)$ may be taken as zero and $(2F)$ as unity. The real parts then become quadratic and the imaginary parts become linear. This corresponds exactly with experience in plotting the aerodynamic terms using the true values of F and G and when the aerodynamic terms were plotted for a workable range of $V = 0$ to $V = 2.50$.

It is the hope of the writer to elaborate on the last paragraph above in an article at some future date.

W. RAYMOND GRIFFIN
Research Engineer

TABLE 2

V	0.25	0.50	1.00	1.25	1.67	2.00	2.50
F (% error)	+2.0	+2.5	+2.0	+1.5	+0.75	−0.5	+0.1
$(-G)$ (% error)	−3.9	−4.4	−2.7	−1.4	+1.4	+3.5	+7.5

TABLE 1

V	0.25	0.50	1.00	1.25	1.67	2.00	2.50	3.33	5.00
F (true)	0.5037	0.5129	0.5395	0.5541	0.5788	0.6030	0.6245	0.6650	0.7276
F (approx.)	0.5120	0.5250	0.5500	0.5625	0.5835	0.6000	0.6250	0.6592	0.7310
Error (%)	+1.5	+2.5	+2.0	+1.5	+1.0	−0.5	0 (approx.)	−1.0	+0.5
$(-G)$ (true)	0.0305	0.0577	0.1003	0.1165	0.1378	0.1510	0.1660	0.1800	0.1886
$(-G)$ (approx.)	0.0293	0.0552	0.0974	0.1144	0.1374	0.1516	0.1672	0.1810	0 1790
Error (%)	−4.0	−4.4	−3.0	−1.8	−0.3	+0.5	+0.9	+0.5	−5.1

Superaerodynamics, Mechanics of Rarefied Gases

HSUE-SHEN TSIEN*

California Institute of Technology

Introduction

Zahm[1] in 1934 published an article on the aerodynamics of highly rarefied gases, a branch of fluid mechanics which he called superaerodynamics. At that time, however, with the means of propulsion then available, flight at extreme altitudes did not seem to be realizable. Therefore, superaerodynamics has been considered as a subject of academic interest rather than one of practical engineering importance. With the recent perfection of the rocket as a propulsive power plant, the situation is radically changed and there should be no limit to the altitude that can be reached by an aircraft. There are even indications that the optimum flight altitude of long-range rocket airplanes is approximately 60 miles. At these and higher altitudes, the air density is so low that the fluid must be thought of as one having a coarse structure and not as a continuous medium of conventional fluid mechanics. Then concepts of superaerodynamics are needed to guide the design of such an aircraft.

Besides its applications to high-altitude flights, superaerodynamics should have many applications to industrial processes in which low density gases are involved. The knowledge of superaerodynamics should be of invaluable help in improving the efficiency of these processes. For instance, the pumping of low density gases will be of more and more importance because of the increasingly frequent use of high vacuum in distillation and other chemical engineering processes. The improvement in the design of such gas pumps definitely needs the understanding of the principles of mechanics of low density gases. It is the purpose of the present paper to discuss the fundamental concepts of this new branch of fluid mechanics and to indicate some of the results already obtained. The field of superaerodynamics is still relatively uncultivated. Here and there the ground has been broken by a few physicists. However, further effort is required to develop this branch of fluid mechanics into an aid in engineering design and research.

Mean Free Path and Realms of Fluid Mechanics

As a first approximation, the gas may be considered as an aggregate of rapidly moving particles which are constantly colliding with each other. The influence of the particles on each other can be conveniently neglected until they are so close together that a "collision" takes place. Then the coarseness of the structure of the gaseous medium can be expressed by the parameter l which is the distance the particles or molecules travel between collisions. Since the instantaneous velocity distribution and density distribution in the gas are far from uniform, one can only conveniently use the statistical average of a quantity instead of the instantaneous value of the quantity. The distance l is then the statistical average over the billions and billions of molecules concerned. This average l is called the mean free path of the gas. If the mean free path is small in comparison with the dimension of the flow field or the dimension of the body in the flow field, then the gas can be considered as a continuum and the ordinary gas dynamics is sufficient for the analysis of these flows. If the mean free path is not negligible when compared with the dimension of the body, then the effects of the discrete character of the gas must be taken into account in the calculation. Then if L is the linear dimension of the body, superaerodynamics can be defined as the aerodynamics of flows where the ratio l/L is not negligible.

The free mean path l can be calculated from the mean velocity of the molecules, the density of the gas, and the "effective radius of the molecules." However, there is no direct way of measuring the effective radius of the molecules; therefore, it is more fruitful to express the quantity l in terms of a measurable quantity such as the viscosity of the gas. This is easily done by the following consideration. If the gas flows in the x-direction with the macroscopic velocity $u(y)$ (Fig. 1), the gradient of velocity is then $\partial u/\partial y$. Now the gas molecules in a lower layer move into an upper layer with the average velocity $\bar{v}$ of the molecules. The distance

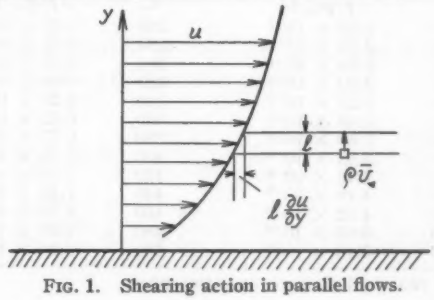

Fig. 1. Shearing action in parallel flows.

Received May 20, 1946.

* Associate Professor of Aeronautics, Daniel Guggenheim Aeronautical Laboratory. Now Associate Professor of Aeronautical Engineering, Massachusetts Institute of Technology.

they will travel before they lose their identity by collision with other molecules is l. The difference in macroscopic velocity of the layer where the molecules originated and the layer where the molecules are mixed is then $l(\partial u/\partial y)$. The mass of molecules crossing a unit area of the layer proportional to $\rho\bar{v}$ where ρ is the density of the fluid. Therefore, momentum exchange between layers is proportional to $\rho\bar{v}l(\partial u/\partial y)$. This is the viscous shearing stress. Since the coefficient of viscosity is defined as

$$\tau = \mu(\partial u/\partial y)$$

μ is proportional to $\rho\bar{v}l$. The proportionality constant can be calculated by the kinetic theory. The most accurate calculation is that due to Chapman[2] who gives

$$\mu = 0.499\rho\bar{v}l \tag{1}$$

The average velocity $\bar{v}$ is closely connected with the "velocity of sound" a by the equation

$$\bar{v} = \sqrt{\frac{8}{\pi}}\sqrt{\frac{p}{\rho}} = \sqrt{\frac{8}{\pi\gamma}}\,a \tag{2}$$

where γ is the ratio of specific heats. From Eqs. (1) and (2), the mean free path is given in terms of the kinematic viscosity $\nu = \mu/\rho$ and the velocity of sound a by

$$l = 1.255\sqrt{\gamma}(\nu/a) \tag{3}$$

For air, the quantity $l(p/p_0)$ in inches is tabulated in Table 1, where p and p_0 are the pressure and standard pressure (one atmosphere), respectively. Thus, for ordinary pressures, the mean free path is truly negligible in comparison with the body dimensions, and therefore gas dynamics is sufficient for aerodynamic calculations. However, at extremely high altitudes where the pressure may be only one-millionth of the pressure at the surface of the earth, the mean free path will be comparable to the body dimensions. A clear demonstration of this fact is perhaps that of Fig. 2 where the mean free path calculated by Maris[3] is plotted against the altitude. Maris assumed that the air temperature above 80 km.

TABLE 1
Mean Free Path for Air

Temperature, °C.	$l(p/p_0)$, In.	Temperature, °C.	$l(p/p_0)$, In.
0	2.32×10^{-6}	260	5.33×10^{-6}
20	2.55×10^{-6}	280	5.57×10^{-6}
40	2.78×10^{-6}	300	5.85×10^{-6}
60	3.00×10^{-6}	320	6.05×10^{-6}
80	3.23×10^{-6}	340	6.28×10^{-6}
100	3.46×10^{-6}	360	6.52×10^{-6}
120	3.69×10^{-6}	380	6.77×10^{-6}
140	3.92×10^{-6}	400	7.00×10^{-6}
160	4.16×10^{-6}	420	7.24×10^{-6}
180	4.40×10^{-6}	440	7.49×10^{-6}
200	4.62×10^{-6}	460	7.73×10^{-6}
220	4.85×10^{-6}	480	7.96×10^{-6}
240	5.10×10^{-6}	500	8.20×10^{-6}

p_0 = Standard pressure, one atmosphere.

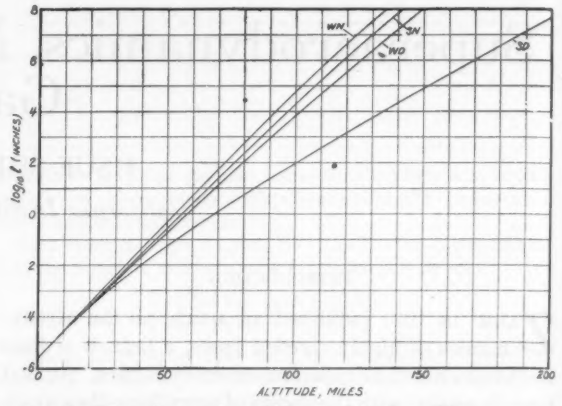

FIG. 2. Mean free path at different altitudes; SD = summer day, SN = summer night, WD = winter day, and WN = winter night (H. B. Maris).

(50 miles) is constant and has the value 97°C., −43°C., −23°C., and −53°C. for summer day, summer night, winter day, and winter night, respectively. At 50 miles altitude, the mean free path is seen to be nearly 1 in. The air there is certainly not a continuum.

The flow conditions near the wall for the case in which the mean free path l is small but not negligible compared with the body dimension L or the thickness δ of the boundary layer were first investigated theoretically by J. C. Maxwell in 1879. It was found that the gas no longer sticks to the surface but slips over the surface with a definite velocity. This phenomenon was also suggested by the experiments of Kundt and Warburg in 1875, on the damping of a vibrating disc by gas at low pressure. Later experiments and theoretical study completely verified this conclusion. This type of flow can be called the *slip flow*. Because of Eq. (3),

$$\frac{l}{\delta} = \frac{l}{L}\frac{L}{\delta} \sim \frac{L}{\delta}\frac{\nu}{a}\frac{1}{L} \sim \frac{L}{\delta}\frac{M}{Re} \tag{4}$$

where M is the Mach Number of the free stream and Re is the Reynolds Number of the flow referred to the length L of the body. For extremely small Reynolds Number, $L/\delta \sim 1$, then

$$l/\delta \sim M/Re, \quad Re \ll 1 \tag{5}$$

For large Reynolds Number, it is well known that $L/\delta \sim \sqrt{Re}$. Then,

$$l/\delta \sim M/\sqrt{Re}, \quad Re \gg 1 \tag{6}$$

Therefore, if the interval $1/100 < l/\delta < 1$ is considered as the proper range for the slip flow, then in the plane of M and Re, this realm of fluid mechanics occupies a region as shown in Fig. 3. The region below this slip-flow region belongs to the realm of the conventional gas dynamics with the usual boundary conditions at the wall.

If the mean free path is much larger compared with the body dimensions, one enters an entirely new realm

of fluid mechanics. Here the chances for the collision of molecules among themselves are much smaller than the chances for the collision of molecules with the wall or the surface of the body. Therefore, for the calculation of forces, one need only consider the impact of a stream of molecules with a velocity and energy distribution determined by the thermal equilibrium in the free stream, the Maxwellian distribution. The re-emission of the molecules from the surface will be governed by the accommodation coefficient. But the greatest simplification comes from the fact that one need not consider the distortion of the Maxwellian distribution due to the collision of the re-emitted molecules with the molecules in the stream. The realm of fluid mechanics can thus be called the *free molecule flow*.

If one takes the limiting ratio of l/L to be 10 for the free molecule flow, then this realm of fluid mechanics occupies a region of the M-Re plan given by

$$l/L \sim M/Re > 10$$

This is shown in Fig. 3. The region between the free molecule flow and the slip flow is the realm of fluid mechanics where the collision between molecules and the collision of molecules with the wall are of equal importance. The problem is extremely complicated and no satisfactory theoretical solution can yet be offered. However, it is certain that as far as the fluid itself is concerned, the characteristic parameters are still the Mach Number M and the Reynolds Number Re as used in gas dynamics.

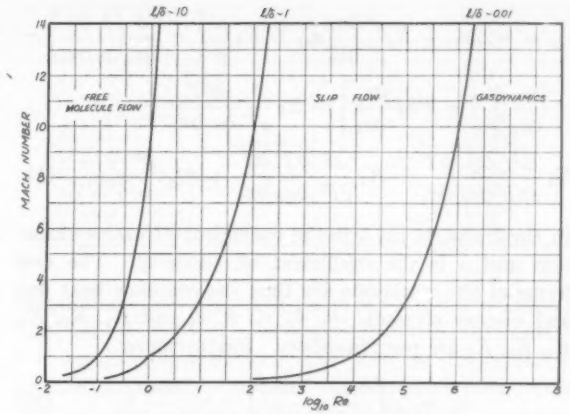

FIG. 3. Realms of fluid mechanics.

STRESSES AND BOUNDARY CONDITIONS IN SLIP FLOW

The fundamental equations governing the fluid flows are the continuity equation, the dynamic equations, and the energy equation. If u_1, u_2, u_3 are the components of velocity in the x_1, x_2, x_3 directions, and p, ρ, T the pressure, density, and temperature of the gas, respectively, these equations are*

$$(\partial\rho/\partial t) + (\partial\rho u_i/\partial x_i) = 0 \tag{7}$$

$$\rho\frac{\partial u_i}{\partial t} + \rho u_j\frac{\partial u_i}{\partial x_j} = -\frac{\partial p}{\partial x_i} - \frac{\partial \tau_{ij}}{\partial x_j} \tag{8}$$

$$\left(\rho\frac{\partial}{\partial t} + \rho u_i\frac{\partial}{\partial x_i}\right)\left(\frac{u_i u_i}{2} + c_p T\right) = \frac{\partial p}{\partial t} - \frac{\partial q_i}{\partial x_i} - \frac{\partial}{\partial x_i}(\tau_{ij}u_j) \tag{9}$$

In these equations, the τ's are the components of the stress tensor, the q's are the components of the heat flux vector, and c_p is the specific heat at constant pressure.

* The summation convention is used here. For instance,

$$\frac{\partial u_K}{\partial x_k} = \frac{\partial u_1}{\partial x_1} + \frac{\partial u_2}{\partial x_2} + \frac{\partial u_3}{\partial x_3}$$

For gases under ordinary pressures, the stresses are the products of the coefficient of viscosity and linear combinations of the first order derivatives of the velocity components. The components of heat flux are simply the products of coefficient of heat conduction and the components of the gradient of temperature.

These relations between the stresses and the heat flux with the flow quantities are confirmed by the kinetic theory of nonuniform gases developed by Maxwell, Boltzmann, Chapman, D. Enskog, and others. In this theory, the distribution function of the molecules in the velocity space on the probability of molecules having a particular range of velocities plays the predominating role.

If, in the macroscopic sense, the gas is at rest with uniform temperature, the probability function is the well-known Maxwellian distribution. In a nonuniform gas, the first order correction to this Maxwellian distribution gives the ordinary viscous stresses and the heat flux by conduction, as observed by experiments.

However, the theory also gives a second order correction to the Maxwellian distribution which introduces highly complicated additional terms to the stresses and the heat flux. These additional terms, while negligible for gases under ordinary pressure, are important for rarefied gases. In fact, they form the basis for interpretation of many experimentally observed phenomena, such as the operation of a radiometer.

The investigation of Burnett[4] gives the following forms of the heat flux and the stresses:

$$q_i = -\lambda\frac{\partial T}{\partial x_i} + \theta_1\frac{\mu^2}{\rho T}\frac{\partial u_j}{\partial x_j}\frac{\partial T}{\partial x_i} + \theta_2\frac{\mu^2}{\rho T}\left[\frac{2}{3}\frac{\partial}{\partial x_i}\left(T\frac{\partial u_j}{\partial x_j}\right) + 2\frac{\partial u_j}{\partial x_i}\frac{\partial T}{\partial x_j}\right] + \left(\theta_3\frac{\mu^2}{\rho p}\frac{\partial p}{\partial x_j} + \theta_4\frac{\mu^2}{\rho}\frac{\partial}{\partial x_j} + \theta_5\frac{\mu^2}{\rho T}\frac{\partial T}{\partial x_j}\right)e_{ji} \tag{10}$$

$$\tau_{ij} = -2\mu e_{ij} + K_1\frac{\mu^2}{p}\frac{\partial u_k}{\partial x_k}e_{ij} + K_2\frac{\mu^2}{p}\left[-\overline{\frac{\partial}{\partial x_i}\left(\frac{1}{\rho}\frac{\partial p}{\partial x_j}\right)} - \frac{\partial u_k}{\partial x_i}\frac{\partial u_j}{\partial x_k} - 2\,\overline{e_{ik}\frac{\partial u_j}{\partial x_k}}\right] + K_3\frac{\mu^2}{\rho T}\overline{\frac{\partial^2 T}{\partial x_i \partial x_j}} + K_4\frac{\mu^2}{\rho p T}\overline{\frac{\partial p}{\partial x_i}\frac{\partial T}{\partial x_j}} + K_5\frac{\mu^2}{\rho T^2}\overline{\frac{\partial T}{\partial x_i}\frac{\partial T}{\partial x_j}} + K_6\frac{\mu^2}{p}\overline{e_{ik}e_{kj}} \quad (11)$$

In these equations, λ is the coefficient of heat conduction and μ is the coefficient of viscosity. The first terms of the equations are thus the ordinary heat flux and viscous stresses. θ_1, θ_2, θ_3, θ_4, θ_5 and K_1, K_2, K_3, K_4, K_5, K_6 are pure numbers. Furthermore,

$$e_{ij} = \tfrac{1}{2}\left(\frac{\partial u_i}{\partial x_j} + \frac{\partial u_j}{\partial x_i}\right) - \tfrac{1}{3}\frac{\partial u_k}{\partial x_k}\delta_{ij} \quad (12)$$

where $\delta_{ij} = 1$ if $i = j$ and $\delta_{ij} = 0$ if $i \neq j$. Any tensor A_{ij} with a bar over it has the following meaning:

$$\overline{A_{ij}} = \tfrac{1}{2}(A_{ij} + A_{ji}) - \tfrac{1}{3}A_{kk}\delta_{ij} \quad (13)$$

The approximate values for θ's and K's are

$$\theta_1 = \frac{15}{4}\left(\frac{7}{2} - \frac{T}{\mu}\frac{d\mu}{dT}\right),$$

$$\theta_2 = \frac{45}{8},\ \theta_3 = -3,\ \theta_4 = 3,\ \theta_5 = \frac{3}{2}\left(5 - \frac{T}{\mu}\frac{d\mu}{dT}\right) \quad (14)$$

$$K_1 = \frac{4}{3}\left(\frac{7}{2} - \frac{T}{\mu}\frac{d\mu}{dT}\right),$$

$$K_2 = 2,\ K_3 = 3,\ K_4 = 0,\ K_5 = \frac{3T}{\mu}\frac{d\mu}{dT},\ K_6 = 8 \quad (15)$$

More accurate values for K's are given by Burnett[4] for molecules of rigid elastic spheres. They differ little from those of Eq. (15).

It is immediately clear by examining Eqs. (10) and (11) that the additional terms in the heat flux and the stress tensor are only of importance in rarefied gases. As an example, the magnitude of the ratio of the second terms to the first terms of these equations will be estimated presently. Let U be the free stream velocity and T_0 the free stream density and temperature, c_p the specific heat at constant pressure. For gases, the Prandtl number $c_p\mu/\lambda$ is rarely unity. Then these ratios have the same order of magnitude given by

$$\frac{U}{L}\frac{\mu}{\rho_0 c_p T_0} = \frac{\mu}{\rho_0 U L}\frac{U^2}{c_p T_0} = (\gamma - 1)\frac{M^2}{Re}$$

where M is the free stream Mach Number and Re the Reynolds Number. According to Eq. (4), the order of magnitude of the additional heat flux or stresses to the ordinary heat flux and stresses is then $M(l/L)$. That is, the additional terms are only of importance if the product of Mach Number and the ratio of mean free path to body dimension is large. Therefore, for the gas dynamical flows with small mean free path, the ordinary heat conduction terms and viscous stress terms suffice. This is also true for the slip flows if the Mach Number is small. For slip flows at high Mach Number, the conventional Navier-Stokes equations are no longer a true description of the physical relations and the complicated forms of heat flux q_i and the stresses τ_{ij} given by Eqs. (10) and (11) must be used.

Since the additional terms in q_i and τ_{ij} contain higher derivatives than the first order, they will raise the order of the system of partial differential equations given by Eqs. (7), (8), and (9). Hence, to solve these equations, one needs more boundary conditions than in the case of gas dynamics. In fact, the question of proper boundary conditions for slip flows of large Mach Number where such additional terms are required, has not yet been answered. This is then one of the fundamental problems in superaerodynamics. The theoretical study of the boundary conditions must, of course, be based on the kinetic point of view. Parallel to such theoretical investigation, it seems advisable to obtain also an experimental check on the validity of Eqs. (10) and (11). One of the possible experiments would be to observe the flow of rarefied gas between two concentric cylinders, one rotating and the other held fixed. If the length of the cylinders is large in comparison with the gap between the cylinders, the flow will be two-dimensional with the radial distance as the only parameter. The physical situation is thus the simplest, and amenable to detailed examination. Indeed, the same experiment has been performed by Millikan and his collaborators[5] at low rotative speeds for the same type of investigation. The high rotative speeds necessary to obtain high flow velocities will certainly introduce difficulties in the technique but these do not seem to be insurmountable.

The results of the kinetic theory discussed in the previous paragraphs are based upon the assumption of simple molecules with the only intrinsic energy due to translation. Generally, however, the gas molecules have three kinds of intrinsic energies: the translational energy, the rotational energy, and the vibrational energy. When the gas is in equilibrium, the distribution of the total energy among the three forms is uniquely determined by the properties of the gas molecules concerned. If this equilibrium is destroyed by a sudden change in the external conditions, such as an expansion, new equilibrium will be reached by numerous collisions of the molecules under these new conditions. However, it is known through ultrasonic dispersion, etc., that the process of reaching equilibrium in the vibrational energy is a slow one. In other words, a large number of collisions is necessary to excite the vibration degrees of freedom of the molecules properly. Since the average velocity of the molecules is $\bar{v}$, the average distance traveled by the molecules per unit time is $\bar{v}$ 1. The number of collisions made by the molecules per unit time is then $\bar{v}/l$. Therefore, the time t, generally called the relaxation time, necessary to excite the vibrational energy is proportional to the mean free path at a given temperature. In other words, the relaxation time is inversely proportional to the pressure of the gas. The

TABLE 2
Relaxation Time t for the Excitation of Vibrational Energy at One Atmosphere (Reference 6)

Pure CO_2		O_2	
Temperature, °C.	$t \times 10^6$ sec.	Temperature, °C.	$t \times 10^6$ sec.
19.2	10.8	40.7	4.4
47.1	10.6	49.7	2.9
58.1	8.1	77.9	4.0
88.7	7.9	100.2	3.6
		138.0	3.1
		140.6	3.7
		141.4	3.3

measured value of t for several typical gases is given in Table 2 (reference 6). Therefore, at extremely low pressures, the relaxation time may be of the order of 1 sec. If this is coupled with high flow velocity, the gas must have passed the body before the vibrational degrees of freedom are excited. Therefore, in low density gas flows, the vibrational energy of the gas can be considered as fixed at the "free stream" value. This decrease in the effective number of degrees of freedom of the gas molecules tends to raise the value of γ, the ratio of specific heats. It is fortunate that for air at ordinary temperatures, the equilibrium vibrational energy is small, therefore this freezing of vibrational degrees will not greatly alter the value of γ. However, at higher temperatures and for other polyatomic gases, the effect may be appreciable.

BOUNDARY CONDITIONS FOR SLIP FLOWS OF SMALL MACH NUMBER

As concluded in the preceding section, the slip flows of small Mach Number can be calculated by using the Navier-Stokes equations. The proper boundary conditions for such flows were first investigated by Maxwell. Millikan[5] has reduced Maxwell's consideration to a simple form. A more detailed theoretical treatment of the problem by Boltzmann's H-theorem was given by Epstein.[7] The result of these investigations shows that if the Mach Number of the flow is small, then the flow velocity along the wall, the normal gradient $\partial u/\partial y$ of u, and the temperature gradient $\partial T/\partial x$ along the wall are connected by the relation[8]

$$u = \frac{\mu}{\beta}\frac{\partial u}{\partial y} + \frac{3}{4}\frac{\mu}{\rho T}\frac{\partial T}{\partial x} \qquad (16)$$

at $y = 0$, where β is the coefficient of sliding or external friction and μ the coefficient of viscosity. The second term in Eq. (16) is the velocity due to temperature gradient and is called the creep velocity. The ratio of μ and β is given by

$$\mu/\beta = 0.998\,[(2/f) - 1]l \qquad (17)$$

f is the fraction of the tangential momentum of the impinging molecules transmitted to the wall. Maxwell himself interpreted the fractional value of f as meaning that a fraction f of the surface reflects diffusely and the remainder specularly. The value of f is listed in Table 3 as given by Millikan.[5] It is seen from Eq. (17) that if l is small compared with the scale of the velocity gradient or the thickness δ of the boundary layer, then β is large and u at the wall is small. This is the reason why in gas dynamics one generally imposes the boundary condition $u = 0$ at the wall. If l/δ is not negligible, then there is a slip of the gas at the wall.

TABLE 3
Values of f (Reference 5)

	f
Air or CO_2 on machined brass or old shellac	1.00
Air on mercury	1.00
Air on oil	0.895
CO_2 on oil	0.92
Hydrogen on oil	0.925
Air on glass	0.89
Helium on oil	0.874
Air on fresh shellac	0.79

Table 3 shows that the value of f is very nearly unity. Therefore, the molecules, after striking the surface, have a strong tendency to reflect diffusely. In the scale of molecular dimensions, the surface of a solid body must be extremely jagged even if it is highly polished in the macroscopic sense. Then one cannot expect the molecules to reflect in any uniform direction. The tendency toward diffusive reflection is thus, perhaps, anticipated. Furthermore, a closer study of the behavior of the molecules colliding with the solid surface seems to indicate the temporary adsorption of the molecules on the surface. This combined structure of gas molecule and the surface materials then breaks up with a certain average rate determined by the "lifetime" of the combined structure. The molecules thus freed are re-emitted from the surface. With this procedure, the molecules re-emerge from the surface with all their prior history obliterated. In particular, the direction of re-emission is completely dependent upon the direction of impinging. In other words, the molecules re-emit diffusely.

Similar to this velocity discontinuity, there is a temperature discontinuity at the wall first found by Smoluchowski in 1898. Namely,

$$\kappa\,(T - T_w) = \lambda(\partial T/\partial y), \quad y = 0 \qquad (18)$$

where T is the temperature of the gas, T_w is the temperature of the wall, and κ is the coefficient of temperature discontinuity. This coefficient κ can be expressed in terms of the mean free path by a consideration similar to Maxwell's.[9] The result is

$$\frac{1}{\kappa} = 1.996\left(\frac{2-\alpha}{\alpha}\right)\frac{\gamma}{\gamma+1}\frac{1}{\mu C_p}l \qquad (19)$$

where α is the accommodation coefficient introduced by Knudsen.[10] α can be defined as the fractional extent to which those molecules that fall on the surface and are reflected or re-emitted from it, have their mean energy adjusted or "accommodated" toward what it

would be if the returning molecules were issuing as a stream out of the mass of gas at the temperature of the wall. This adaptation of the impinging molecules to the wall conditions is, of course, expected from the temporary adsorption of molecules on the surface, as mentioned before. Thus, if E_i is the energy brought up to unit area of the wall per second by the incident molecules, and E_r the energy carried away by the re-emitted molecules, and E_w the energy that would be carried away if the gas is at the wall temperature, then

$$E_i - E_r = \alpha(E_i - E_w) \tag{20}$$

Of course, strictly speaking, α is different for the three different types of molecular energies: translational, rotational, and vibrational. However, experimental evidence seems to indicate that one coefficient is generally sufficient. The older measured values of α are given in many books on kinetic theory of gases.[11] Wiedmann[12] recently determined the value of α for air on metals. The results are given in Table 4. Wiedmann concluded that the value of the accommodation coefficient is independent of the nature of the technical surface of the metal. This again supports the concept of the microscopic character of the surface collision.

TABLE 4
Accommodation Coefficient α for Air (Reference 12)

Surface Description	Accommodation Coefficient—Minimum	Accommodation Coefficient—Maximum
Flat black lacquer on bronze	0.881	0.894
Bronze, polished	0.91	0.94
Bronze, machined	0.89	0.93
Bronze, etched	0.93	0.95
Cast iron, polished	0.87	0.93
Cast iron, machined	0.87	0.88
Cast iron, etched	0.89	0.96
Aluminum, polished	0.87	0.95
Aluminum, machined	0.95	0.97
Aluminum, etched	(0.89)	(0.97)

Slip Flows at Small Mach Numbers

If the Mach Number is extremely small, the effect of the compressibility of the gas can be neglected and the fluid can be treated as incompressible. In order that the mean free path will be comparable with body dimension, the Reynolds Number must also be small. The flow can then be calculated by the well-known method of Stokes[13] who neglected the inertia terms, which are small in comparison with the viscous and pressure terms. The resistance of a sphere of radius R moving with a velocity U through a fluid of viscosity and coefficient β of sliding friction is given by Basset.[14] If the drag coefficient C_D is defined as the drag divided by $(\rho/2)U^2\pi R^2$ then

$$C_D = \frac{12}{Re}\left[\frac{1 + 2(\mu/\beta R)}{1 + 3(\mu/\beta R)}\right] \tag{21}$$

where Re is the Reynolds Number UR/ν. According to Eqs. (3) and (17),

$$\frac{\mu}{\beta R} = 0.998\left(\frac{2}{f} - 1\right)\frac{l}{R} = 1.253\sqrt{\gamma}\left(\frac{2}{f} - 1\right)\frac{M}{Re} \tag{22}$$

Hence, Eq. (21) can be rewritten as

$$C_D = \frac{12}{Re}\left\{\frac{1 + 2.506\sqrt{\gamma}\,[(2/f) - 1](M/Re)}{1 + 3.759\sqrt{\gamma}\,[(2/f) - 1](M/Re)}\right\} \quad \text{(sphere)} \tag{23}$$

Fig. 4 shows the drag coefficient as function of M and Re with $\gamma = 1.405$ and $f = 1$. It is seen that there is an appreciable reduction in the drag coefficient due to the slip phenomenon. It also introduces a large effect of Mach Number, although this is not the compressibility effect in the ordinary sense.

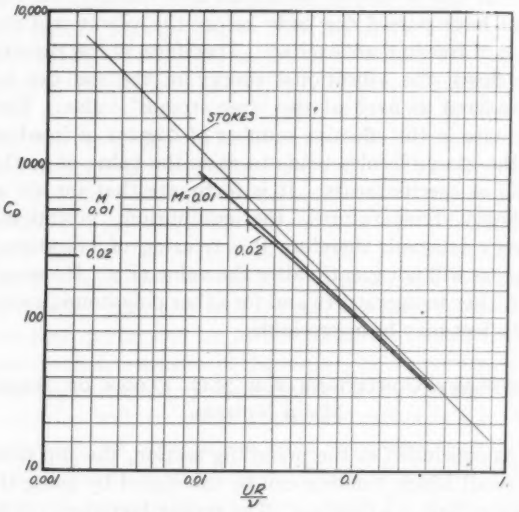

FIG. 4. Drag coefficient C_D as functions of Mach Number M and Reynolds Number for spheres of radius R, $f = 1$, $\gamma = 1.405$.

The similar case of the uniform two-dimensional motion of a circular cylinder can be obtained by a slight modification of Lamb's solution.[15] If the drag coefficient is defined as the drag per unit length divided by $(\rho/2)U^2(2R)$ where R is the radius of the cylinder,

$$C_D = 4\pi/Re\left[\log\frac{4}{Re} - 1.28107 + 1.253\sqrt{\gamma}\left(\frac{2}{f} - 1\right)\frac{M}{Re}\right] \quad \text{(cylinder)} \tag{24}$$

where Re is again the Reynolds Number UR/γ. The results of calculation are again plotted in terms of M and Re in Fig. 5. The reduction of drag due to slip is again evident.

For the fully established laminar flow through a circular tube of radius R, the velocity u as a function of the radial distance from the axis of the tube is determined by

$$\frac{1}{\mu}\frac{dp}{dx} = \frac{1}{r}\frac{d}{dr}\left(r\frac{du}{dr}\right) \tag{25}$$

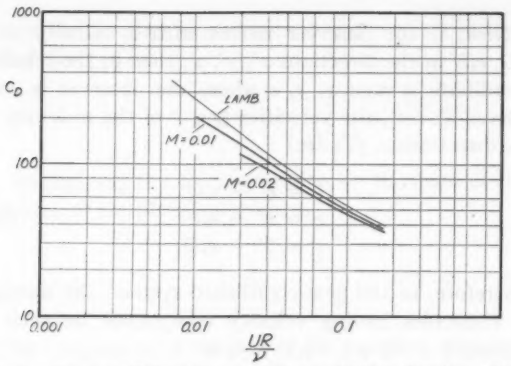

FIG. 5. Drag coefficient C_D as functions of Mach Number M and Reynolds Number for cylinders of radius R, $f = 1$, $\gamma = 1.405$.

The pressure gradient along the tube is a constant. Therefore, Eq. (25) yields

$$du/dr = (1/2\mu)(dp/dx)r \tag{26}$$

and

$$u = (1/4\mu)(dp/dx)r^2 + u_0 \tag{27}$$

where u_0 is the velocity at the center of the tube. The boundary condition that

$$\beta u_{r=R} = -\mu(du/dr)_{r=R}$$

then gives

$$-dp/dx = (4\mu/R^2)/[1 + 2(\mu/\beta R)]u_0 \tag{28}$$

The relation between the average velocity U and the maximum velocity u_0 can be easily obtained by integrating Eq. (27). Thus

$$u_0 = U\{[1 + 2(\mu/\beta R)]/[1/2 + 2(\mu/\beta R)]\} \tag{29}$$

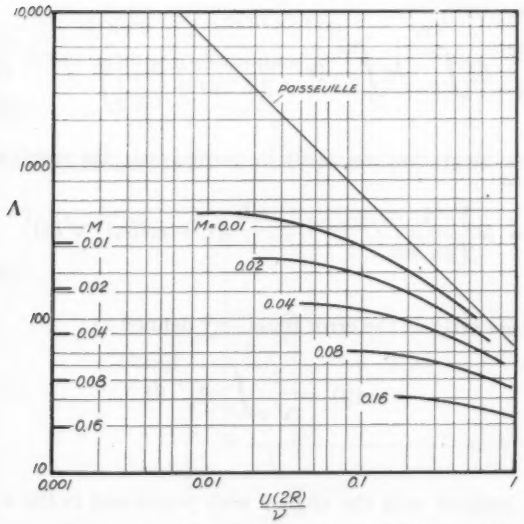

FIG. 6. Pressure drop coefficient Λ as functions of Mach Number M and Reynolds Number Re for flow in a tube of radius R, $f = 1$, $\gamma = 1.405$.

As the ratio of mean free path to the radius increases, the value of $\mu/\beta R$ will increase according to Eq. (22). Then Eq. (29) shows that the average velocity U approaches the maximum velocity u_0. In other words, the velocity distribution across the tube becomes more uniform. This is, of course, expected from the "slip" at the wall.

If the pressure drop coefficient Λ is defined as

$$\Lambda = (4R/\rho U^2)(-dp/dx) \tag{30}$$

then Eqs. (19) and (20) give immediately

$$\Lambda = \frac{64}{Re}\frac{1}{1 + 10.024\sqrt{\gamma}\,[(2/f) - 1](M/Re)} \tag{31}$$

where Re is the Reynolds Number based upon the diameter, $U(2R)/\nu$. Here again the effect of slip is to reduce the resistance coefficient. For extremely small mean free path the value of the second fraction is unity and the equation reduces to the well-known formula for Poiseuille flow. Fig. 6 is a graph for Λ as function of M and Re, assuming as before $f = 1$ and $\gamma = 1.405$. Experiments on the slip flow in a tube were made by Knudsen,[16, 17] Gaede,[18] and Ebert.[19, 20] The correctness of Eq. (31) is fully verified. In fact, it can be used to determine the reflection factor f for the wall materials.

Free Molecule Flows at Small Mach Numbers

Free molecule flow at low velocities has been studied for two cases: the flow around a sphere, and the flow in a tube. The calculation made by Epstein[7] has shown that the drag coefficient C_D can be expressed

$$C_D = 8/3\sqrt{8/\pi\gamma}\; C(1/M) \tag{32}$$

where C is a constant. Epstein determined C with diffuse reflection of molecules to be 1.442 for spheres that do not conduct heat and 1.393 for spheres that conduct heat perfectly. The experimental value of C for charged oil drop through air found by Millikan[21] is 1.365. The lower experimental value can be accounted for by a small tendency toward specular reflection of the molecules at the surface. By using the value of $C = 1.393$ and $\gamma = 1.405$, the drag coefficients are indicated in Fig. 4 for small Reynolds Number Re. In this flow régime, the C_D is independent of Re. Fig. 4 shows that in the transition region between slip flow and free molecule flow, the drag coefficient actually decreases with decrease in Reynolds Number.

The free molecule flow through a circular tube was first investigated by Knudsen[16] and Smoluchowski.[22] Here the macroscopic velocity of the gas is constant across the section of the tube as could be expected from the large slip in the present case. The pressure drop can be expressed in terms of the pressure drop coefficient Λ defined by Eq. (30) as

$$\Lambda = (3\sqrt{\pi}/\sqrt{2\gamma})(f/2 - f)(1/M) \tag{33}$$

where f is fraction of diffuse reflection as defined previously. By assuming $f = 1$, and $\gamma = 1.405$, values of Λ are calculated from Eq. (33). They are indicated in Fig. 6 at the left side of the diagram. It is seen that, similar to the drag coefficient for the sphere, Λ actually decreases for a decrease of Reynolds Number in the transition region from slip flow to free molecule flow.

The absence of Reynolds Number in Eqs. (32) and (33) simply means that the mean free path does not enter into this type of flow because of the smallness of the body dimension when compared with it. Thus, for both gas dynamical flow and for free molecule flow, viscosity or Reynolds Number is a secondary effect. The primary effect is given by the Mach Number. In the slip flow region, both the Reynolds Number and the Mach Number are of the same importance.

Free Molecule Flow at Large Mach Numbers

Epstein and Smoluchowski assumed the velocity of macroscopic motion to be small in comparison with the microscopic molecular velocity in their investigations of free molecule flows. This means, of course, that the Mach Number of the flow is much smaller than unity. For large Mach Numbers, this restriction must be removed. The calculation should be simple because of the inherent simplicity of the physical situation. Sänger[23, 24] has solved this problem but his calculation[23] is rather complicated. With the belief that a simpler derivation of the fundamental formulas will be helpful for an understanding of his results, the author will try to reproduce his basic equations by following Epstein's general method for free molecule flows.[7]

If ξ', η', ζ' are the components of velocity of a molecule in the directions x', y', z' of a coordinate system in which the macroscopic velocity of the gas is zero, then since the velocity distribution is not modified by the impact with the body because of absence of collision between molecules in the free stream and re-emitted molecules from the surface of the body, the distribution is Maxwellian, or

$$N_{\xi'\eta'\zeta'} = N(h/\pi)^{3/2}\, e^{-h(\xi'^2+\eta'^2+\zeta'^2)} \tag{34}$$

$N_{\xi'\eta'\zeta'}$ is the number of molecules per unit volume in the range of velocities ξ' to $\xi' + d\xi'$, η' to $\eta' + d\eta'$, and ζ' to $\zeta' + d\zeta'$ divided by $d\xi' d\eta' d\zeta'$. N is total of molecules per unit volume. h is related to the most probable velocity c_i of the molecules in the free stream by the expression

$$h = 1/c_i^2 \tag{35}$$

where $c_i^2 = 2RT = 2(p/\rho)$.

Now, if the observer moves with a velocity e_1U, e_2U, e_3U in the directions x', y', z', then in the relative coordinate system x, y, z where the observer is considered at rest, the velocities ξ, η, ζ of the molecule in the directions x, y, z are

$$\begin{aligned} \xi &= \xi' - e_1U \\ \eta &= \eta' - e_2U \\ \zeta &= \zeta' - e_3U \end{aligned} \tag{36}$$

Therefore, in the new coordinate system, the number of molecules having velocity component between ξ, η, ζ and $\xi + d\xi$, $\eta + d\eta$, $\zeta + d\zeta$ is

$$N_{\xi\eta\zeta}\, d\xi\, d\eta\, d\zeta = N\left(\frac{h}{\pi}\right)^{3/2} e^{-h[(\xi+e_1U)^2+(\eta+e_2U)^2+(\zeta+e_3U)^2]} \tag{37}$$

Suppose there is a surface dS whose normal is the x-axis. During 1 sec., the molecules, having velocity components between ξ, η, ζ and $\xi + d\xi$, $\eta + d\eta$, $\zeta + d\zeta$, and striking the surface dS, will be contained at a given moment in the cylinder with dS as base and the length $\sqrt{\xi^2 + \eta^2 + \zeta^2}$ in the direction ξ, η, ζ. The volume of the cylinder is equal to the area of the base dS multiplied by the heights $-\xi$. The number of this kind of molecules is then $N_{\xi\eta\zeta} d\xi\, d\eta\, d\zeta(-\xi)dS$. The number of molecules between ξ, η, ζ and $\xi + d\xi$, $\eta + d\eta$, $\zeta + d\zeta$ that will strike a unit area with x-axis as normal is then $-\xi N_{\xi\eta\zeta} d\xi\, d\eta\, d\zeta$.

To find the total number n of molecules striking this unit area, one has to integrate $-\xi N_{\xi\eta\zeta} d\xi\, d\eta\, d\zeta$ from $\xi = -\infty, \eta = -\infty, \zeta = -\infty$ to $\xi = 0, \eta = \infty, \zeta = \infty$. The upper limit for ξ is easily understood since no molecules with positive velocity in the x-direction can strike this area. Thus

$$n = -N\left(\frac{h}{\pi}\right)^{3/2} \int_{-\infty}^{0} d\xi \int_{-\infty}^{\infty} d\eta \int_{-\infty}^{\infty} \zeta e^{-h[(\xi+e_1U)^2+(\eta+e_2U)^2+(\zeta+e_3U)^2]}\, d\zeta \tag{38}$$

The integration can easily be carried out; the result is

$$n = N\left\{\frac{1}{2\sqrt{\pi h}}\, e^{-h(e_1U)^2} + \frac{e_1U}{2}\left[1 + \operatorname{erf}(e_1U\sqrt{h})\right]\right\} \tag{39}$$

where $\operatorname{erf}(t)$ is the error function[25] defined as

$$\operatorname{erf}(t) = \frac{2}{\sqrt{\pi}} \int_0^t e^{-s^2}\, ds \tag{40}$$

If the velocity U of the motion of the area concerned is inclined with the angle θ with y-axis and in the x-y plane (Fig. 7), then

$$e_1 = \sin\theta, \quad e_2 = \cos\theta, \quad e_3 = 0 \tag{41}$$

Hence, the number of molecules per second striking a unit area of the plate inclined at an angle θ to the stream with velocity U is

$$n = N\left\{\frac{1}{2\sqrt{\pi h}}\, e^{-h(U^2)\sin^2\theta} + \frac{U\sin\theta}{2}\,[1 + \operatorname{erf}\,(U\sqrt{h}\,\sin\theta)]\right\}$$

By multiplying the above equation by the mass of the molecule, the mass m_i of the stream per second striking a unit area of the plate is obtained,

$$m_i = \rho\,\frac{c_i}{2\sqrt{\pi}}\left\{e^{-U^2/c_i^2\sin^2\theta} + \sqrt{\pi}\,\frac{U}{c_i}\sin\theta\left[1 + \operatorname{erf}\left(\frac{U}{c_i}\sin\theta\right)\right]\right\} \tag{42}$$

The component of velocity of the molecule in a direction, having directional cosines e_1', e_2', e_3' with the axes is $e_1'\xi + e_2'\eta + e_3'\zeta$. If this molecule is absorbed by the surface after striking it, the corresponding momentum will be transferred to the surface. For the surface with x-axis as normal as considered previously, the total momentum $M_{e_1', e_2', e_3'}$ per second per unit area is

$$M_{e_1', e_2', e_3'} = -\rho\left(\frac{h}{\pi}\right)^{3/2}\int_{-\infty}^{0} d\xi\int_{-\infty}^{\infty} d\eta\int_{-\infty}^{\infty}\xi(e_1'\xi + e_2'\eta + e_3'\zeta)e^{-h[(\xi+e_1U)^2+(\eta+e_2U)^2+(\zeta+e_3U)^2]}\,d\zeta \tag{43}$$

The result of integration is

$$M_{e_1', e_2', e_3'} = -\frac{\rho}{2}U^2\left\{\frac{1}{\sqrt{\pi h}U}(e_1e_1' + e_2e_2' + e_3e_3')e^{-h(e_1U)^2} + \left[\frac{e_1'}{2hU^2} + e_1(e_1e_1' + e_2e_2' + e_3e_3')\right][1 + \operatorname{erf}\,(U\sqrt{h}\,e_1)]\right\} \tag{44}$$

For calculating the pressure p_i due to impact of molecules on a plate inclined at an angle θ to the stream of velocity U,

$$\begin{aligned} e_1 &= \sin\theta \quad & e_1' &= -1 \\ e_2 &= \cos\theta \quad & e_2' &= 0 \\ e_3 &= 0 \quad & e_3' &= 0 \end{aligned} \tag{45}$$

By substituting Eq. (45) into Eq. (43), the impact pressure p_i is calculated by

$$\frac{p_i}{{}^1/_2\,\rho U^2} = \sin\theta\,\frac{c_i}{U}\,e^{-(U^2/c_i^2)\sin^2\theta} + \left(\frac{1}{2}\,\frac{c_i^2}{U^2} + \sin^2\theta\right)\left[1 + \operatorname{erf}\left(\frac{U}{c_i}\sin\theta\right)\right] \tag{46}$$

Eq. (46) reduces to particularly simple forms for the two limiting cases of $U = 0$ and $U \gg c_i$. When $U = 0$, the impinging pressure is

$$p_i = {}^1/_4\,\rho c_i^2$$

This is one-half of the pressure acting on the surface calculated by the kinetic theory as the other half is the result of the reflection of molecules. For $U \gg c_i$ and $\theta = 90°$, the impinging pressure is

$$p_i = \rho({}^1/_2 c_i^2 + U^2)$$

This checks with the result of Zahm[1] except for a factor of 2 which is accounted for by the fact that here only pressure due to impinging molecules is calculated, not the total pressure. Zahm obtained the result by simply assuming that $U \geq c_i$ and the molecules all having the same speed c_i but with random distribution in their directions of motion. The later assumption is, of course, an oversimplification. However, if $U \gg c_i$, the spread of the speeds of the molecule is relatively unimportant. Then the present more accurate calculation should rightly give the same result as Zahm.

To calculate the shearing stress τ_i due to impact of molecules on the plate, the direction cosines are

$$\begin{aligned} e_1 &= \sin\theta \quad & e_1' &= 0 \\ e_2 &= \cos\theta \quad & e_2' &= -1 \\ e_3 &= 0 \quad & e_3' &= 0 \end{aligned} \tag{47}$$

By substituting Eq. (47) into Eq. (43),

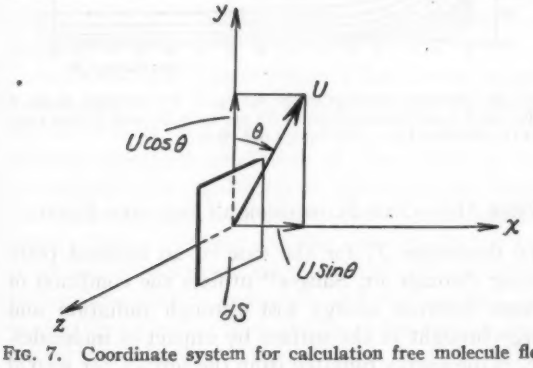

FIG. 7. Coordinate system for calculation free molecule flow.

$$\frac{\tau_i}{{}^1/_2\,\rho U^2} = \cos\theta\,\frac{c_i}{U}\,e^{-(U^2/c_i^2)\sin\theta} + \sin\theta\cos\theta\left[1 + \operatorname{erf}\left(\frac{U}{c_i}\sin\theta\right)\right] \quad (48)$$

If the molecules reflect specularly from the surface, then motion of the impinging molecules normal to the surface is simply reversed in re-emission, while the tangential velocity is maintained. Then it is easy to see that the pressure due to re-emission is $p_r = p_i$ and the shearing stress due to re-emission is $\tau_r = -\tau_i$. On the other hand, if the molecules re-emit diffusely, $\tau_r = 0$, since no preferred direction exists. To calculate the pressure p_r due to diffuse re-emission, one observes that according to the kinetic theory,

$$p_r = (\text{mass emitted per second per unit area})\ (\sqrt{\pi}/2)c_r \quad (49)$$

where c_r is the most probable velocity of the molecule in thermal equilibrium at a temperature T_r of the re-emitted gas. Thus

$$c_r^2 = 2RT_r \quad (50)$$

But the mass re-emitted must be equal to the mass m_i striking the surface, as given by Eq. (40). Thus,

$$\frac{p_r}{{}^1/_2\,\rho U^2} = \frac{\sqrt{\pi}}{2}\frac{c_i}{U}\frac{c_r}{U}\frac{e^{-(U^2/c_i^2)\sin^2\theta}}{\sqrt{\pi}} + \frac{\sqrt{\pi}}{2}\frac{c_r}{U}\sin\theta\left[1 + \operatorname{erf}\left(\frac{U}{c_i}\sin\theta\right)\right] \quad (51)$$

(diffuse reflection).

The total pressure due to both impinging and re-emission, with f fraction of the molecules reflected diffusely and $(1 - f)$ fraction of the molecule reflected specularly is

$$\frac{p}{{}^1/_2\,\rho U^2} = (2 - f)\frac{p_i}{{}^1/_2\,\rho U^2} + f\frac{p_r}{{}^1/_2\,\rho U^2} \quad (52)$$

The corresponding shearing stress is

$$\tau/{}^1/_2\,\rho U^2 = f(\tau_i/{}^1/_2\,\rho U^2) \quad (53)$$

These equations can be also written in terms of Mach Numbers by the substitution

$$\frac{U}{c_i} = \sqrt{\frac{\gamma}{2}}\,M,\ \frac{U}{c_r} = \sqrt{\frac{\gamma}{2}}\,M\left(\frac{c_i}{c_r}\right) \quad (54)$$

where M is the free stream Mach Number.

The temperature T_r has to be determined by a consideration of the accommodation coefficient α. The energy content of the molecules from the wall is proportional $(1 - f)T_0^\circ + fT_r$ where T_0° is the stagnation temperature of the free stream. Therefore, according to the definition given in Eq. (20),

$$\alpha = \frac{T_0^\circ - [(1-f)T_0^\circ + fT_r]}{T_0^\circ - T_w} = \frac{f(T_0^\circ - T_r)}{T_0^\circ - T_w} \quad (55)$$

where T_w is the temperature of the surface. If α and T_w are given, T_r can be calculated from this equation.

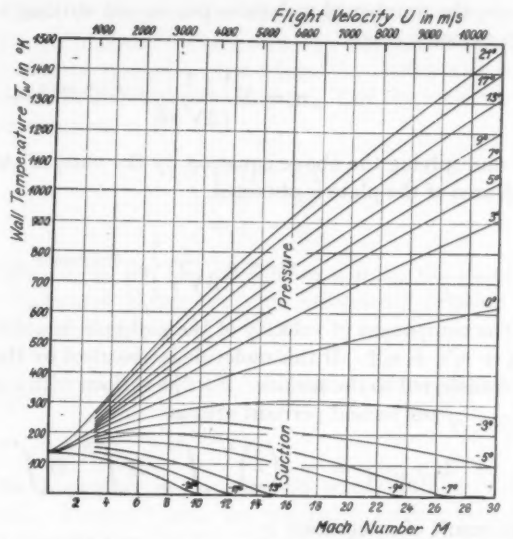

FIG. 8. Surface temperature T_w for various angles θ to the wind in an atmosphere of 86 per cent N_2 and 14 per cent O_2 at the density 1.9×10^{-9} slugs per cu.ft. Air temperature = 320 °K.

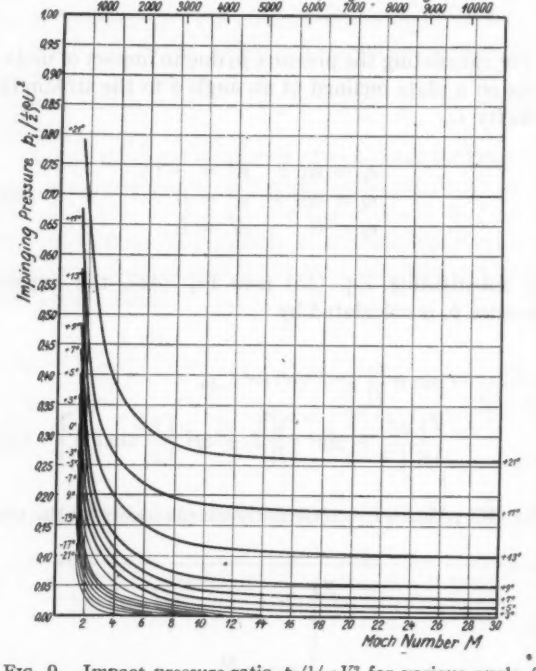

FIG. 9. Impact pressure ratio $p_i/{}^1/_2\rho V^2$ for various angle θ to the wind in an atmosphere of 86 per cent N_2 and 14 per cent O_2 at the density 1.9×10^{-9} slugs per cu.ft.

FREE MOLECULE FLOW OVER AN INCLINED PLATE

To determine T_r for the case of an inclined plate moving through air, Sänger[24] utilizes the condition of balance between energy lost through radiation and energy brought to the surface by impact of molecules. If E_s is the energy radiated from the surface per second

per unit area, then it is related to the energy E_i brought to the plate and the energy E_r carried away from the plate by

$$E_s = E_i - E_r \tag{56}$$

Let $\epsilon_{\text{trans.}}$, $\epsilon_{\text{rot.}}$, $\epsilon_{\text{vib.}}$ be the translational energy, the rotational energy, and the vibrational energy per until mass of the gas. Since experiments and theoretical considerations indicate that the re-emission is mostly diffuse, Sänger takes $f = 1$. Then, if m_i is the mass brought to and re-emitted from the surface per unit per unit time,

$$E_i = m_i(\tfrac{1}{2}U^2 + \epsilon_{i\,\text{trans.}} + \epsilon_{i_{\text{rot.}}} + \epsilon_{i_{\text{vib.}}} \tag{57}$$

$$E_r = m_i(\epsilon_{r_{\text{trans.}}} + \epsilon_{r_{\text{rot.}}} + \epsilon_{r_{\text{vib.}}} \tag{58}$$

The corresponding energies for a gas temperature T_w is $\epsilon_{w_{\text{trans.}}}$, $\epsilon_{w_{\text{rot.}}}$ and $\epsilon_{w_{\text{vib.}}}$. Sänger then assumes that the accommodation coefficients for translational and rotational energies are unity, while the accommodation coefficient for vibrational energy is zero because of its slow rate of adjustment.

Then

$$\begin{aligned} \epsilon_{i_{\text{trans.}}} - \epsilon_{r\ \text{trans.}} &= \epsilon_{i_{\text{trans.}}} - \epsilon_{w_{\text{trans.}}} \\ \epsilon_{i_{\text{rot.}}} - \epsilon_{r_{\text{rot.}}} &= \epsilon_{i_{\text{rot.}}} - \epsilon_{w_{\text{rot.}}} \\ \epsilon_{i_{\text{vib.}}} - \epsilon_{r_{\text{vib.}}} &= 0 \end{aligned} \tag{59}$$

Hence, $\epsilon_{r_{\text{trans.}}} = \epsilon_{w_{\text{trans.}}}$, $\epsilon_{r_{\text{rot.}}} = \epsilon_{w_{\text{rot.}}}$, $\epsilon_{r_{\text{vib.}}} = \epsilon_{i_{\text{vib.}}}$ and

$$c_r = \sqrt{2RT_w} \tag{60}$$

Therefore, Eq. (58) can be written as

$$E_r = m_i(\epsilon_{w_{\text{trans.}}} + \epsilon_{w_{\text{rot.}}} + \epsilon_{i_{\text{vib.}}}) \tag{61}$$

By substituting Eqs. (57) and (61) into Eq. (56), one has immediately

$$E_s = m_i[\tfrac{1}{2}U^2 + (\epsilon_{i_{\text{trans.}}} - \epsilon_{w_{\text{trans.}}}) + (\epsilon_{i_{\text{rot.}}} - \epsilon_{w_{\text{rot.}}})] \tag{62}$$

For nitrogen and oxygen the equipartition value of the rotational energy is reached at even exceedingly low temperatures. Therefore,

$$\epsilon_{\text{trans.}} = 3/2RT$$

$$\epsilon_{\text{rot.}} = 2/2RT$$

Hence Eq. (61) gives

$$E_s = m_i\ [\tfrac{1}{2}\ U^2 + \tfrac{5}{2}R(T_i - T_w)] \tag{63}$$

where m_i is given by Eq. (42). T_i is the free stream temperature T_0.

As an example, Sänger assumes that the air temperature is equal to $T_i = T_0 = 320°\text{K}$. (47°C.). The air density is 1.904×10^{-9} slugs per cu.ft. The density ratio referred standard conditions is thus 0.802×10^{-6}, corresponding to an altitude of approximately 55 miles. The mean free path according to Table 1 is thus approximately 3.5 in. Sänger actually assumed the air to be composed of 14 per cent oxygen and 86 per cent nitrogen without considering ionization and dissociation. Neglecting the radiation from the air to the surface, he assumed the emissivity of the surface to be 0.80. Thus

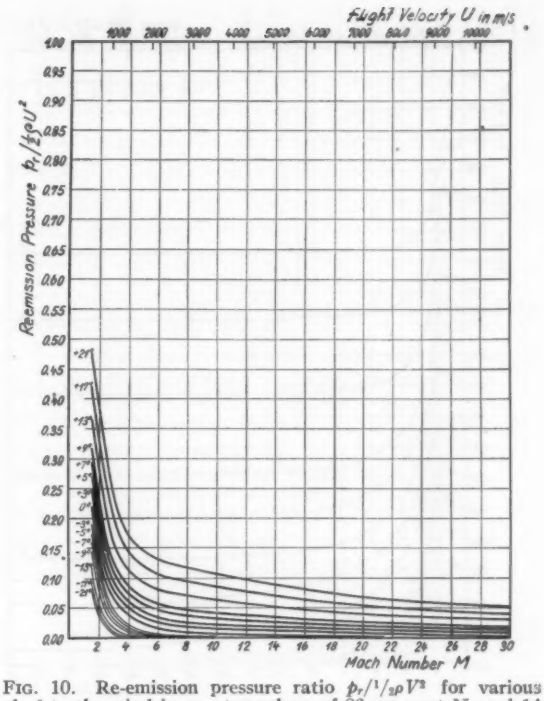

FIG. 10. Re-emission pressure ratio $p_r/\frac{1}{2}\rho V^2$ for various angle θ to the wind in an atmosphere of 86 per cent N_2 and 14 per cent O_2 at the density 1.9×10^{-9} slugs per cu.ft.

$$E_s = 0.80\sigma T_w^4$$

where σ is the Stefan-Boltzmann constant for radiation. The results of calculation of the wall temperature T_w are shown in Fig. 8. It is interesting to note that because of radiation, the wall temperature is considerably lower than the air temperature for low air velocities and suction side. The value of c_r can be calculated by Eq. (60). The stresses acting on the surface can then be computed with Eqs. (52) and (53). The pressure ratios $p_i/\frac{1}{2}\rho U^2$ and $p_r/\frac{1}{2}\rho U^2$ for impinging and diffuse reemission ($f = 1$) are given in Figs. 9 and 10, also taken from Sänger's paper. The shearing stress is given in Fig. 11. The extremely high shearing force is evident.

If the dimension of a flat plate airfoil is much less than the mean free path, Eqs. (52) and (53) can be used to calculate the lift and drag. Thus, for diffuse reflection ($f = 1$), and for an angle of attack α, the lift coefficient C_L and the drag coefficient C_D are

$$C_L = \sqrt{\frac{2\pi}{\gamma}}\frac{1}{M}\left(\frac{c_r}{c_i}\right)\sin\alpha\cos\alpha + \frac{2}{\gamma}\frac{1}{M^2}\cos\alpha\,\text{erf}\left(\sqrt{\frac{\gamma}{2}}\,M\sin\alpha\right) \tag{64}$$

$$C_D = \sqrt{\frac{8}{\gamma}}\frac{1}{M}e^{-(\gamma/2)\,M^2\sin^2\alpha} + \sqrt{\frac{2\pi}{\gamma}}\frac{1}{M}\left(\frac{c_r}{c_i}\right)\sin^2\alpha + 2\left(\frac{1}{\gamma M^2} + 1\right)\sin\alpha\,\text{erf}\left(\sqrt{\frac{\gamma}{2}}\,M\sin\alpha\right) \tag{65}$$

Sänger's result for the flat plate airfoil is given in Fig.

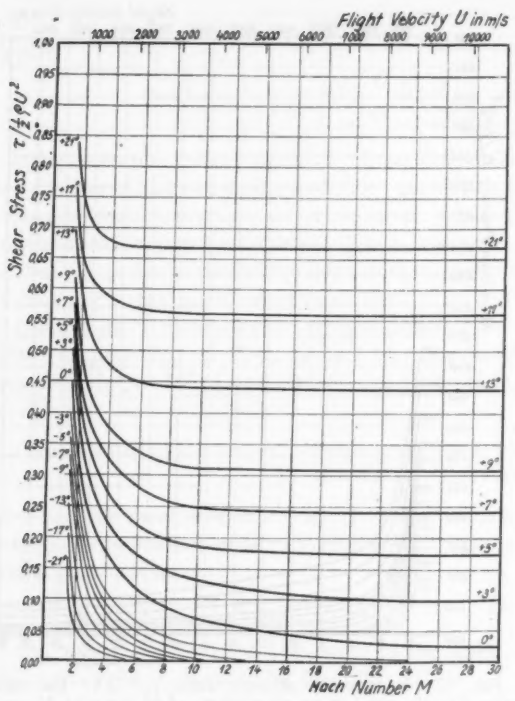

FIG. 11. Shear stress ratio $\tau/\frac{1}{2}\rho V^2$ for various angle θ to the wind in an atmosphere of 86 per cent N_2 and 14 per cent O_2 at the density 1.9×10^{-9} slugs per cu.ft.

12. The lift-drag ratio is less than unity, showing the poor efficiency of the surface under free molecule flow conditions. Of course, the calculated values hold true only for wing dimensions much less than the mean free path, i.e., less than 3.5 in. for the case under consideration.

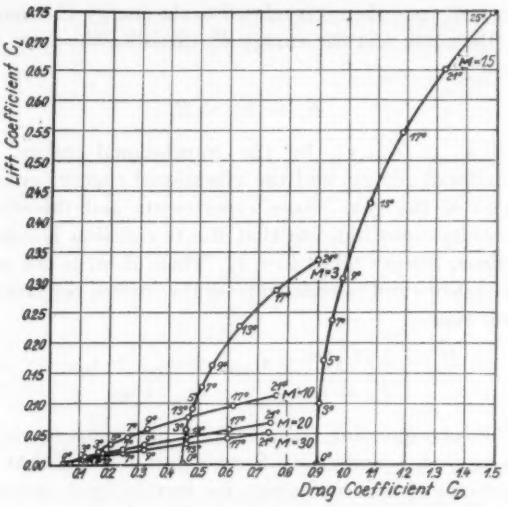

FIG. 12. Polar diagram for a flat plate at various angles of attack in an atmosphere of 86 per cent N_2 and 14 per cent O_2 at the density 1.9×10^{-9} slugs per cu.ft.

REFERENCES

[1] Zahm, A. F., *Superaerodynamics*, Journal of The Franklin Institute, Vol. 217, pp. 153–166, 1934.

[2] Chapman, S., *On the Law of Distribution of Molecular Velocities, and on the Theory of Viscosity and Thermal Conduction, in a Non-Uniform Simple Monatomic Gas*, Phil. Trans. Roy. Soc., Vol. 216(A), pp. 279–348, 1915.

[3] Maris, H. B., *The Upper Atmosphere*, Terr. Magn., Vol. 33, pp. 233–255, 1928; Vol. 34, pp. 45–53, 1929.

[4] Burnett, D., *The Distribution of Molecular Velocities and the Mean Motion in a Non-Uniform Gas*, Proc. Lond. Math. Soc., Vol. 40, p. 382, 1935. See also Chapman, S., and Cowling, T. G., *The Mathematical Theory of Non-Uniform Gases*, 1st Ed., Chap. 15; Cambridge University Press, London, 1939.

[5] Millikan, R. A., *Coefficients of Slip in Gases and the Law of Reflection of Molecules from the Surfaces of Solids and Liquids*, Physical Review, Vol. 21, pp. 217–238, 1923.

[6] van Itterbeck, A., and Mariens, P., *Measurements on the Absorption of Sound in O_2 Gas and in CO_2 Gas Containing Small Quantities of H_2O, D_2O and Ne. Relaxation Times for Vibrational Energy*, Physica, Vol. 7, pp. 125–130, 1940.

[7] Epstein, P. S., *On the Resistance Experienced by Spheres in Their Motion Through Gases*, Physical Review, Vol. 23, pp. 710–733, 1924.

[8] See, for instance, Kennard, E. H., *Kinetic Theory of Gases* pp. 328–332; McGraw-Hill Book Co., Inc., New York, 1938.

[9] Kennard, *Ibid.*, pp. 312–315.

[10] Knudsen, M., *Die molekulare Warmeleitung der Gase und der Akkommodationskoefficient*, Ann. Physik, Vol. 34, pp. 593–656, 1911.

[11] See, for instance, Kennard, *op. cit.*, p. 323.

[12] Wiedmann, M. L., *Thermal Accommodation Coefficient*, Trans. of A.S.M.E., Vol. 68, pp. 57–64, 1946.

[13] See, for example, Lamb, H., *Hydrodynamics*, 6th Ed., pp. 594–617; Cambridge University Press, London, 1932.

[14] Basset, A. B., *Hydrodynamics*, Vol. 2, pp. 270–271; Deighton, Bell and Co., Cambridge, 1888, or Lamb, *op cit.*, pp. 602–604.

[15] Lamb, *op. cit.*, pp. 615, 616.

[16] Knudsen, M., *Die Gesetze der Molekularströmung und der inneren Reibungsströmung der Gase durch Rohren*, Ann. Physik, Vol. 28, pp. 75–130, 1909.

[17] Knudsen, M., *Molekularströmung des Wasserstoffs durch Rohren und das Hitzdrahtmanometer*, Ann. Physik, Vol. 35, pp. 389–396, 1911.

[18] Gaede, W., *Die äussere Reibung der Gase*, Ann. Physik, Vol. 41, pp. 289–336, 1913.

[19] Ebert, H., *Das Strömen von Gasen bei niedrigen Drucken*, Physikalische Zeitschrift, Vol. 33, pp. 145–151, 1932.

[20] Ebert, H., *Darstellung der Strömungsvorgange von Gasen bei niedrigen Drucken mittels Reynoldsscher Zahlen*, Zeitschrift für Physik, Vol. 85, pp. 561–564, 1933.

[21] Millikan, R. A., *The General Law of Fall of a Small Spherical Body Through a Gas, and Its Bearing upon the Nature of Molecular Reflection from Surfaces*, Physical Review, Vol. 22, pp. 1–23, 1923.

[22] Smoluchowski, M. v., *Zur kinetischen Theorie der Transpiration und Diffusion verdünnter Gase*, Ann. Physik, Vol. 33, pp. 1559–1570, 1910.

[23] Sänger, E., *Gaskinetik sehr hoher Fluggeschweindigkeiten*, Deutsche Luftfahrtforschung, Bericht 972, Berlin, 1938.

[24] Sänger, E., and Bredt, J., *Uber einen Raketenantrieb für Fernbomber*, Deutsche Luftfahrtforschung, Untersuchungen u. Mitteilungen Nr. 3538, pp. 141–173, Berlin, 1944.

[25] The error function is tabulated. See, for instance, Jahnke-Ende *Tables of Functions*, 3rd Ed., p. 24; B. G. Teubner, Liepzig, 1938; or *Tables of Probability Functions*, Vols. I and II; National Bureau of Standards, Washington, D.C., 1943.

An Investigation of the Airflow Underneath Helicopter Rotors

ROBERT S. ROSS*

Daniel Guggenheim Airship Institute

SUMMARY

The airflow underneath helicopter rotors, as determined by the classical blade element and momentum theories without the assumptions of constant chord or constant circulation along the span, was estimated from theoretically determined charts. These values were compared with those obtained from the actual measurements taken near a model rotor with a "hot wire" anemometer.

Both time average and instantaneous readings of velocity were taken at simulated hovering and horizontal flight conditions. These measurements showed the theoretical estimation to be good at low angles of attack and at positions not too near the blade tips. They also indicated the pulsations that occur in horizontal flight, and showed these to be of unanticipated magnitude. Positions of maximum and minimum effect were tested to get the range of pulsation.

This method of determining rotor characteristics was different from those now employed, and the equipment used was built specially for these tests. The instruments were easy to handle and offered an improved picture of the distribution of rotor forces.

DEFINITION OF TERMS

α	= angle whose tangent is D/L
α_0	= angle of attack of the blade sections
α_1	= angle between the rotor disc and horizontal plane
β	= angle the relative wind makes with the rotor plane
b	= number of rotor blades
c	= chord of rotor blade
C_D	= coefficient of drag of airfoil
C_L	= coefficient of lift of airfoil
D	= drag of the rotor blade
dD	= drag for section of span dr
dL	= lift for section of span dr
dr	= elemental section of blade
dT	= elemental thrust for section of span dr
dQ	= elemental rotor torque for section of span dr
dW_0	= elemental weight to be lifted by section of span dr
K	= drag over lift ratio
K_1	= $1 - \sqrt{1 - P^2 - 2KP}$
L	= lift of the rotor blade
L_1	= $\{\sqrt{1 - [(P^2 + 2sP + 2KP)/(1 - Ks)^2]}\}$
M	= $(2s + P)$
n	= r.p.s. of the rotor
N	= $(1 - Ks)$
p or P	= ratio of the induced axial velocity to the rotational velocity for hovering flight
Q	= rotor torque
r	= radius of blade to section
R	= tip radius of rotor blades
ρ	= mass density of air (0.002378 for standard air)
s	= ratio of the axial velocity to the rotational velocity
θ	= blade position with respect to the direction of the horizontal velocity
u	= rotational (or tangential) velocity of the rotor
u'	= induced rotational (or tangential) velocity
u_2	= rotational velocity when rotor is tipped
v	= axial velocity of the rotor
v'	= induced axial velocity
v_1'	= axial induced velocity for horizontal flight
v_2'	= induced axial velocity when rotor is tipped
W	= relative wind velocity for hovering flight
W_0	= weight to be lifted by rotor
Y	= horizontal velocity of helicopter
Y_2	= horizontal velocity component in plane of rotor disc
Z	= resultant force on airfoil
Z_3	= resultant induced velocity from airfoil

Presented at the Rotating Wing Aircraft Session, Fourteenth Annual Meeting, I.A.S., New York, January 29–31, 1946.

* Technical Director.

INTRODUCTION

FOR A GREAT NUMBER OF YEARS people have tried to solve the helicopter problems and build a practical man-carrying machine. However, it was not until the last couple of years that research has concentrated on the various helicopter difficulties and tried to find out more about them. Since the 15th century, adventurous people have been building helicopters of every variety and combination, each trying to make a completed machine. The basic principle of flight appeared so simple that no attempt was made to isolate any of the aerodynamics involved. As a matter of fact, few experimenters realized that there were such problems as stability, vibration, or controllability. Their main trouble lay in trying to produce a rotor that would lift their machine with the power available.[1]

Today, however, both rotor and propeller design have advanced to such a stage that the lifting problem has been solved. No sooner had a helicopter been built which would rise off the ground than all the complications began to appear. It became evident that much concentrated research was needed on each particular phase of helicopter flight to enable the design engineers to anticipate and try to solve these problems.

One of the unknown values which had come up time and time again was the distribution of the flow under the rotor blades. It was the purpose of this investigation to try to give some answer to this question. In order to do this, it was necessary to develop experimental equipment capable of checking the validity of the use of basic helicopter theories.

Description of Apparatus

All of the rotor tests were made in the 6 ft. 6 in. vertical wind tunnel of the Daniel Guggenheim Airship Institute. The rotor blades were mounted rigidly to the rotor shaft, the plane of the blades being 5 ft. above the tunnel mouth for hovering tests. The rotor shaft, in turn, was connected through a set of reduction gears to a $^1/_3$-hp., 10,000-r.p.m. 110-volt a.c. motor. The motor, gearing, shaft, and blades were all connected at the motor end to a specially devised arrangement of flat springs. The rotor end was supported by ball bearings mounted inside of a protective tube that extended from the blades to the motor housing.

Force Apparatus

The entire arrangement, except for the rotor blades, of course, was housed in a streamlined shield to prevent any interference from the air and to reduce to a minimum any effect of the machine on the airflow itself.

The motor was prevented from moving in either an axial or rotating direction by the flat spring support on the bottom of the instrument. Two of the springs were crossed; this enabled the motor to rotate a fraction of a degree but prevented it from moving in the axial direction. The other spring prevented the first set of springs from rotating but allowed them to move axially just a fraction of an inch. By mounting strain gages on these two sets of springs, the tendency to move in either the axial or rotary direction could be measured. These values, when calibrated, gave the thrust and torque of the rotor blades.

The strain gages, which were mounted on the springs in this force apparatus, formed part of a bridge circuit. The unbalance of this circuit due to the stretching of the gages was amplified and recorded on Esterline Angus recorders, which were calibrated to measure the thrust and torque of the rotor blades. This part of the apparatus therefore gave the performance characteristics as measured at the shaft and was used as a qualitative check on the induced velocity measurement.

"Hot Wire" Indicators

In order to measure the velocity and direction of the air under the rotor blades, a special "hot wire" instrument was used. These wires were mounted at the end of a long probe, which, in turn, was supported in an adjustable clamp enabling its placement at any desired position under the blades. The "wires" themselves consisted of two separate units: one for the direction indication, and the other for the velocity. The direction unit was made up of two $^1/_8$-in. long wires in the form of a V. The velocity unit was one $^1/_8$-in. long wire set at right angles to the plane of the direction V. All wires used were 0.0006-in. diameter platinum strands. They were strung between needle points properly spaced at the end of the adjustable probe.

The two sides of the V of the direction wire made up two arms of a bridge circuit. If the bridge showed a balance, it meant that these two sides of the V were equally cooled by the airflow, and the direction of this flow could be read on a large protractor on the probe. The velocity wire made up part of another bridge circuit, the unbalance of which was amplified and recorded on another Esterline Angus recorder. This recorder was calibrated to read the velocity of the air passing over the wire. The entire "hot wire" unit was no larger than a sphere of approximately $^3/_{16}$-in. diameter. This enabled "point" investigations, since it was so small.

The "hot wire" instrument was calibrated in a special small wind tunnel. It consisted of a 7-in. diameter tube about 3 ft. long, at one end of which was mounted the motor and fan. The tube was fitted with screens at the entrance and "egg crates" at the exit so as to obtain relatively smooth flow. This small wind tunnel was equipped with a $^1/_{16}$-in. diameter pitot tube connected to an alcohol manometer inclined to 5° with the horizontal. A small hole in the side of the tunnel $^1/_2$ in. in diameter enabled one to insert the "hot wire" probe until the wires rested at the center of the tube. Velocities from 0 to about 30 ft. per sec. could be obtained here. The speed of the tunnel motor was regulated with a variable inductance. Both the velocity and direction wires were calibrated in this tunnel for low velocity readings.

In order to measure the instantaneous velocities, a "hot wire" about $^1/_2$ in. in length was installed at the end of the probe. This wire was connected through a bridge circuit to an oscillograph on which a photographic record of the velocity changes could be made. A two-element unit was used so that a 60-cycle timing wave could be photographed alongside the velocity picture. Records were made by either drawing the film over the light spots in an X direction while spots were restricted to move in the Y direction or by allowing the light spots to scan a photographic film screen once while moving in both the X and Y directions. The film, when developed, made a permanent record that could be easily studied.

Types of Rotor Blades

The rotor blades used for the tests were made of mahogany wood shaped to an NACA 0015 profile. Three sets of rotors were tested, each set employing three 2 ft blades. The first set had a constant chord of 2 in. and was twisted so that the root was 10° greater than the tip. The second and third sets were tapered so that the root chord length was $2^3/_4$ in. and the tip was $1^1/_4$ in. One of these sets was not twisted, while the other had a 10° twist similar to that of the constant chord set. The blades, which were fitted with a tapped socket at the root end, were screwed to a small hub and held rigidly in place by a lock nut.

Test Procedure

"Hot Wire" Measurements

The first investigations made were those with the "hot wire." Before starting the calibrations, it was necessary to check the "hot wires" themselves to make sure that they were well soldered to their needle supports and that good electrical contact was made throughout the circuits. The "hot wire" unit was then plugged into the long probe, and the probe was swung around into position so that the wire rested in the center of the small calibrating tunnel. The electrical apparatus was then calibrated so that the Esterline Angus recorder would read the velocity over the wire, while the angle of the direction wire was maintained at zero by rotating the entire probe. In order to best utilize the recorder for the majority of the velocities to be encountered, it was necessary to balance the velocity bridge with the tunnel operating at a low velocity. This gave better accuracy to the values taken but prohibited the recording of zero velocity itself. The "hot wire" was calibrated before each run to make sure that such things as the change in temperature of the air in the room and its effect on the wire did not enter into the results.

So as to produce hovering flight conditions, the rotor blades were placed in the tunnel so that the plane of the blades was horizontal and about 5 ft. above the tunnel mouth. Because it was a vertical tunnel, the opening under the blades helped remove the ground effect. The turning vanes and corner of the tunnel, the first solid obstructions under the blades, were about 25 ft. from the helicopter rotor. All of the tests were run in semi-darkness. A Strobotac was used to determine the rotor speed, which was kept constant at 450 r.p.m. This value was chosen arbitrarily because the equipment ran well at that speed.

After the "hot wire" was calibrated, the tunnel room was darkened, and the probe was swung into a position so that the "hot wire" could be easily moved underneath the rotor disc. Velocity and direction readings were then taken in a plane about 2 in. below the rotor disc, and a complete traverse was made from a radius of about 2 in. to about 24 in. At extremely low velocities the readings could not be taken, and at positions where the air was turbulent the readings were not accurate. However, regions of these conditions did not contribute much to the effectiveness of the blade, so this was no great loss. Readings were taken radially at 1-in. intervals, the resultant velocities and directions being recorded.

Horizontal Flight Tests

So as to obtain horizontal flight conditions, the rotor was inclined in the air stream until the plane of the blade was parallel to the direction of the wind-tunnel air flow. The supports of the motor housing were moved back so that the rotor blades themselves remained well within the air stream. The rotor chosen to be investigated was the one with the nontapered, twisted blades that were set at $(\beta + \alpha_0) = 20°$ at the root. These were mounted rigidly at the rotor hub, and the "hot wire" probe was mounted so that measurements could be taken at 2 in. below the plane of the blades. The velocity and direction "hot wire" unit was first used, and readings were taken at 1-in. intervals along the radius of the blades. Then the instantaneous velocity wire was installed and readings were taken only at several representative points.

The wind-tunnel velocity, which was determined by a pitot tube mounted in the air stream, was held at a constant value depending upon the test desired. Since the wire would burn out at zero air velocity, care had to be exercised that air was flowing past the wire before the current was turned on. This was necessary because high current had to be maintained through the wire to obtain the sensitivity desired.

Helicopter Theory

An examination of the airflow around a helicopter rotor blade with the primary purpose of determining design criteria was the main function of this investigation. By the use of the well-known blade element and momentum theories, formulas were developed which would give the characteristics of the rotor blades under various attitudes of flight.[2] These formulas, which become quite complicated when both the lift and drag of the blade element are considered, were plotted in curve form and in that way present a simple and rapid means of their solution for any particular flight condition.

All the important design factors were included in one "design coefficient" ($C_L bc/r$) which is dependent upon the spanwise blade loading and the rotational speed of the blade. The physical characteristics of the blade shape would therefore be determined by the structural ability of the blade to handle the load given it. Once the possible blade loading is decided upon, it would be a matter of applying these values to the above-mentioned curves to obtain the $C_L bc/r$ value for any section.

The general solution of the problem was considered first, and then various possible flight conditions, such as hovering and horizontal flight, were investigated. The entire theory was determined primarily from the basic blade element and momentum theories and was developed from there.

Taking a rotor blade section of span dr (as illustrated in Fig. 1) and examining the airflow at that point where r is the radius of the rotor to that section, c is the chord of the rotor section, and R is the tip radius, one finds the conditions illustrated in Fig. 2. These can be analyzed as follows:

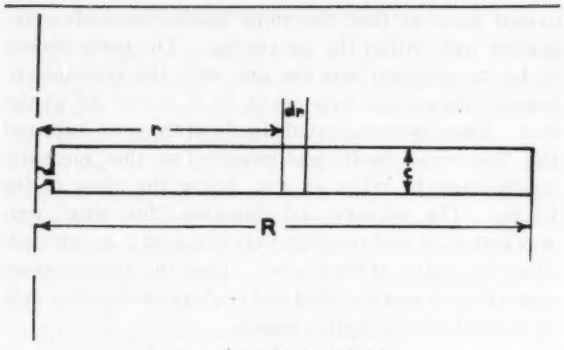

FIG. 1. Rotor blade definition.

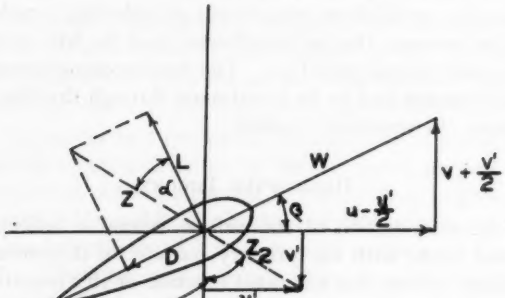

FIG. 2. Velocity and force diagram on cross section of rotor blade.

Let the terms be defined so that

- v = the velocity entering the rotor disc (axial velocity of the rotor)
- u = the rotational velocity of the rotor
- v' = the increase in axial velocity or induced axial velocity
- u' = the increase in tangential (rotational) velocity or induced tangential velocity
- dL = lift of the rotor section
- dD = drag of the rotor section
- W = velocity relative to the rotor section

If W is the relative velocity of the air with respect to the blade section, then the lift component dL must be perpendicular to W and the drag component dD must be parallel to it. The resultant of these lift and drag components is Z, which makes an angle α with the lift vector.

This force Z has a reaction on the air equal and opposite to it. Call the velocity set up by this force an induced velocity and give it the value Z_2. Z_2 can then be broken up into its horizontal and vertical components u' and v', respectively. If β is the angle the relative velocity W makes with the horizontal axis, then Z_2 makes the angle $(\beta + \alpha)$ with the vertical axis, and

$$\tan (\beta + \alpha) = u'/v' \tag{1}$$

According to the momentum theory, if the overall increase of velocity is v', then the increase at the blade is one-half of that or $v'/2$. Applying this to both the tangential and axial velocities, it is found that the relative velocity W is made up of the axial velocity $[v + (v'/2)]$ and the tangential velocity $[u - (u'/2)]$. From this new vector triangle, it is clear that

$$\tan \beta = [v + (v'/2)]/[u - (u'/2)] \tag{2}$$

Expanding Eq. (1),

$$u'/v' = (\tan \beta + \tan \alpha)/(1 - \tan \beta \tan \alpha) \tag{3}$$

Since the $\tan \alpha = dD/dL$ or C_D/C_L, Eq. (2) can be substituted in Eq. (3) to give

$$\frac{u'}{v'} = \frac{\{[v + (v'/2)]/[u - (u'/2)]\}}{1 - \{[v + (v'/2)]/[u - (u'/2)]\}} + \left(\frac{C_D/C_L}{C_D/C_L}\right) \tag{4}$$

Let $C_D/C_L = K$ and simplify Eq. (4). This gives

$$v'\left[\left(\frac{2v + v'}{2u - u'}\right) + K\right] = u'\left[1 - \left(\frac{2v + v'}{2u - u'}\right)K\right] \tag{5}$$

Expanding Eq. (5) gives

$$2vv' + v'^2 + 2Kv'u - Kv'u' = 2uu' - u'^2 - 2vu'K - u'v'K \tag{6}$$

Collecting terms and rearranging Eq. (6) so that it would be possible to solve for u' yields

$$u'^2 - 2u'(u - vK) + v'^2 + 2vv' + 2Kv'u = 0 \tag{7}$$

Solving Eq. (7) for u',

$$u' = 2(u - vK) \pm \sqrt{4(u - vK)^2 - 4(v'^2 + 2vv' + 2Kv'u)} \tag{8}$$

$$u' = (u - vK) \pm \sqrt{(u - vK)^2 - (v'^2 + 2vv' + 2Kv'u)} \tag{9}$$

In order to analyze Eq. (9) to find out which sign applies, rearrange it into this form:

$$u' = (u - vK) \pm (u - vK) \times \sqrt{\frac{(u - vK)^2 - (v'^2 + 2vv' + 2Kv'u)}{(u - vK)^2}} \tag{10}$$

$$u' = (u - vK)\left[1 \pm \sqrt{1 - \frac{v'^2 + 2vv' + 2Kv'u}{(u - vK)^2}}\right] \tag{11}$$

To simplify the equation even further, consider the condition where the axial velocity v is equal to zero. The expression $(u - vK)$ then becomes u, and the value inside the brackets must be equal to or less than 1 because u' cannot be larger than u. This means that the negative sign must be employed, since the value under the radical always lies between zero and 1.

Consider now the force that can be obtained from this blade section. Since

force = thrust = mass × acceleration = (mass/sec.) (change in velocity)

the following relationship can be set up:

$$dT = 2\pi r \rho dr v_{\text{(average axial)}} \times v_{\text{(axial)}} \quad (12)$$

where dT is the elemental thrust force and ρ is the mass density of the air. The average axial velocity is equal to the velocity at the section or $[v + (v'/2)]$, while the change in axial velocity is the v' mentioned earlier. Substituting these values in Eq. (12) gives

$$dT = 2\pi r dr \rho [v + (v'/2)]v' \quad (13)$$

which, when simplified, yields

$$dT/dr = \pi r \rho (2vv' + v'^2) \quad (14)$$

To find the axial thrust of the rotor section by another method, the following equation can be set up:

$$\text{thrust} = L \cos \beta - D \sin \beta \quad (15)$$

or

$$\text{thrust} = (C_L \cos \beta - C_D \sin \beta)\rho \frac{(\text{velocity})^2}{2} \text{ area} \quad (16)$$

where the velocity equals the relative velocity (W) and the area equals the area of the rotor blades. Eq. (16) can then be written for the elemental sector considered previously:

$$dT = (C_L \cos \beta - C_D \sin \beta)(\rho/2) W^2 bcdr \quad (17)$$

where b equals the number of rotor blades used. From Fig. 2 it can be seen that

$$W = [v + (v'/2)]/ \sin \beta \quad (18)$$

Substituting this value in Eq. (17) and rearranging the equation to solve for dT/dr results in

$$\frac{dT}{dr} = (C_L \cos \beta - C_D \sin \beta) \left(\frac{\rho}{2}\right) \left[\frac{v + (v'/2)}{\sin \beta}\right]^2 bc \quad (19)$$

Eqs. (19) and (14) both give values for dT/dr and can therefore be equated:

$$2\pi r(2vv' + v'^2) = (C_L \cos \beta - C_D \sin \beta) \left[\frac{v + (v'/2)}{\sin \beta}\right]^2 bc \quad (20)$$

Since $C_D/C_L = K$ or $C_D = KC_L$, Eq. (20) can be rewritten so that

$$2\pi r(2vv' + v'^2) = C_L(\cos \beta - K \sin \beta) \left[\frac{v + (v'/2)}{\sin \beta}\right]^2 bc \quad (21)$$

Solving Eq. (21),

$$\frac{C_L bc}{r} = \frac{2\pi(2vv' + v'^2)}{(\cot \beta - K)[(2v + v')^2/4 \sin \beta]} \quad (22)$$

This can then be put into the simpler form:

$$\frac{C_L bc}{r} = \frac{8\pi \sin \beta}{(\cot \beta - K)[2(v/v') + 1]} \quad (23)$$

which is the final design formula.

Condition of Hovering Flight

Now that the design Eq. (23) is available, apply it to the simplest condition, hovering flight, where the axial velocity of the rotor blade is $v = 0$. The rotational induced velocity u' from Eq. (11) becomes

$$u' = u\{1 - \sqrt{1 - [(v'^2 + 2Kv'u)/u^2]}\} \quad (24)$$

and the tan β from Eq. (2) becomes

$$\tan \beta = \frac{v'/2}{u - \frac{u}{2}\left[1 - \sqrt{1 - \frac{v'^2 + 2Kv'u}{u^2}}\right]} \quad (25)$$

The new equation for the relative velocity W becomes

$$W = \sqrt{\left(\frac{v'}{2}\right)^2 + \left[u - \frac{u}{2}\left(1 - \sqrt{1 - \frac{v'^2 + 2Kv'u}{u^2}}\right)\right]^2} \quad (26)$$

from the original equation taken from Fig. 2, where

$$W = \sqrt{[v + (v'/2)]^2 + [u - (u'/2)]^2} \quad (27)$$

The sin β, which becomes

$$\sin \beta = \frac{v'/2}{\sqrt{\left(\frac{v'}{2}\right)^2 + \left[u - \frac{u}{2}\left(1 - \sqrt{1 - \frac{v'^2 + 2Kv'u}{u^2}}\right)\right]^2}} \quad (28)$$

can be simplified to the following form:

$$\sin \beta = v'/\sqrt{2u^2 + 2u(\sqrt{u^2 - v'^2 - 2Kv'u} - Kv')} \quad (29)$$

Now that $v = 0$, the new design formula, Eq. (23), becomes

$$C_L bc/r = 8\pi \sin \beta/(\cot \beta - K) \quad (30)$$

Substituting both Eqs. (29) and (25) in Eq. (30) results in

$$\frac{C_L bc}{r} = \frac{8\pi\left[\frac{v'}{\sqrt{2u(u + \sqrt{u^2 - v'^2 - 2Kv'u} - Kv')}}\right]}{[(u + \sqrt{u^2 - v'^2 - 2Kv'u})/v'] - K} \quad (31)$$

This equation can be simplified by collecting terms to

$$\frac{C_L bc}{r} = \frac{8\pi v'^2}{(\sqrt{2u})(u - Kv' + \sqrt{u^2 - v'^2 - 2Kv'u})^{3/2}} \quad (32)$$

By dividing the numerator and denominator by u^2,

$$\frac{C_L bc}{r} = \frac{8\pi(v'/u)^2}{\sqrt{2}\,[1 - K(v'/u) + \sqrt{1 - 2K(v'/u) - v'^2/u^2}]^{3/2}} \quad (33)$$

Since the ratio, v'/u appears so often, let it be called P, and the design Eq. (33) for hovering flight becomes

$$\frac{C_L bc}{r} = \frac{17.77P^2}{(1 - KP + \sqrt{1 - 2KP - P^2})^{3/2}} \quad (34)$$

All the equations have now been derived whereby one can obtain the design condition for hovering flight. If the weight to be lifted is W_0, then a dW can be assigned to each dr of the blade and replaced for dT in Eq. (14). If v is zero, as it is in hovering flight, then this equation becomes

$$dW_0/dr = \pi r \rho v'^2 \quad (35)$$

and if a value is assigned to dW_0/dr, v' can be determined at any given radius. If the distribution of the induced velocity is uniform over the rotor disc, Eq. (35) can be written in the integral form and solved:

$$W_0 = \pi \rho v'^2 \int_0^R r\,dr \quad (36)$$

$$W_0 = \pi \rho v'^2 (R^2/2), \quad (37)$$

or

$$v' = \sqrt{2W_0/\pi\rho R^2} \quad (38)$$

$$v' = (1/R)\sqrt{2W_0/\pi\rho} \quad (39)$$

This equation gives an average v' for the entire disc.

However, it is impossible to make v' constant throughout the disc, since, if it were, the value P, (v'/u), would become extremely large near the center of the rotor. By examination of Eq. (34), it is clear that P can never be over 1, since, if it were, the value under the radical sign would be negative and no design coefficient $C_L bc/r$ could be obtained. It is therefore apparent that in the actual design v' will probably decrease as r approaches the center of the rotor.

If a rotor loading is assumed in which the load is uniform throughout the disc—that is, that each dr carries the same weight—then the induced velocity for any section dr between R_2 and R_1 would be

$$W_0 = \int_{R_1}^{R_2} \pi r \rho v'^2\,dr \quad (40)$$

or

$$v' = \left(\frac{2W_0}{\pi\rho}\right)\left(\frac{1}{\sqrt{R_2^2 - R_1^2}}\right) \quad (41)$$

Since $\sqrt{2W_0/\pi\rho}$ is a constant, v' just varies with the reciprocal of $\sqrt{R_2^2 - R_1^2}$. As the values of R_2 and R_1 approach the center, this radical would decrease in value, while the values for v' would again increase. This also proves to be the wrong system of loading, since no blade could be designed to furnish the relatively high values of v' occurring.

Assume then a v' that is proportional to r, say fr. If this value is now substituted for v' in the equation $p = v'/u$ and if u is given the value $2\pi rn$, then

$$P = fr/2\pi rn \text{ or } f/2\pi n \quad (42)$$

which is a constant for any r. Substituting this new value for P in Eq. (34) gives $C_L bc/r$ as a constant also. This means that if the C_L does not vary through the span of the rotor blade, then the chord C of the blade will increase with the radius r. This would indicate a blade narrow at the root and wide at the tip. Aerodynamically, the blade design is now possible, but, structurally, it does not appear to be plausible. Either a different induced velocity distribution is necessary, or the C_L value will also have to change along the span.

Use of Charts

So as to determine the theoretical velocity distribution underneath the rotor blade in hovering flight, three curves, Figs. 3, 4, and 5, are used. They are, namely, a graph of the rotor blade characteristics; a graph of the value $C_L bc/r$ vs. P; and a graph of β vs. P. To illustrate the use of these graphs, a particular case is chosen and the theoretical distribution is determined.

Assume a 4-ft. diameter rotor with three blades of 2-in. constant chord, each rotating at 450 r.p.m. Let the blade itself have a 10° twist, the tip section being set at 10° with respect to the horizontal plane and the root being 20°. Use as blade section an NACA 0015 Airfoil. Sections along the span 4 in. apart will be chosen so that those to be considered are at r = 0, 4, 8, 12, 16, 20, and 24 in., respectively. Choosing the section at r = 12 in. as an example, the procedure for determining the values v' and u' at that point are as follows:

Since it is not known just what C_L exists at r = 12 in., three assumptions could be made and the actual point found by plotting these values on Fig. 6. Values of C_L = 0.85, 0.51, and 0.27, were arbitrarily chosen. If C_L were 0.51 from Fig. 3, the angle α_0 would have to be 7° and the L/D would have to be 20. Since the blade has a 10° twist and is set at 20° at the root, the angle $(\beta + \alpha_0)$ at r = 12 in. would be 15°. This would therefore mean that β must be 8°. From Fig. 5, if β were 8° and the L/D ratio were 20, then P would necessarily be 0.272. However, the $C_L bc/r$ value with C_L as 0.51 at a radius r = 12 is equal to 0.255. From Fig. 4 this gave P equal to 0.199. These points were then plotted on Fig. 6, and the same procedure was followed through for C_L = 0.85 and 0.27. By this method, it was determined that P = 0.218 at r = 12. If the rotor is operating at 450 r.p.m., then the tangential velocity (u) of the blade section considered is equal to $2\pi rn$ or 47.1 ft. per sec. P was defined as v'/u, so v' is equal to Pu or 0.218 × 47.1 = 10.27 ft. per sec. This value was plotted on Fig. 8 as the value of the axial velocity. In a similar manner the other values of v' were determined and the entire curve was plotted.

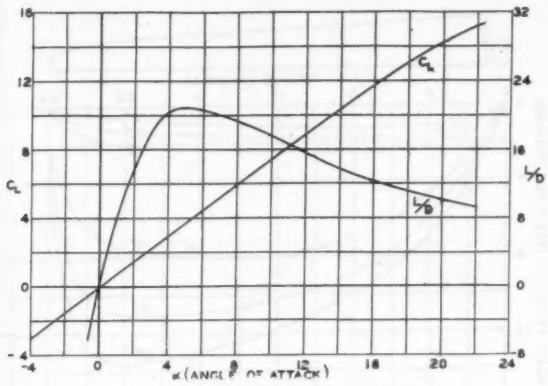

FIG. 3. NACA 0015 airfoil characteristics.

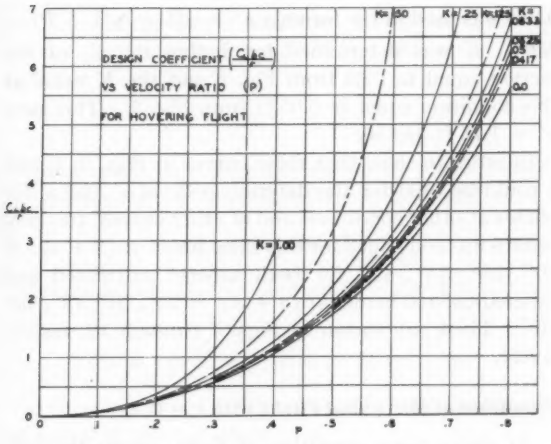

FIG. 4. Design chart for various drag/lift ratios.

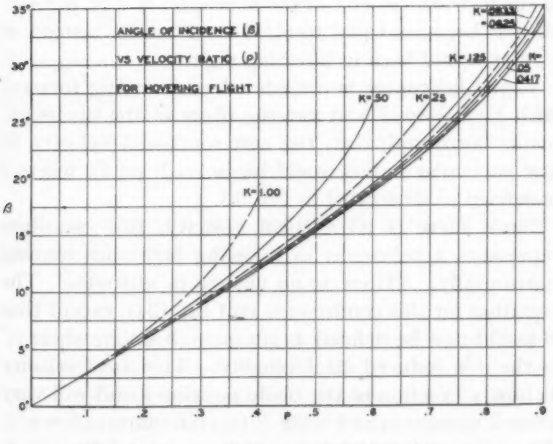

FIG. 5. Incidence chart for various drag/lift ratios.

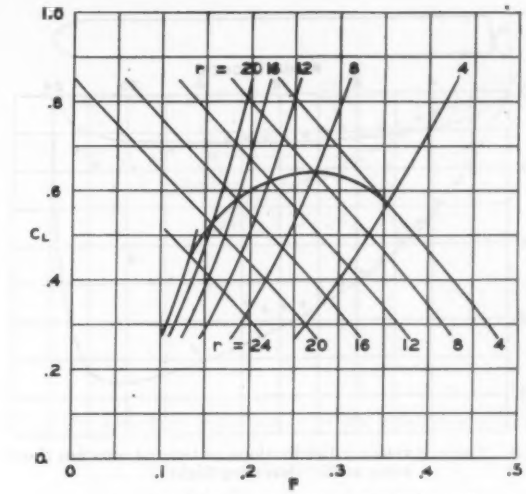

FIG. 6. Graphic determination of velocity ratio.

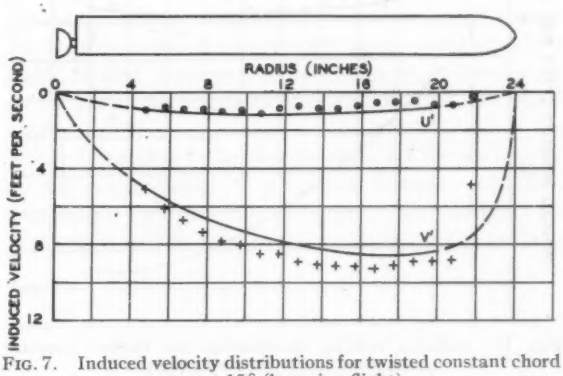

FIG. 7. Induced velocity distributions for twisted constant chord rotor at 15° (hovering flight).

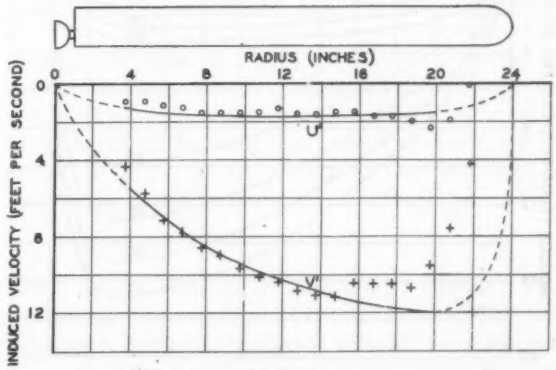

FIG. 8. Induced velocity distributions for twisted constant chord rotor at 20° (hovering flight).

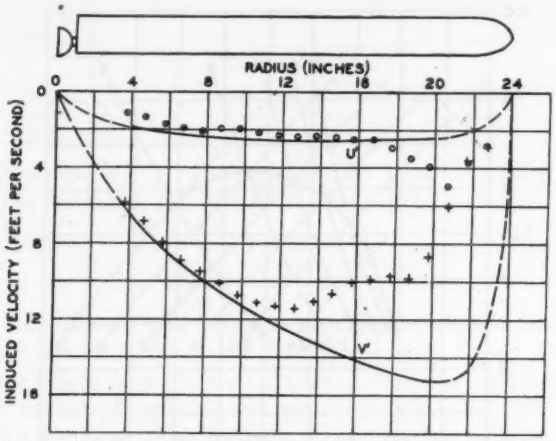

FIG. 9. Induced velocity distributions for twisted constant chord rotor at 25° (hovering flight).

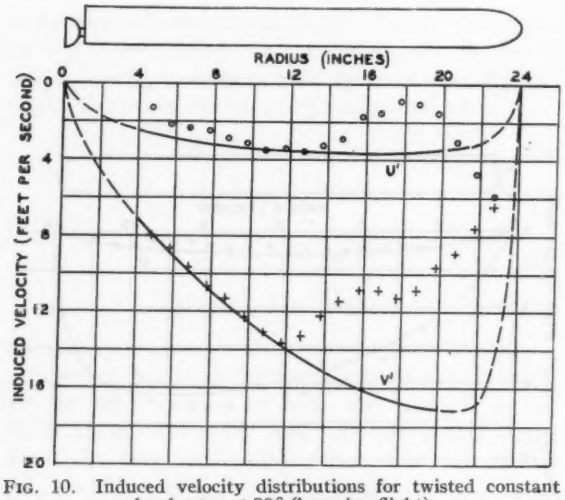

FIG. 10. Induced velocity distributions for twisted constant chord rotor at 30° (hovering flight).

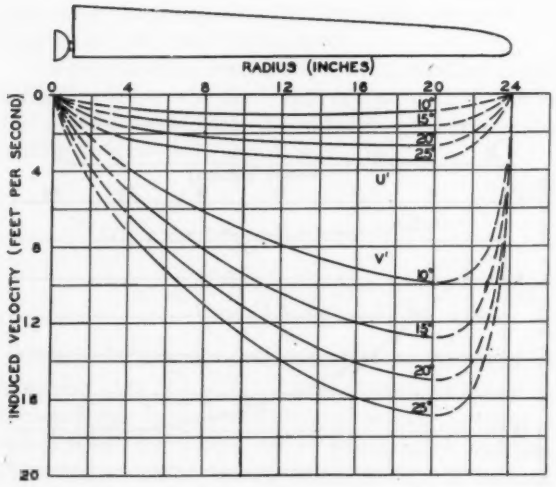

FIG. 11. Induced velocity distributions for nontwisted, tapered-chord rotors.

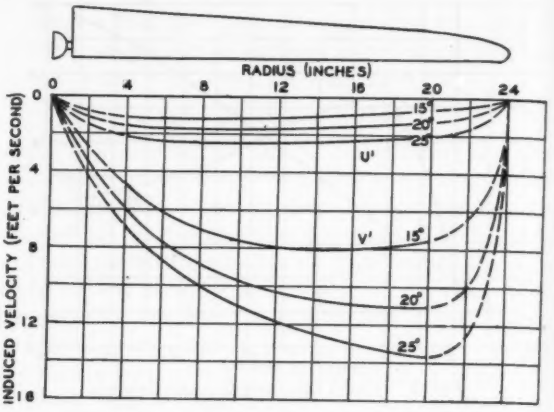

FIG. 12. Induced velocity distributions for twisted, tapered-chord rotors.

To determine the magnitude of u' the value of $P = 0.218$ was used in the formula $u' = u[1 - \sqrt{1 - P^2 - KP}]$. K was determined by finding the C_L of the section equal to 0.62 from Fig. 6 and the K value at this condition equal to 0.0532 from Fig. 3. This gave $u' = 1.75$ ft. per sec.

In order to show that these curves in Figs. 3, 4, and 5 could be used for the determination of v' and u' for blades at other conditions and of other shapes, this procedure was continued for this same blade at $(\beta + \alpha_0) = 30°$, 25°, 15°, and for both tapered untwisted and tapered twisted blades at $(\beta + \alpha_0) = 25°$, 20°, 15°, and 10°. These are shown in Figs. 7 through 12, respectively.

Condition of Horizontal Flight with v = 0

At the extreme condition of flight, where the helicopter is moving forward and the plane of the rotor remains horizontal, the value of v' and u' varies with the blade position as well as along the radius.[3] However, the same values of P as those in hovering flight are still valid, except that they are now defined differently. If the forward velocity of the helicopter is Y ft. per sec. then P becomes equal to $v'/(u - Y \sin \theta)$, instead of v'/u as it had been in hovering flight.

If the helicopter is considered as traveling forward with a velocity Y and yet the plane of the blades remains horizontal, then the new rotational velocity at any particular radius would be $(u - Y \sin \theta)$, where θ is defined as illustrated in Fig. 13.

Since there is no vertical velocity, this condition represents a helicopter in hovering flight but moving horizontally. (There is no change in altitude.) The equation for this condition is still Eq. (34), except that p would now be defined as $v_1'/(u - Y \sin \theta)$, where v_1' is the new induced axial velocity. This axial velocity is now a function of the blade position θ and will vary from a maximum at $\theta = 3\pi/2$ to a minimum at $\theta = \pi/2$. This means that if p is found by means of Figs. 3, 4,

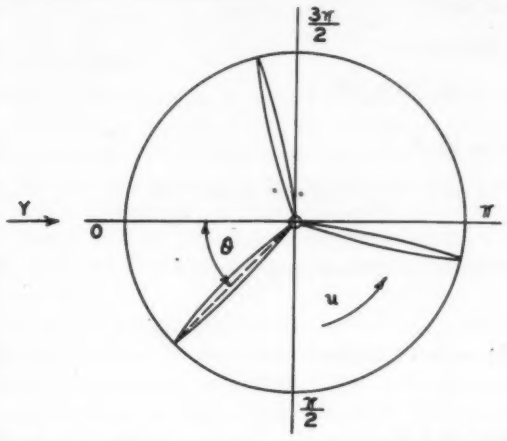

FIG. 13. Top view of rotor disc in horizontal hovering flight.

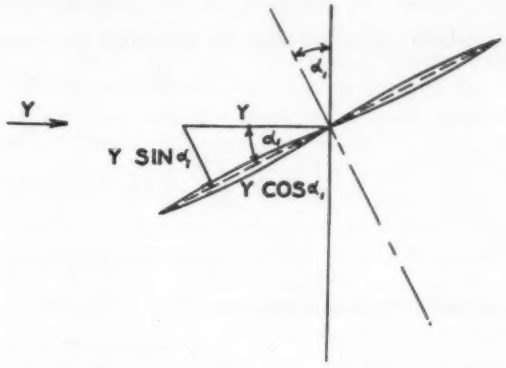

FIG. 14. Side view of inclined rotor disc in horizontal flight.

and 5 for the hovering condition, then this value of p for any particular radius r could be used in the determination of the new v_1':

$$v_1' = p(u - Y \sin \theta) \tag{43}$$

Considering now a small section of rotor span dr and solving for the lift produced by it, it is found that

$$dL/dr = \rho r d\theta (v_1'^2/2) \tag{44}$$

This comes from the momentum formula, which states that

$$\text{lift} = (\text{mass/sec.})(\text{change in velocity})$$

If it is desired to find the entire lift produced by this section dr at radius r, then

$$\frac{dL}{dr} = \frac{p^2 r \rho}{2} \int_0^{2\pi} (u - Y \sin \theta)^2 d\theta \tag{45}$$

or

$$\frac{dL}{dr} = \frac{p^2 r \rho}{2} \int_0^{2\pi} (u^2 - 2uY \sin \theta + Y^2 \sin^2 \theta) d\theta \tag{46}$$

This gives

$$\frac{dL}{dr} = \frac{p^2 r \rho}{2} \left[u^2 \theta + 2uY \cos \theta + Y^2 \left(\frac{\theta}{2} - \frac{\sin 2\theta}{4} \right) \right]_0^{2\pi} \tag{47}$$

$$dL/dr = (p^2 r \rho/2)(2\pi u^2 + Y^2 \pi) \tag{48}$$

If the helicopter were not moving horizontally, then this equation would read

$$dL/dr = (p^2 r \rho/2) 2\pi u^2 \tag{49}$$

This formula therefore shows an increase of lift for the section considered equal to $(p^2 r \rho/2)(Y^2 \pi)$. This increase of lift, of course, was based on the assumption that the rotor blades would continue to rotate at the same speed as they had been in hovering flight. The amount of torque required for a similar section should therefore be examined for both hovering and horizontal flight, as just described, to determine what increase of power would be required to maintain this rotational speed.

The formula for the torque required for section dr at radius r is similar to the thrust formula, Eq. (48), except that the value p is replaced by K_1, which equals $(1 - \sqrt{1 - p^2 - 2Kp})$, and a distance factor (r) is added.

$$dQ/dr = (K_1 p \rho r^2/2)(2\pi u^2 + Y^2 \pi) \tag{50}$$

represents the condition of hovering forward flight, while

$$dQ/dr = (K_1 p \rho r^2/2) 2\pi u^2 \tag{51}$$

represents the condition for still hovering flight. $(K_1 p \rho r^2/2) Y^2 \pi$, the difference between these two values, is the increase of torque required for a horizontal movement of the blades at a velocity Y over the torque required for plain hovering flight for the same rotor speed. Therefore, although a gain of lift of $(p^2 \rho r/2) \times (Y^2 \pi)$ is felt during this horizontal movement, an increase of torque of $K_1 p \rho r^2 (Y^2 \pi)/2$ was necessary in order to produce this result.

In normal horizontal flight the axis of the helicopter rotor is usually tilted in the direction of motion. This causes a component of the total lifting force of the rotor to be directed horizontally and enables horizontal motion without the need of auxiliary rotors. This type of flight condition can be investigated with the formulas just completed. From Fig. 14 it can be seen that velocity v now equals $Y \sin \alpha_1$ and is the same throughout the disc. The new rotational velocity is equal to $u_2 = Y_2 \sin \theta$, where $Y_2 = Y \cos \alpha_1$. Therefore,

$$u_2 = u - Y \cos \alpha_1 \sin \theta \tag{52}$$

The thrust of the rotor then can be written for a section dr at distance r:

$$dT/dr = \rho r \int_0^{2\pi} [Y \sin \alpha_1 + (v_2'/2)]v_2' \, d\theta \tag{53}$$

where

$$v_2' = P(u - Y \cos \alpha_1 \sin \theta) \tag{54}$$

$$\frac{dT}{dr} = \rho r \int_0^{2\pi} \{Y \sin \alpha_1 + [P(u - Y \cos \alpha_1 \sin \theta)/2]\}[P(uY \cos \alpha_1 \sin \theta)]d\theta \tag{55}$$

or

$$dT/dr = \rho r P \pi [2Yu \sin \alpha_1 + (P/2)(2u^2 + Y^2 \cos^2 \alpha_1)] \tag{56}$$

In order to check this equation, let $Y = 0$; then

$$dT/dr = \rho r P[+ (P/2)(2\pi u^2)] = (\rho r P^2/2)(2\pi u^2) \tag{57}$$

which is the same as Eq. (49). Then let $\alpha_1 = 0$ and

$$dT/dr = (\rho r P^2/2)(2\pi u^2 + Y^2 \pi) \tag{58}$$

which is the same as Eq. (48).

The lift of the rotor blade for the section considered now decreases according to the angle α_1.

$$dL/dr = (dT/dr) \cos \alpha_1 \tag{59}$$

The remainder, $(dT/dr) \sin \alpha_1$, goes into the forward thrust of the rotors. The forward thrust equation for the rotor at section (r, dr) is

$$(dT/dr) \sin \alpha_1 = \rho r P \pi \sin \alpha_1 [2Yu \sin \alpha_1 + (P/2)\ (2u^2 + Y^2 \cos^2 \alpha_1)] \tag{60}$$

In this equation all the values are known except P, and that can be obtained from the charts on either hovering or vertical flight conditions. These values may then be summed up for all the dr's and the total forward thrust obtained.

Condition of Vertical Flight

Previously, the specific case of hovering flight was considered, but the formulas developed for that condition did not take into account what would happen in the event the ship would rise or descend. Eq. (23) is a general equation for any condition and can be solved provided the terms in it can be determined. This was done in Eq. (34) for hovering flight but becomes a little more complicated for vertical flight.

If the vertical velocity is equal to v as defined in Fig. 3, then,

$$\sin \beta = \frac{v + (v'/2)}{W} = \frac{(v + v'/2)}{\sqrt{(v + v'/2)^2 + (u - u'/2)^2}} \tag{61}$$

The term u' can be defined by Eq. (11) and substituted in Eq. (61) to give

$$\sin^2 \beta = \frac{1}{1 + \dfrac{1}{(2v + v')^2}\left[2u - (u - vK)\left(1 - \sqrt{1 - \dfrac{v'^2 + 2vv' + 2Kv'u}{(u - vK)^2}}\right)\right]^2} \tag{62}$$

In the same manner, the cot β can be found to be

$$\cot \beta = \left\{u - \left(\frac{u - vK}{2}\right)\left[1 - \sqrt{1 - \frac{v'^2 + 2vv' + 2Kv'u}{(u - vK)^2}}\right]\right\} / [v + (v'/2)] \tag{63}$$

These terms, as defined in Eqs. (62) and (63) can be substituted in the general Eq. (23) to give the solution desired. Through simplification, this equation can be put into another form. By dividing both the numerator and denominator by u^2 and letting $v'/u = P$ and $v/u = s$, the equation becomes

$$\frac{C_L bc}{r} = \frac{8\pi PM}{\sqrt{M^2 + [2 - N(1 - L_1)]^2}\,[N(1 + L_1) - KP]} \tag{64}$$

where $M = (2s + P)$, $N = (1 - Ks)$ and $L_1 = \sqrt{1 - [(P^2 + 2sP + 2KP)/(1 - Ks)^2]}$.

This Eq. (64) is now in a form that is general enough to be applied easily to either hovering, vertical, or horizontal flight.

Results

Hovering Flight

By employing Figs. 3, 4, and 5, the theoretical induced velocity distribution of three types of blades at various angles of incidence were calculated and plotted by the means described in the section on the "Use of Charts." The results of these calculations were plotted in Figs. 7 through 12 and show the relative values that can be expected when the various shapes and settings are used.

As would be expected, the curves show that there is a gradual decrease in the induced velocity as the blade angle of incidence is decreased. This amount is most easily observed in Figs. 11 and 12, where the group of blades are plotted together. By comparing the curves of the 20° blade settings, it appears that the twisted blades have the more even distribution. The tapered blade, which is not twisted, carries an even greater load toward the tip than the constant chord blade. The two twisted blades have a similar distribution, the tapered blade being a little more evenly loaded than the other. This tends to indicate that the tapered twisted blade would probably be the best of the group structurally, while the constant chord blades, being simpler to construct, are a close approximation.

The induced velocities of the constant chord rotors were measured in the wind tunnel by means of the "hot wire" units discussed earlier, and the experimental points obtained were plotted on Figs. 7–10. The experimental values for the 15° and 20° blade settings are fairly close to those predicted by the theoretical curves. However, as the angle of incidence of the blade is increased, the relationship between experimental and predicted values becomes less apparent, especially toward the tip. Since no tip correction was incorporated in the theoretical curves, it was to be expected that a discrepancy would appear. However, the breakdown of the induced velocity distribution does not localize itself to the tip but starts about at the center of the blade. By comparing the four constant chord blade curves, it appears that this breakdown acts almost as an ordinary stall but settles down to practically the same values for the three highest angle settings.

The measured rotational induced velocities were fairly close to the predicted values in those regions where the axial induced velocities checked. Near the tip, however, where the measured axial velocities began to decrease, the rotational measurements showed a slight increase. This indicates that the air has begun to follow the blade around as if it were a paddle instead of a propeller and is an evidence of wasted power.

Accuracy of Measurements

The velocities close to the hub were not taken because the equipment was set to measure only velocities above a certain base value. As was explained earlier in the discussion on the apparatus, this enabled more accurate readings of the velocities that were taken. The tip velocities also tended to zero and were omitted either because they were too low or because the turbulence in that region was too great to be assigned a constant value. The remainder of the velocities were measured to within an accuracy of about 1 per cent. This figure is an estimate, since it depends mainly on the ability to read the record and get a good average value for the velocity indicated. The actual velocity records, however, oscillated some 2 mm. out of 180, necessitating the use of an average value. The wind-tunnel air, when not disturbed by the rotor blades, would record as a straight line, the fluctuations in it being too fast and too small for the Esterline Angus meter to follow. The higher velocities under the rotor, therefore, could easily be measured with a better than 1 per cent accuracy.

The angle measurement, which was also taken, presupposes that there is not much radial velocity present and that the majority of the air is traveling in a plane perpendicular to the radius. The V-wire, therefore, measures the angle in that plane, and the velocity wire measures the velocity in that plane. On the whole, this assumption of low radial velocities is valid for the rotational velocity used and was checked by making a survey with the "hot wire" probe along that radius which would cause the V-wire to lie in a plane made up of the axis of the rotor and the radius.

Horizontal Flight

One rotor arrangement was chosen to be investigated thoroughly, and it consisted of the three constant chord blades set at 20° with respect to the rotor disc at the hub. With these blades revolving at 450 r.p.m. and inclined in the wind tunnel so that the plane of the disc was parallel to the air stream, several surveys were made under the rotor at various wind-tunnel velocities. Both average velocity surveys and instantaneous records were taken at positions that would be equivalent to $\theta = \pi/2$ and $\theta = 3\pi/2$. These are the positions of maximum and minimum effectiveness and would be representative of the range of velocities to be encountered. At $\theta = \pi/2$ the blades were traveling in the direction of the wind-tunnel airflow, and at $\theta = 3\pi/2$ they were traveling opposite to this flow. Since these blades were held rigidly at the hub, they passed through a region of high lift and high torque at $\theta = 3\pi/2$ and of low lift and low torque 180° from this position.

The average velocity records were taken at 2-in. intervals from about $r = 4$ to 34 in. because there seemed to be an interesting reversal of flow past the tip of the blades. The plain velocity readings did not indicate anything particular, but the direction of flow changed so much that attention was drawn to this region from the tip outward.

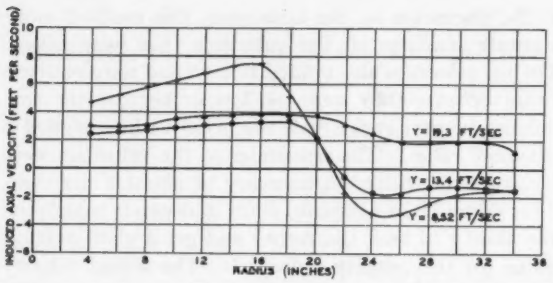

FIG. 15. Induced axial velocity vs. radius for horizontal and hovering flight at $\theta = \pi/2$.

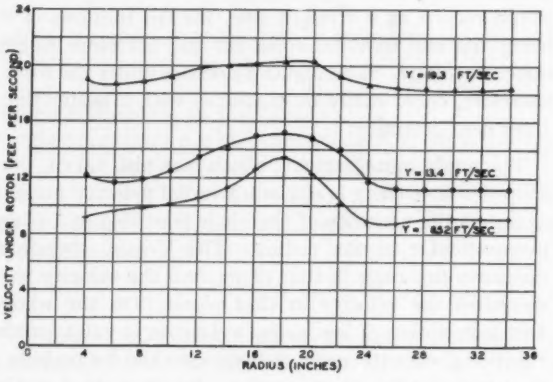

FIG. 16. Velocity under rotor vs. radius for horizontal flight at $\theta = \pi/2$.

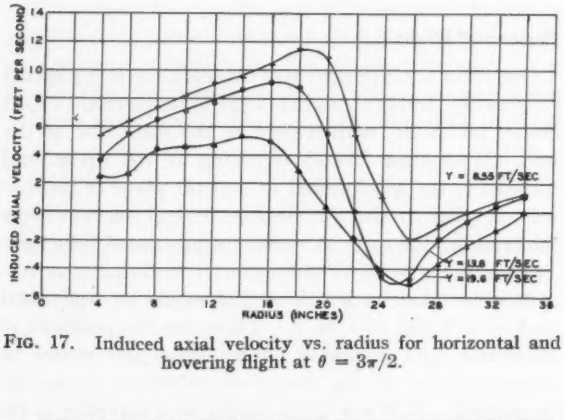

FIG. 17. Induced axial velocity vs. radius for horizontal and hovering flight at $\theta = 3\pi/2$.

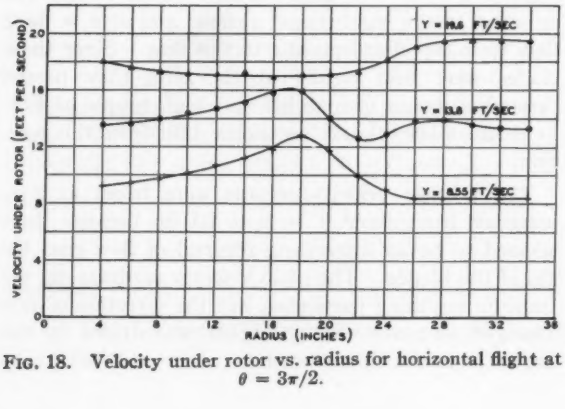

FIG. 18. Velocity under rotor vs. radius for horizontal flight at $\theta = 3\pi/2$.

From Fig. 15 it can be seen that there is a reversal of axial flow from about $r = 22$ in. outward for the 8.52 and 13.4 ft. per sec. runs. The 19.3 ft. per sec. run does not show this negative v', and this seems to follow the trend set by the 13.4 ft. per sec. run, which shows a decrease over the slower velocity. Although an axial velocity is indicated past the blade tip, not too much emphasis should be placed on it, since it was difficult to obtain accurate angle readings in this region of disturbed airflow. These measurements were also taken close to the edge of the tunnel, and, although qualitatively they are probably valid, the actual values obtained are less accurate than the rest.

Theoretically, the axial flow immediately under the rotor for the 19.3 ft. per sec. run should be the lowest, and then it should increase as the horizontal velocity decreases. The 8.52 ft. per sec. run follows this trend as compared to the other two, but the 19.3 ft. per sec. run shows about the same axial induced velocity as the 13.4 ft. per sec. run. It seems that the horizontal airflow is great enough to disrupt this tendency even at 2 in. below the blades. (This is evidenced again at $\theta = 3\pi/2$, as will be explained later.)

Fig. 16, from which the axial induced velocities were taken, shows the maximum effectiveness of the blade to be at about 18 in. out from the center or at about 75 per cent of the radius. There is a gradual rise in induced velocity up to this peak and then a decline. The percentage of increase becomes less as the horizontal velocity increases.

At $\theta = 3\pi/2$ the effectiveness of the blade should be just opposite to that just discussed. The forces on the blade here are increased by the horizontal airflow, and this increase is supposed to be great enough to not only offset the opposite side but to cause the overall effectiveness of the rotor to increase. This is evidenced by both the force tests and the theory. At all three wind-tunnel velocities a reversal of flow is caused at the tip, the values of the 13.8 ft. per sec. velocities shifting between the other two. Although theoretically the induced axial velocities should increase with the horizontal velocity, Fig. 17 shows a decrease. The worst curve (19.6 ft. per sec.) could be explained from the fact that the blade is evidently stalled. This is indicated by Fig. 18, which shows the gradual increase of effectiveness along the radius for the 13.8 and 8.55 ft. per sec. runs but shows no such increase for the other. The 19.6 ft. per sec. run indicated a near stalled condition, because at times it gave velocity readings that varied considerably. The low readings plotted were the most consistent.

These velocities discussed so far have been average values taken under the blades at the positions indicated. They ranged from the lowest expected values to the highest. Since the force on the blade is a function of v' and since v' has been shown to be greatest at $\theta = 3\pi/2$ for any horizontal velocity tried, this fact checks

with the theory that predicts this effect. However, this theory also only considers an average velocity, and it is known that the velocity is not steady, but pulsating, because the blades do not form a solid disc. Therefore, instantaneous velocity tests were made to try to determine the magnitude of these variations.

Instantaneous Velocities

Three radial positions at $r = 12$, 17, and 21 in. were chosen, and instantaneous velocity records were made at $\theta = \pi/2$ and $3\pi/2$. Several check points were also made at $\theta = 0$. Several sample records of these runs are shown in Fig. 19, the thin horizontal reference line through each photograph representing a 15 ft. per sec. velocity. These records show the entire velocity under the rotor blades, not just the axial induced velocities. Such records were made because no means of determining the instantaneous angle was provided. The timing wave is 60 cycles per sec., and the blade impulses are 22.5 per sec. Therefore, each blade takes up approximately three timing wave cycles.

From these records the impulses were not only discovered to be large, but it was found that the low velocity values of the waves actually went below the horizontal velocity value in almost all instances. At $\theta = \pi/2$ and with the horizontal velocity at 13.4 ft. per sec., the percentage of velocity change based on the horizontal velocity was at $r = 21$, 17, and 12 in., respectively; 23.1, 21.6, and 30.2 per cent. At $Y = 19.3$, the percentages are 13.2, 19.3, and 22 per cent, respectively. At $\theta = 3\pi/2$ and with the horizontal velocity at 13.8 ft. per sec., the percentage change for each similar station is 43.1, 34.4, and 36.9 per cent. For $Y = 19.6$ ft. per sec., these values are 19.1, 27.5, and 33.7 per cent, respectively. These values show that the impulses are greatest at $\theta = 3\pi/2$ where the total force is also greatest. They also show that the increase of horizontal velocity causes a definite decrease in the percentage change, even though some of the actual amounts of velocity change are greater for the higher horizontal velocity.

A close examination of these records showed that at $\theta = 3\pi/2$, where the impulses are the greatest, the impulse builds up gradually and drops off sharply at $r = 12$ in.; it builds up and drops off at about the same rate at $r = 17$ in.; and it has an extremely erratic behavior at $r = 21$ in. This is true for both the 13.8 and 19.6 ft. per sec. runs. At $\theta = \pi/2$ no definite impulses like those exhibited on the opposite sides were present. In all cases the average velocity measured previously with the direction-velocity "hot wire" was between the maximum and minimum values obtained by the instantaneous wire.

From this investigation it has been shown that although the basic theory could be applied to plain hovering flight, where the design method introduced here proves fairly satisfactory, there is much about the flow under the rotor during horizontal flight which this theory does not include. Such effects as the apparent loss of v' at high horizontal velocities would reduce the possibilities of obtaining stability by down-wash from the rotors. The stalling of the rotor blades during part of the cycles and the reversed flow beyond the tips during horizontal flight are two more factors not shown in the theory. However, perhaps the most startling find is in the instantaneous velocity changes. Although it was well understood that impulses were to be expected, it is doubtful that the percentages obtained by these tests were anticipated. Not only were they much greater than seemed evident at first, but the fact that they actually went into the negative region, with respect to the horizontal flow, shows the possibility of greater vibration effects and the need for extra stress consideration.

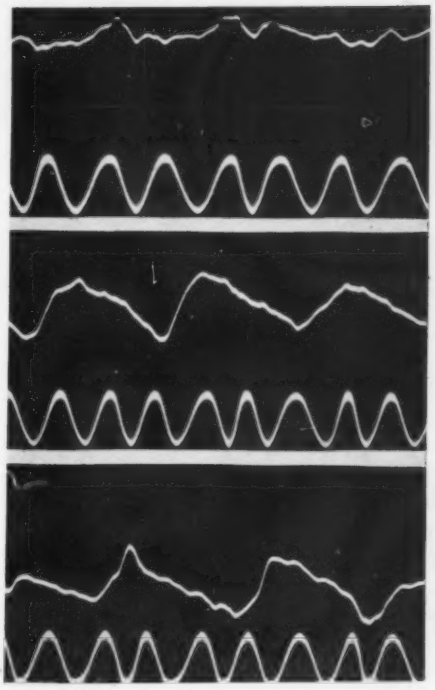

FIG. 19a (*top*). $\theta = \pi/2$; $v = 19.3$ ft. per sec.; $r = 12$ in. Fig. 19b (*center*). $\theta = 0$; $v = 13.8$ ft. per sec.; $r = 8$ in. Fig. 19c (*bottom*). $\theta = 3\pi/2$; $v = 13.8$ ft. per sec.; $r = 12$ in.

REFERENCES

[1] Famé, Lieutenant Colonel, *Le Vol. Vertical*, 1st Ed., p. 9; Ed. Blondel La Rougery, Paris, 1934.

[2] Durand, W. F., *Aerodynamic Theory*, 1st Ed., Vol. IV, p. 230; Julius Springer, Berlin, 1935.

[3] Glauert, H., *Horizontal Flight of a Helicopter*, Tech. Report A. R. C., R. & M. No. 1157, Vol. I, p. 612, March, 1928.

The Column Paradox

F. R. SHANLEY*

Lockheed Aircraft Corporation

Since this article was received, the author has informed us that he has worked out the equilibrium equation for a simplified, two-flange column. The column starts to bend at the tangent modulus load and the load increases with increasing lateral deflection. If the tangent modulus is assumed to be constant, the column load is asymptotic to the value predicted by the reduced modulus theory. This development will be covered by a second paper, now in preparation.—EDITOR.

INTRODUCTION

As SHOWN BY VON KÁRMÁN in his classical paper,[1] column action in the inelastic range (beyond the proportional limit) involves two different moduli of elasticity: the elastic (Young's) modulus, and the tangent modulus (local slope of stress-strain diagram). The "reduced modulus" is a function of both of these and is also affected by the shape of the cross section. By using the reduced modulus in place of Young's modulus, Euler's equation has been generalized to include stresses well beyond the elastic limit.

REDUCED MODULUS THEORY

If the tangent modulus is used directly in the Euler formula, the resulting critical load is somewhat lower than that given by the reduced modulus theory. This simpler formula, originally proposed by Engesser, is now widely used by engineers, since it gives values that agree very well with test data. Nevertheless, the reduced modulus formula is still generally considered to be the true theoretical solution for perfect columns, and the lower test values are explained by references to unavoidable eccentricities, testing technique, and other errors.

The reduced modulus theory is derived by assuming that, *after* the column reaches the critical uniform stress, the column bends. This causes the strain to decrease on one side and increase on the other. For the increasing strains the resulting stresses are given by the tangent modulus, while for the decreasing strains the elastic modulus gives the relation between strain and stress. Tests have shown that, *when the strain reverses*, actual conditions are in accordance with this theory.

DISCUSSION

But there is an implied assumption in the derivation of the reduced modulus theory that is open to question. It is, in effect, assumed that something keeps the column straight while the strain increases from that predicted by the tangent modulus theory to the higher value derived from the reduced modulus theory. Actually, there is nothing (except the column's bending stiffness) to prevent the column from bending *simultaneously* with increasing axial loading. Under such conditions the compressive strain could increase on one edge of the column while remaining constant on the other, or it could increase at a different rate on opposite edges. If such action were assumed, the tangent modulus would apply over the entire cross section, and the theoretical buckling load would be that predicted by the tangent modulus theory. This creates a paradox, because, if all of the strains equal or exceed the tangent modulus value, the average strain will be *greater* than that predicted by the tangent modulus theory.

The assumptions involved in the reduced modulus theory also represent a paradox. The theory predicts that the column will remain straight up to the calculated maximum load, but it also shows that some strain reversal is needed in order to provide the additional column stiffness required beyond the tangent modulus load. It is impossible to have strain reversal in a straight column.

Evidently, the maximum column load will be reached somewhere between the loads predicted by the two theories. The entire problem should be reviewed on the basis that axial loading and bending can occur *simultaneously*. The use of the principle of superposition is not valid in this case.

CONCLUSIONS

Since it will require some reversal of strain in order to exceed the tangent modulus load, it can be predicted that bending will begin as soon as that load is exceeded. The tangent modulus theory can therefore be regarded as correct for predicting the maximum axial load at which a perfect centrally loaded column will remain straight.

To find the maximum load for a perfect column in the plastic range, it will evidently be necessary to analyze each case separately, using a step-by-step process and employing the general methods followed by von Kármán in his solution of the eccentric column.

Received August 23, 1946.

* Division Engineer in Charge of Engineering Research.

REFERENCE

[1] Forschungsarbeiten, No. 81, 1910, Berlin; see any modern textbook on advanced structures.

105164
TL
501
.I 522
V.13
1946

Index to Volume 13

Journal of the Aeronautical Sciences

Numbers 1–12, January–December, 1946

No. 1, January, 1946, pages 1– 48
No. 2, February, 1946, pages 49–108
No. 3, March, 1946, pages 109–156
No. 4, April, 1946, pages 157–220
No. 5, May, 1946, pages 221–276
No. 6, June, 1946, pages 277–332
No. 7, July, 1946, pages 333–388
No. 8, August, 1946, pages 389–444
No. 9, September, 1946, pages 445–500
No. 10, October, 1946, pages 501–556
No. 11, November, 1946, pages 557–620
No. 12, December, 1946, pages 621–684

Material that has appeared in the above volume has been indexed under a general subject heading and by author and has been further cross-indexed under various subheadings.

Aerodynamics—

Additional Developments of Greene's Equation to the Study of Compressible Airflow, George L. Shue ... 581
Aileron Reversal Speed by Influence Coefficients and Matrix Iteration, William T. Thomson ... 192
Airplane Maneuvering Loads, E. C. Posner ... 325
Calculation of Flow of Air and Diatomic Gases, Chester W. Smith ... 309
Coupled Surfaces, J. B. Kendrick ... 316
Effective Control of Stalling Characteristics of Highly Tapered and Swept-Back Wings, Maurice A. Garbell ... 88
A Flight Investigation of the Effects of Surface Finish on Wing Profile Drag, W. H. Day and J. M. Schwarzbach 209
The Interaction Between Boundary Layer and Shock Waves in Transonic Flow, Hans Wolfgang Liepmann ... 623
Investigation of Three Methods for Solving the Flutter Equations and Their Relative Merits, R. J. Ruggiero ... 3
Letters to the Editor
Griffin, W. Raymond ... 652
Johnston, R. B. ... 93
Kennedy, Charles C., and C. D. P. Pancu ... 140
Laitone, E. V. ... 404, 645
Lees, Lester ... 638
Liepmann, H. W. ... 94
Pancu, C. D. P., and Charles C. Kennedy ... 140
Pope, Alan ... 93
Sears, W. R. ... 637
Newton and Fluid Mechanics, J. C. Hunsaker ... 647
Superaerodynamics, Mechanics of Rarified Gases, Hsue-Shen Tsien ... 653
Supersonic Wave Drag of Thin Airfoils, Allen E. Puckett 475
Tests on Elbows of a Special Design, John J. Harper ... 587
Vortex Frequency and Flow Pattern in the Wake of Two Parallel Cylinders at Varied Spacing Normal to an Air Stream, Herman M. Spivack ... 289
Aileron reversal speed by influence coefficients and matrix iteration ... 192

Aircraft Propulsion—

Aircraft Ejector Performance, Frank A. McClintock and J. Hall Hood ... 559
British Aircraft Gas Turbines (Ninth Wright Brothers Lecture), H. Roxbee Cox ... 53
The Combination of Dynamical Systems, Thomas G. Sofrin 281
Comparison of Propeller and Reaction-Propelled Airplane Performances, Benson Hamlin and F. Spenceley ... 425
Jet Propulsion Applied to Helicopter Rotors, R. H. Miller 639
Jet Propulsion and Its Application to High-Speed Aircraft, D. J. Keirn and D. R. Shoults ... 411
Letters to the Editor
Dallenbach, Frederick ... 141
Spangler, S. B. ... 180
Propellers for Aircraft Gas Turbines, George W. Brady .. 449
Some Elementary Details of Ramming Intake and Propulsive Jets for Airplanes, Sanford A. Moss and W. R. Foote ... 111
Some Experiences in Full-Scale Power-Plant Testing, Milton U. Clauser ... 247
On the Steady Flow of a Gas Through a Tube with Heat Exchange or Chemical Reaction, Paul Chambré and Chia-Chiao Lin ... 537
Airfoil theory for rotary wing aircraft ... 218
Airfoils, thin, supersonic wave drag of ... 475
ALLEN, RALPH W. Flapping Characteristics of Rigid Rotor Blades ... 183
ANDERSON, JOHN M., AND ORIN B. JOHNSTON. The Application of Established Automatic Control Methods to the Study of Basic Flight Problems ... 235
Anti-icing system, thermal, icing problems and the ... 485
Atomic energy ... 171

Bar, twisted, static displacement and coupled frequencies of a ... 214
BARRETT, ST. J., AND O. A. WHEELON. Symposium on Notch Effects in High-Strength Aluminum Alloys. Part IV. The Effect of Notches upon Limiting Strain in High-Strength Aluminum Alloys ... 401
Beams, a simple tabular method of calculating deflections and influence coefficients of ... 23
BEERER, J. G. The Reduction of Flight-Test Performance Data to Standard Air Conditions by the Temperature Altitude Method ... 543
Bend radii, minimum, effect of bend width upon ... 161
BENSCOTER, STANLEY U. Numerical Transformation Procedures for Shear-Flow Calculation ... 438
BESKIN, L., AND R. M. ROSENBERG. Higher Modes of Vibration by a Method of Sweeping ... 597
BEST, GILBERT C. The Stress-Area Method Applied to Frames ... 151
Blades, helicopter, a method for the stress analysis of ... 195
BOEKE, F. L., AND R. A. PASELK. Icing Problems and the Thermal Anti-Icing System ... 485
BOLEY, BRUNO A., AND BERTRAM KLEIN. Letter to the Editor (Stress Analysis and Structures) ... 276
Boundary layer and shock waves in transonic flow, the interaction between ... 623
BRADY, GEORGE W. Propellers for Aircraft Gas Turbines .. 449

Buckling curves, nondimensional—their development and application 511
Buckling loads of curved thin aluminum-alloy sheets for monocoque constructions, the effect of radius of curvature and preliminary artificial eccentricities on 593
Buckling loads of curved thin aluminum-alloy sheets for monocoque constructions, influence of different factors on 204

CHAMBRÉ, PAUL, AND CHIA-CHIAO LIN. On the Steady Flow of a Gas Through a Tube with Heat Exchange or Chemical Reaction 537
CHIEN, WEI-ZANG, AND THEODORE VON KÁRMÁN. Torsion with Variable Twist 503
CLAUSER, MILTON U. Some Experiences in Full-Scale Power-Plant Testing 247
Column of varying section, a procedure for determining the critical load for a 135
Column paradox, the 678
Compressible airflow, additional developments of Greene's Equation to the study of 581
COX, H. ROXBEE. British Aircraft Gas Turbines (Ninth Wright Brothers Lecture) 53
COZZONE, F. P., AND M. A. MELCON. Nondimensional Buckling Curves—Their Development and Application .. 511
Cylinder, infinite, an analogy among torsional rigidity, rotating fluid inertia, and self-inductance for an 377

DALLENBACH, FREDERICK. Letter to the Editor (Aircraft Propulsion) 141
DAY, W. H., AND J. M. SCHWARZBACH. A Flight Investigation of the Effects of Surface Finish on Wing Profile Drag. 209
De-icer surfaces, reduction of the adhesion of ice to 126
Design—
Aero Medical Aspects of Cabin Pressurization for Military and Commercial Aircraft, W. R. Lovelace, II, and A. P. Gagge 143
Chart for the Design of Wooden Spars, Bernard Etkin ... 498
Flight-Test Investigation of the Strength of a Square-Tipped Wing, Leonid A. Minor 469
Letters to the Editor
Dommasch, D. O. 580
Flax, A. H. 536
Notes on the Design of Pressurized Cabin Aircraft, Daniel O. Dommasch 302
Roadability and Landing Ability in Aircraft Undercarriages, Reinhardt M. Rosenberg 270
Theoretical Principles of Wing-Tip Fins for Tailless Airplanes and Their Practical Application, Maurice A. Garbell 525
DEUTSCH, M. L. Ground Vibrations of Helicopters 223
DOMMASCH, D. O. Letter to the Editor (Design) 580
———— A Method for the Stress Analysis of Helicopter Blades 195
———— Notes on the Design of Pressurized Cabin Aircraft 30
DORN, J. E., A. E. FLANIGAN, AND L. F. TEDSEN. Tensile Properties Affecting the Formability of Aluminum-Alloy Sheet at Elevated Temperatures 457
————, H. R. KAISER, ALAN E. FLANIGAN, AND LESLIE F. TEDSEN. An Autographic Method for Obtaining Load-Extension Records of High-Speed Tensile Tests on Sheet Specimens at Elevated Temperatures 405
DRAKE, D. W. The Effect of Notches on Static and Fatigue Strength 259
DUNHOLTER, R. J. Static Displacement and Coupled Frequencies of a Twisted Bar 214

Elbows of a special design, tests on 587
ETKIN, BERNARD. Chart for the Design of Wooden Spars 498

FLANIGAN, A. E., L. F. TEDSEN, AND J. E. DORN. Tensile Properties Affecting the Formability of Aluminum-Alloy Sheet at Elevated Temperatures 457
————, LESLIE F. TEDSEN, JOHN E. DORN, AND H. R. KAISER. An Autographic Method for Obtaining Load-Extension Records of High-Speed Tensile Tests on Sheet Specimens at Elevated Temperatures 405
FLAX, A. H. Letter to the Editor (Design) 536
Flight Testing—
The Application of Established Automatic Control Methods to the Study of Basic Flight Problems, Orin B. Johnston and John M. Anderson 235
The Determination of the Stalling Speed and the Maximum Lift Coefficient in Flight, Ernest W. Graham and Harold Luskin 95
Development of Precision Radio-Controlled Dynamically Similar Flying Models, Ernest G. Stout 335
A Flight Investigation of the Effects of Surface Finish on Wing Profile Drag, W. H. Day and J. M. Schwarzbach 209
Flight-Test Investigation of the Strength of a Square-Tipped Wing, Leonid A. Minor 469
The Reduction of Flight-Test Performance Data to Standard Air Conditions by the Temperature Altitude Method, J. G. Beerer 543
Fluid mechanics, Newton and 647
Flutter equations and their relative merits, investigation of three methods for solving the 3
FOOTE, W. R., AND SANFORD A. MOSS. Some Elementary Details of Ramming Intake and Propulsive Jets for Airplanes 111
FORBES, T. W. Auditory Signals for Instrument Flying .. 255
Frames, the stress-area method applied to 151

GAGGE, A. P., AND W. R. LOVELACE, II. Aero Medical Aspects of Cabin Pressurization for Military and Commercial Aircraft 143
GARBELL, MAURICE A. Effective Control of Stalling Characteristics of Highly Tapered and Swept-Back Wings ... 88
———— Theoretical Principles of Wing-Tip Fins for Tailless Airplanes and Their Practical Application 525
Gases, diatomic, calculation of flow of air and 309
GERARD, GEORGE. Effect of Bend Width upon Minimum Bend Radii 161
———— Effective Width of Elastically Supported Flat Plates 518
———— Letter to the Editor (Stress Analysis and Structures) 651
————Secant Modulus Method for Determining Plate Instability Above the Proportional Limit 38
GRAHAM, ERNEST W., AND HAROLD LUSKIN. The Determination of the Stalling Speed and the Maximum Lift Coefficient in Flight 95
GRIFFIN, W. RAYMOND. Letter to the Editor (Aerodynamics) 652

HAAS, E. G., AND D. L. LOUGHBOROUGH. Reduction of the Adhesion of Ice to De-Icer Surfaces 126
HAMLIN, BENSON, AND F. SPENCELEY. Comparison of Propeller and Reaction-Propelled Airplane Performances ... 425
HARPER, JOHN J. Tests on Elbows of a Special Design ... 587
Helicopter performance 353
Helicopters, ground vibrations of 223
HILL, D. C., AND J. F. MCBREARTY. Landing Gear Strength Envelopes 229
HOFF, N. J. Letter to the Editor (Stress Analysis and Structures) 363
HOOD, J. HALL, AND FRANK A. MCCLINTOCK. Aircraft Ejector Performance 559

HORVAY, GABRIEL. Vibrations of a Helicopter on the Ground ... 605
HUNSAKER, J. C. Newton and Fluid Mechanics ... 647

Ice Prevention—
Icing Problems and the Thermal Anti-Icing System, F. L. Boeke and R. A. Paselk ... 485
Reduction of the Adhesion of Ice to De-Icer Surfaces, D. L. Loughborough and E. G. Haas ... 126
Instruments—
Analysis of Relay Servomechanisms, Herbert K. Weiss ... 364
The Application of Established Automatic Control Methods to the Study of Basic Flight Problems, Orin B. Johnston and John M. Anderson ... 235
Auditory Signals for Instrument Flying, T. W. Forbes ... 255
Letter to the Editor
Weiss, Herbert K ... 555
ISAACS, RUFUS. Airfoil Theory for Rotary Wing Aircraft ... 218

Jet propulsion and its application to high-speed aircraft ... 411
JOHNSTON, ORIN B., AND JOHN M. ANDERSON. The Application of Established Automatic Control Methods to the Study of Basic Flight Problems ... 235
JOHNSTON, R. B. Letter to the Editor (Aerodynamics) ... 93

KAISER, H. R., AND ALAN E. FLANIGAN, LESLIE F. TEDSEN, AND JOHN E. DORN. An Autographic Method for Obtaining Load-Extension Records of High-Speed Tensile Tests on Sheet Specimens at Elevated Temperatures ... 405
KEIRN, D. J., AND D. R. SHOULTS. Jet Propulsion and Its Application to High-Speed Aircraft ... 411
KENDRICK, J. B. Coupled Surfaces ... 316
KENNEDY, CHARLES C., AND C. D. P. PANCU. Letter to the Editor (Aerodynamics) ... 140
KLEIN, BERTRAM, AND BRUNO A. BOLEY. Letter to the Editor (Stress Analysis and Structures) ... 276

LAITONE, E. V. Letters to the Editor (Aerodynamics) ... 404, 645
Landing Gear—
Landing Gear Strength Envelopes, J. F. McBrearty and D. C. Hill ... 229
Roadability and Landing Ability in Aircraft Undercarriages, Reinhardt M. Rosenberg ... 270
LANGHAAR, HENRY L. Buckling of a Flanged Plate ... 187
——— Stability of Semimonocoque Wing Structures ... 119
LEES, LESTER. Letter to the Editor (Aerodynamics) ... 638
LICHTEN, ROBERT L. Helicopter Performance ... 353
LIEPMANN, HANS WOLFGANG. The Interaction Between Boundary Layer and Shock Waves in Transonic Flow ... 623
——— Letter to the Editor (Aerodynamics) ... 94
LIN, CHIA-CHIAO, AND PAUL CHAMBRÉ. On the Steady Flow of a Gas Through a Tube with Heat Exchange or Chemical Reaction ... 537
Loads, airplane maneuvering ... 325
Loads, dynamic, in airplane structures during landing ... 381
LOUGHBOROUGH, D. L., AND E. G. HAAS. Reduction of the Adhesion of Ice to De-Icer Surfaces ... 126
LOVELACE, W. R., II, AND A. P. GAGGE. Aero Medical Aspects of Cabin Pressurization for Military and Commercial Aircraft ... 143
LUSKIN, HAROLD, AND ERNEST W. GRAHAM. The Determination of the Stalling Speed and the Maximum Lift Coefficient in Flight ... 95

MADDEN, BAXTER C., JR. A Method of Testing Thin Sheet Material in Compression ... 346
MARTIN, G. H. A Procedure for Determining the Critical Load for a Column of Varying Section ... 135
Materials—
An Autographic Method for Obtaining Load-Extension Records of High-Speed Tensile Tests on Sheet Specimens at Elevated Temperatures, Alan E. Flanigan, Leslie F. Tedsen, John E. Dorn, and H. R. Kaiser ... 405
The Effect of Radius of Curvature and Preliminary Artificial Eccentricities on Buckling Loads of Curved Thin Aluminum-Alloy Sheets for Monocoque Constructions, Georges Welter ... 593
Influence of Different Factors on Buckling Loads of Curved Thin Aluminum-Alloy Sheets for Monocoque Constructions, Georges Welter ... 204
A Method of Testing Thin Sheet Material in Compression, Baxter C. Madden, Jr ... 346
Symposium on Notch Effects in High-Strength Aluminum Alloys. Part I. Notch Sensitivity, L. Schapiro and H. E. North; *Part II. The Effects of Open Holes*, C. H. Stevenson; *Part III. Effects in Spar Caps*, D. L. Moseley; *Part IV. Effect upon Limiting Strain*, O. A. Wheelon and St. J. Barrett ... 391
Tensile Properties Affecting the Formability of Aluminum-Alloy Sheet at Elevated Temperatures, A. E. Flanigan, L. F. Tedsen, and J. E. Dorn ... 457
MCBREARTY, J. F., AND D. C. HILL. Landing Gear Strength Envelopes ... 229
MCCLINTOCK, FRANK A., AND J. HALL HOOD. Aircraft Ejector Performance ... 559
MELCON, M. A., AND F. P. COZZONE. Nondimensional Buckling Curves—Their Development and Application ... 511
MILES, JOHN W. An Analogy Among Torsional Rigidity, Rotating Fluid Inertia, and Self-Inductance for an Infinite Cylinder ... 377
MILLER, JAMES A., AND WALTER RAMBERG. Determination and Presentation of Compressive Stress-Strain Data for Thin Sheet Metal ... 569
MILLER, R. H. Jet Propulsion Applied to Helicopter Rotors ... 639
MINOR, LEONID A. Flight-Test Investigation of the Strength of a Square-Tipped Wing ... 469
Models, precision radio-controlled dynamically similar flying, development of ... 335
Monocoque constructions, the effect of radius of curvature and preliminary artificial eccentricities on buckling loads of curved thin aluminum-alloy sheets for ... 593
Monocoque constructions, the influence of different factors on buckling loads of curved thin aluminum-alloy sheets for ... 204
MOSELEY, D. L. Symposium on Notch Effects in High-Strength Aluminum Alloys. Part III. Notch Effects in High-Strength Aluminum-Alloy Spar Caps ... 397
MOSS, SANFORD A., AND W. R. FOOTE. Some Elementary Details of Ramming Intake and Propulsive Jets for Airplanes ... 111
MYKLESTAD, N. O. A Simple Tabular Method of Calculating Deflections and Influence Coefficients of Beams ... 23

NORTH, H. E., AND L. SCHAPIRO. Symposium on Notch Effects in High-Strength Aluminum Alloys. Part I. Notch Sensitivity in High-Strength Aluminum Alloys—Theoretical Aspects ... 391
Notch effects in high-strength aluminum alloys, symposium on ... 391
Notches, the effect of, on static and fatigue strength ... 259

OSGOOD, WILLIAM R. Stress-Strain Formulas ... 45

PANCU, C. D. P., AND CHARLES C. KENNEDY. Letter to the Editor (Aerodynamics) 140
PASELK, R. A., AND F. L. BOEKE. Icing Problems and the Thermal Anti-Icing System 485
Performance—
Comparison of Propeller and Reaction-Propelled Airplane Performances, Benson Hamlin and F. Spenceley 425
The Determination of the Stalling Speed and the Maximum Lift Coefficient in Flight, Ernest W. Graham and Harold Luskin 95
Helicopter Performance, Robert L. Lichten 353
The Reduction of Flight-Test Performance Data to Standard Air Conditions by the Temperature Altitude Method, J. G. Beerer 543
Physiology—
Aero Medical Aspects of Cabin Pressurization for Military and Commercial Aircraft, W. R. Lovelace, II, and A. P. Gagge 143
Plate, flanged, buckling of a 187
Plate instability above the proportional limit, secant modulus method for determining 38
Plates, elastically supported flat, effective width of 518
POPE, ALAN. Letter to the Editor (Aerodynamics) 93
POSNER, E. C. Airplane Maneuvering Loads 325
Power-plant testing, full-scale, some experiences in 247
Pressurization, cabin, for military and commercial aircraft, aero medical aspects of 143
Pressurized cabin aircraft, notes on the design of 302
Propellers—
Propellers for Aircraft Gas Turbines, George W. Brady 449
PUCKETT, ALLEN E. Supersonic Wave Drag of Thin Airfoils 475

RAMBERG, WALTER, AND JAMES A. MILLER. Determination and Presentation of Compressive Stress-Strain Data for Thin Sheet Metal 569
Ramming intake and propulsive jets for airplanes, some elementary details of 111
ROSENBERG, REINHARDT M. Roadability and Landing Ability in Aircraft Undercarriages 270
———————, AND L. BESKIN. Higher Modes of Vibration by a Method of Sweeping 597
ROSS, ROBERT S. An Investigation of the Airflow Underneath Helicopter Rotors 665
Rotating Wing Aircraft—
Airfoil Theory for Rotary Wing Aircraft, Rufus Isaacs 218
Flapping Characteristics of Rigid Rotor Blades, Ralph W. Allen 183
Ground Vibrations of Helicopters, M. L. Deutsch 223
Helicopter Performance, Robert L. Lichten 353
An Investigation of the Airflow Underneath Helicopter Rotors, Robert S. Ross 665
Jet Propulsion Applied to Helicopter Rotors, R. H. Miller 639
Letter to the Editor
Stepniewski, W. Z. 409
A Method for the Stress Analysis of Helicopter Blades, Daniel O. Dommasch 195
Vibrations of a Helicopter on the Ground, Gabriel Horvay 605
Rotor blades, rigid, flapping characteristics of 183
Rotors, helicopter, an investigation of the airflow underneath 665
Rotors, helicopter, jet propulsion applied to 639
RUGGIERO, R. J. Investigation of Three Methods for Solving the Flutter Equations and Their Relative Merits 3

SCHAPIRO, L., AND H. E. NORTH. Symposium on Notch Effects in High-Strength Aluminum Alloys. Part I. Notch Sensitivity in High-Strength Aluminum Alloys—Theoretical Aspects 391
SCHWARZBACH, J. M., AND W. H. DAY. A Flight Investigation of the Effects of Surface Finish on Wing Profile Drag 209
SEARS, W. R. Letter to the Editor (Aerodynamics) 637
Semimonocoque structures under bending, general instability of 29
Servomechanisms, relay, analysis of 364
SHANLEY, F. R. The Column Paradox 678
Shear-flow calculation, numerical transformation procedures for 438
SHOULTS, D. R., AND D. J. KEIRN. Jet Propulsion and Its Application to High-Speed Aircraft 411
SHUE, GEORGE L. Additional Developments of Greene's Equation to the Study of Compressible Airflow 581
SMITH, CHESTER W. Calculation of Flow of Air and Diatomic Gases 309
SOFRIN, THOMAS G. The Combination of Dynamical Systems 281
SPANGLER, S. B. Letter to the Editor (Aircraft Propulsion) 180
Spars, wooden, chart for the design of 498
SPENCELEY, F., AND BENSON HAMLIN. Comparison of Propeller and Reaction-Propelled Airplane Performances ... 425
SPIVACK, HERMAN M. Vortex Frequency and Flow Pattern in the Wake of Two Parallel Cylinders at Varied Spacing Normal to an Air Stream 289
Stalling speed and the maximum lift coefficient in flight, the determination of the 95
STEPNIEWSKI, W. Z. Letter to the Editor (Rotating Wing Aircraft) 409
STEVENSON, C. H. Symposium on Notch Effects in High-Strength Aluminum Alloys. Part II. The Effects of Open Holes on the Tensile Strength of Some Aluminum Alloys 395
STOUT, ERNEST G. Development of Precision Radio-Controlled Dynamically Similar Flying Models 335

Stress Analysis and Structures—
An Analogy Among Torsional Rigidity, Rotating Fluid Inertia, and Self-Inductance for an Infinite Cylinder, John W. Miles 377
Buckling of a Flanged Plate, Henry L. Langhaar 187
The Column Paradox, F. R. Shanley 678
Determination and Presentation of Compressive Stress-Strain Data for Thin Sheet Metal, Walter Ramberg and James A. Miller 569
Dynamic Loads in Airplane Structures During Landing, Shou-Ngo Tu 381
Effect of Bend Width upon Minimum Bend Radii, George Gerard 161
The Effect of Notches on Static and Fatigue Strength, D. W. Drake 259
Effective Width of Elastically Supported Flat Plates, George Gerard 518
General Instability of Semimonocoque Structures Under Bending, Tsun Kuei Wang 29
Higher Modes of Vibration by a Method of Sweeping, L. Beskin and R. M. Rosenberg 597
Influence of Different Factors on Buckling Loads of Curved Thin Aluminum-Alloy Sheets for Monocoque Constructions, Georges Welter 204
Landing Gear Strength Envelopes, J. F. McBrearty and D. C. Hill 229
Letters to the Editor
Boley, Bruno A., and Bertram Klein 276
Gerard, George 651
Hoff, N. J. 363
Klein, Bertram, and Bruno A. Boley 276
Stepniewski, W. Z. 409
Wagner, Francis V. 409

A Method for the Stress Analysis of Helicopter Blades, Daniel O. Dommasch ... 195
Nondimensional Buckling Curves—Their Development and Application, F. P. Cozzone and M. A. Melcon ... 511
Numerical Transformation Procedures for Shear-Flow Calculation, Stanley U. Benscoter ... 438
A Procedure for Determining the Critical Load for a Column of Varying Section, G. H. Martin ... 135
Secant Modulus Method for Determining Plate Instability Above the Proportional Limit, George Gerard ... 38
A Simple Tabular Method of Calculating Deflections and Influence Coefficients of Beams, N. O. Myklestad ... 23
Stability of Semimonocoque Wing Structures, Henry L. Langhaar ... 119
Static Displacement and Coupled Frequencies of a Twisted Bar, R. J. Dunholter ... 214
The Stress-Area Method Applied to Frames, Gilbert C. Best ... 151
Stress-Strain Formulas, William R. Osgood ... 45
Torsion with Variable Twist, Theodore von Kármán and Wei-Zang Chien ... 503

Tailless airplanes, theoretical principles of wing-tip fins for, and their practical application ... 525
Tedsen, L. F., J. E. Dorn, and A. E. Flanigan. Tensile Properties Affecting the Formability of Aluminum-Alloy Sheet at Elevated Temperatures ... 457
———, John E. Dorn, H. R. Kaiser, and Alan E. Flanigan. An Autographic Method for Obtaining Load-Extension Records of High-Speed Tensile Tests on Sheet Specimens at Elevated Temperatures ... 405
Thomson, William T. Aileron Reversal Speed by Influence Coefficients and Matrix Iteration ... 192
Torsion with variable twist ... 503
Transonic flow, the interaction between boundary layer and shock waves in ... 623
Tsien, Hsue-Shen. Atomic Energy ... 171
——— Superaerodynamics, Mechanics of Rarefied Gases ... 653
Tu, Shou-Ngo. Dynamic Loads in Airplane Structures During Landing ... 381
Turbines, gas, British aircraft (Ninth Wright Brothers Lecture) ... 53

Vibration by a method of sweeping, higher modes of ... 597
Vibrations of a helicopter on the ground ... 605
von Kármán, Theodore, and Wei-Zang Chien. Torsion with Variable Twist ... 503

Wagner, Francis V. Letter to the Editor (Stress Analysis and Structures) ... 409
Wang, Tsun Kuei. General Instability of Semimonocoque Structures Under Bending ... 29
Weiss, Herbert K. Analysis of Relay Servomechanisms. 364
——— Letter to the Editor (Instruments). 555
Welter, Georges. The Effect of Radius of Curvature and Preliminary Artificial Eccentricities on Buckling Loads of Curved Thin Aluminum-Alloy Sheets for Monocoque Constructions ... 593
——— Influence of Different Factors on Buckling Loads of Curved Thin Aluminum-Alloy Sheets for Monocoque Constructions ... 204
Wheelon, O. A., and St. J. Barrett. Symposium on Notch Effects in High-Strength Aluminum Alloys. Part IV. The Effect of Notches upon Limiting Strain in High-Strength Aluminum Alloys ... 401
Wing profile drag, a flight investigation of the effects of surface finish on ... 209
Wing, square-tipped, flight-test investigation of the strength of a ... 469
Wing structures, semimonocoque, stability of ... 119
Wings, highly tapered and swept-back, effective control of stalling characteristics of ... 88

Errata

We regret the following errors in the article by Maurice A. Garbell, "Theoretical Principles of Wing-Tip Fins for Tailless Airplanes and Their Practical Application," which appeared in the October, 1946, issue of the Journal of the Aeronautical Sciences on pages 525–536.

(1) Page 530, Eq. (8), the left-hand expression should be: $\left(\frac{dC_N}{d\beta}\right)_f$.

(2) Page 531, Eq. (12), the left-hand expression should be: $\left[\frac{dC_N}{d(rb/2V)}\right]_f$.

(3) Page 534, Eq. (37), the first member of the bracketed expression, right-hand side, should be:

$$\left[\frac{d(C_{D_{P_{fr}}} - C_{D_{P_{fl}}})}{2d\beta}\right] \ldots\ldots$$

(4) Page 535, under the heading "Conclusions," the 8th and 9th lines should read:

"... or sweptback high-aspect-ratio wings and in tail-first airplanes; it is maintained that the central vertical fin is...."